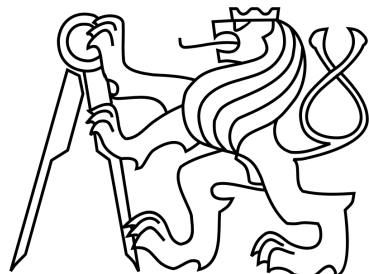


CZECH TECHNICAL UNIVERSITY IN PRAGUE

Faculty of Nuclear Sciences and Physical Engineering

Department of dosimetry and application of ionizing radiation



---

*Ph.D. Thesis*

---

**Pixel detectors in double beta decay,  
experiments COBRA and TGV**

Prague, 2014

Ing. Joshy Madathiparambil Jose



# **Pixel detectors in double beta decay, experiments COBRA and TGV**

**Ph.D. Thesis**

*submitted to*

**Faculty of Nuclear Sciences and Physical Engineering  
Czech Technical University in Prague**

*by*

**Ing. Joshy Madathiparambil Jose \*@**

*Doctoral study program: Applied natural science*

*Discipline: Nuclear engineering*

*Supervisor: Doc. Ing. Ivan Štekl CSc.\**

*Supervisor specialist: Ing. Pavel Čermák PhD.\**

**Prague, 2014**

---

\* Institute of Experimental and Applied Physics, CTU in Prague.

® Faculty of Nuclear Sciences and Physical Engineering, CTU in Prague.



# Declaration

I hereby declare that this dissertation is the result of my own work. Wherever contributions of others are involved, every effort is made to indicate that clearly. All the resources such as literature, projects and software that I have used are stated in the attached lists.

*Prague,  
26 September 2014.*

*Ing. Joshy Madathiparambil Jose*



# Acknowledgements

I would like to express special appreciation and thanks to my supervisor Doc. Ing. Ivan Štekl, CSc. for his persistent support and unbroken confidence in me. He was always positive towards my plans and suggestions, and offered all helps in pursuing them. I would like to thank co-supervisor Ing. Pavel Čermák, PhD. for his active cooperation and support. I express my gratitude to Prof. Ing. Tomáš Čechák, CSc. for his helps and supports from the very beginning of my studies. I am lucky to meet a person like the director of ÚTEF Prof. Ing. Stanislav Pospíšil, DrSc. with a lot of practical experience and boundless enthusiasm. I would like to thank him for giving me an opportunity to work at the institute. I am grateful to all teachers during my PhD studies, especially RnDr. Vladimír Wagner, CSc. for his interesting lectures. It was very valuable experience working with colleagues at the TGV and COBRA collaborations, and I thank all of them, especially Yu. A. Shitov and N. I. Rukhadze for their helps and support. It was a great experience working at the institute interacting with many talented people. I sincerely thank all my colleagues at ÚTEF, especially Pavel Soukup for discussions and suggestions in electronics, Jan Jakubek and Zdeněk Vykydal for sharing their experience in pixel detectors, Karel Smolek for helpful discussions and Ondřej Valach for timely help with mechanical works. I appreciate the helps from staff members at the LSM, France who were kind and helpful with my needs during the visits at the laboratory. Especially, I thank Pia Loaiza for helping with low background measurements of our samples. And finally, I express my heartfelt gratitude to my families for their support and encouragements which was a big moral boost throughout my studies.



# Abstract

The double beta decay ( $\beta\beta$ ) is a very challenging subject in today's physics. It can be used as a powerful tool to test neutrino properties (e.g. if neutrino is Dirac or Majorana type) and lepton number conservation. However, these experiments demand very high sensitivity and very strong background reduction. New experimental approaches are necessary for satisfying such demands. Pixel detectors offer new possibilities in this direction, as it can better identify the background events. Timepix detector from Medipix collaboration is currently under investigation for two double beta decay experiments (TGV, COBRA). A new coincidence setup, pixel telescope (with detectors face to face) has been constructed and extensive background measurements are under way. Main tasks of this work were to understand the background radiation in the pixel setup and to suppress them. The preliminary results obtained from the background measurements (surface and underground) as well as the estimation of the experimental limits for double beta decay which can be achieved using this unique detection technique are presented.

## Shrnutí

Dvojitý beta rozpad ( $\beta\beta$ ) je v současné době velmi intenzivně studovaná oblast fyziky. Tento jev může být využit jako mocný nástroj k experimentálnímu studiu vlastností neutrín (např. testování Diracovské a Majoranovské povahy neutrín) a k testování zákona zachování leptonového čísla. Tyto experimenty však vyžadují vysokou citlivost měření a velmi silné potlačení pozadí. K dosažení lepších výsledků je potřeba využít nových experimentálních přístupů. Pixelové detektory představují jednu z takových možností. Výhodou těchto detektorů je identifikace pozad'ových událostí s lepší efektivitou. Detektor Timepix, vyvíjený kolaborací Medipix, je v současné době zkoumán z hlediska využití v experimentech dvojitého rozpadu beta (TGV, COBRA). Bylo zkonstruováno nové koincidenční zařízení, pixelový teleskop (s detektory umístěnými proti sobě), se kterým jsou v současné době prováděna dlouhodobá měření pozad'ových událostí. Cílem těchto měření je porozumět pozad'ové radiaci v měřící aparatuře. Prezentovány jsou předběžné výsledky z těchto měření (provedená na povrchu i v podzemí).



# Contents

<b>Table of Contents</b>	<b>ix</b>
<b>List of Figures</b>	<b>xiv</b>
<b>List of Tables</b>	<b>xvi</b>
<b>List of abbreviations</b>	<b>xviii</b>
<b>1 Introduction</b>	<b>2</b>
<b>2 Theoretical background</b>	<b>4</b>
2.1 Brief history and basic physics of the neutrino . . . . .	4
2.2 Brief description of double beta decay . . . . .	4
2.3 Experimental sensitivity . . . . .	6
2.4 Experimental approaches and aspects . . . . .	6
2.5 Current results . . . . .	9
2.6 Sources of background and suppression of background events . . . . .	9
<b>3 Experiments TGV, SPT and COBRA</b>	<b>12</b>
3.1 TGV II . . . . .	12
3.2 Silicon Pixel Telescope (Pixel detectors in <i>EC/EC</i> ) . . . . .	15
3.3 COBRA . . . . .	18
<b>4 Timepix pixel detector</b>	<b>25</b>
4.1 Timepix Detector . . . . .	26
4.2 Timepix pixel cell . . . . .	27
4.2.1 Analog section . . . . .	27
4.2.2 Digital section . . . . .	30
4.3 Timepix periphery and readout . . . . .	30
4.4 Equalization and calibration of Timepix . . . . .	31
4.5 Tracking capabilities of Timepix . . . . .	33
<b>5 Intrinsic background studies</b>	<b>40</b>
5.1 PCB materials tests and selection . . . . .	40
5.2 Test of components . . . . .	42
5.3 Test of finished PCBs . . . . .	43

<b>6</b>	<b>Hardware developments</b>	<b>48</b>
6.1	CuFlon Pixel Telescope . . . . .	49
6.2	Flex-Rigid Pixel Telescope . . . . .	51
<b>7</b>	<b>COBRA background measurements</b>	<b>55</b>
7.1	Surface measurements . . . . .	58
7.2	Underground measurements . . . . .	64
<b>8</b>	<b>SPT background measurements</b>	<b>72</b>
8.1	TGV II background . . . . .	72
8.2	Si Pixel Telescope (SPT) background measurements for $2\nu EC/EC$ decay of $^{106}\text{Cd}$ . . . . .	77
8.2.1	Si Single Pixel Detector (standard version) . . . . .	77
8.2.2	CuFlon Si Pixel Telescope . . . . .	79
8.2.3	Flex-Rigid Si Pixel Telescope . . . . .	89
8.3	Background comparison between different setups . . . . .	91
<b>9</b>	<b>Conclusions</b>	<b>93</b>
<b>A</b>	<b>Statement of author's contributions</b>	<b>104</b>
<b>B</b>	<b>List of relevant publications</b>	<b>106</b>
<b>C</b>	<b>Other outputs</b>	<b>108</b>
<b>D</b>	<b>Co-author's statements</b>	<b>110</b>

# List of Figures

2.1	Illustration of double beta decay spectrum with expected neutrinoless decay peak.	5
3.1	The decay scheme of $^{106}\text{Cd}$ .	13
3.2	Schematic cross-section of TGV II setup. It has 16 HPGe detector pairs. In the Figure LN is liquid nitrogen pipe, PA is pre-amplifier, PS is polispider, Cu is parts made of copper and Al is Al-Si alloy parts.	14
3.3	The schematic of the passive shielding for the TGV II measurement setup. In the Figure BPE is borated polyethylene (outermost shielding layer, 16 cm thickness), Pb is lead shielding (10 cm thickness), Cu is copper shielding (20 cm thickness) and T is tube for calibration source.	14
3.4	Schematic illustration of SPT detection unit. The good signature events in the pixel detector pair form either Single Side Events (SSE) or Double Side Events (DSE)	15
3.5	Simulated Efficiencies of $^{106}\text{Cd}$ $2\nu EC/EC$ decay detection in the SPT cell (using Si Timepix detectors of dimension $1.4\text{ cm} \times 1.4\text{ cm} \times 2\text{ mm}$ ) as a function of source foil thickness (mass normalized to 1 at $50\text{ }\mu\text{m}$ foil thickness).	17
3.6	Simulated distance distribution between coincident X-rays (of $^{106}\text{Cd}$ $2\nu EC/EC$ decay) interaction points. The mean distances between hit pixels are 3.2 and 1.2 mm for FG and CG, respectively.	17
3.7	Distance distribution of background Single Side Events (SSE) measured using Si Timepix Single-Pixel-Detector in the underground laboratory.	18
3.8	Co-Planar Grid (CPG) detector used in the COBRA experiment.	19
3.9	CPG detector layer ( $4 \times 4$ CdTe detectors) on Delrin support.	20
3.10	COBRA shielding constructed in the LNGS underground laboratory.	20
3.11	Result obtained from COBRA prototype unit (64 CPG detectors) after collection of $82.2\text{ kg}^*\text{days}$ of data. Background rate as low as 1 count/keV/kg/y was achieved in the 2.8 MeV region.	21
3.12	Simulated stopping ranges for primary particle (double electron of energy 2.8 MeV) in $0\nu\beta\beta$ decay of $^{116}\text{Cd}$ for three different pixel pitch configurations.	21
3.13	Simulated cluster sizes (total pixels in the event) for the $0\nu\beta\beta$ decay (double electron of energy 2.8 MeV) of $^{116}\text{Cd}$ in pixel detectors with different pixel pitches.	22
3.14	Distribution of energy deposited in start, passed and stopped pixels for $110\text{ }\mu\text{m}$ pitch configuration.	22

3.15	Distribution of energy deposited in start, passed and stopped pixels for 55 $\mu\text{m}$ pitch configuration. . . . .	23
3.16	A simulated track of $0\nu\beta^-\beta^-$ decay event from $^{116}\text{Cd}$ generated in CdTe pixel detector of pitch 55 $\mu\text{m}$ . . . . .	24
4.1	Illustration of pixel detector . . . . .	26
4.2	Schematic of Timepix pixel electronics . . . . .	27
4.3	Block diagram of Timepix Charge Sensitive Amplifier. . . . .	28
4.4	Timepix Charge Sensitive Amplifier response to input charge. . . . .	29
4.5	Block diagram of discriminator. . . . .	30
4.6	Illustration of Timepix pixel operation modes. . . . .	31
4.7	Schematic illustration of Timepix periphery. . . . .	32
4.8	FITPix USB readout module. . . . .	32
4.9	Example of Pixelman software Graphical User Interface. . . . .	33
4.10	Illustration of calibration curve. . . . .	34
4.11	Registered events on Si pixel detector in 1 s time window. Pixel detectors can give spatial information along with energy of the events. . . . .	35
4.12	2D track of alpha particle (2869 keV) generated in a 55 $\mu\text{m}$ pitch Si Timepix. . . . .	37
4.13	2D track of electron (2524 keV) generated in a 55 $\mu\text{m}$ pitch Si Timepix. . . . .	38
4.14	2D track of Muon/MIP (2795 keV) generated in a 55 $\mu\text{m}$ pitch Si Timepix. . . . .	39
5.1	Timepix pixel detector mounted on FR4 chip-carrier PCB. The materials close to Si sensor can influence the intrinsic background level of the measurement system. . . . .	41
5.2	Schematic view of two layer PCB. Two layers of copper separated by an insulating layer. . . . .	42
5.3	Components, connectors and glue used in the pixel telescope. These items were measured for intrinsic contamination. . . . .	44
5.4	Finished Pixel Telescope PCBs used in the measurements for intrinsic contamination. . . . .	47
6.1	CERN chip-carrier board with Timepix detector (using CdTe sensor). The PCB is produced from FR4 material. . . . .	48
6.2	Schematic illustration of CuFlon Pixel Telescope. . . . .	50
6.3	CuFlon Pixel Telescope. . . . .	50
6.4	Schematic illustration of Flex-Rigid Pixel Telescope. . . . .	51
6.5	CuFlon Silicon Pixel Telescope. . . . .	52
6.6	Newly produced Flex-Rigid Si Pixel Telescope units mounted in the Delrin support structure. Two units were made using 0.5 mm Si sensors and other two units were made using 1 mm Si sensors. . . . .	53
6.7	Side view of the Delrin structure. The opening to insert additional layer of shielding between the detectors and the readout units is highlighted. . . . .	54
7.1	Timepix CdTe SPD (Single Pixel Detector) inside aluminium (Al) box, which was used in the background studies. Al box was used as a mechanical protection and also as a chamber to flush vaporised liquid Nitrogen ( $\text{N}_2$ ) to suppress the Radon. . . . .	55

7.2	Examples of clusters with different linearities. . . . .	56
7.3	Examples of clusters with different tortuosity. . . . .	56
7.4	Examples of clusters with different roundness. . . . .	57
7.5	Examples of clusters with different circularities. . . . .	57
7.6	Lead shielding (5 cm thickness) used in the surface measurements. . . . .	58
7.7	Full spectrum of surface measurement using CdTe SPD. Duration of measurement was 13.5 days and observed rate of all background events was 11818.46 per hour. . . . .	59
7.8	Alpha spectrum from surface measurement using CdTe SPD. Duration of measurement was 13.5 days and observed rate of alpha events was 15.85 per hour. . . . .	59
7.9	Electron spectrum from surface measurement using CdTe SPD. Duration of measurement was 13.5 days and observed rate of electron events was 23.11 per hour. . . . .	60
7.10	Spectrum of small clusters (sizes up to 10 pixels) from surface measurement using CdTe SPD. Duration of measurement was 13.5 days and observed rate of events was 11621.09 per hour. . . . .	60
7.11	Comparison of alpha, electron and small clusters ( $\leq 10$ pixels) spectra with full spectrum, from surface measurement using CdTe SPD. . . . .	61
7.12	Accumulated frame of alpha clusters in the 2.5 - 3 MeV region from the surface measurement with CdTe SPD. . . . .	62
7.13	Accumulated frame of electron clusters in the 2.5 - 3 MeV region from the surface measurements with CdTe SPD. . . . .	63
7.14	Shielding used in the underground measurements at LNGS. The CdTe SPD was kept inside the Al box and covered by 10 cm of lead. . . . .	64
7.15	Comparison of full spectra from underground measurements with (87.46 events/h) and without N <sub>2</sub> flushing (78.43 events/h) using CdTe SPD. Total time of measurement was 11 and 45 days for without N <sub>2</sub> flushing and with N <sub>2</sub> flushing data, respectively. . . . .	65
7.16	Comparison of full spectra from underground measurements with N <sub>2</sub> flushing (78.43 events/h) and surface measurement without N <sub>2</sub> (11818.46 events/h) using CdTe SPD. Total time of measurement was 45 and 13.5 days for underground and surface data, respectively. . . . .	66
7.17	Alpha spectrum from underground measurements with N <sub>2</sub> flushing. Total time of measurement was 45 days and observed alphas rate was 0.29 events/h. . . . .	67
7.18	Electron spectrum from underground measurements with N <sub>2</sub> flushing. Total time of measurement was 45 days and observed electrons rate was 0.44 events/h. . . . .	68
7.19	Spectrum of events with size $\leq 10$ pixels from underground measurements with N <sub>2</sub> flushing. Total time of measurement was 45 days and observed rate was 75.20 events/h. . . . .	68
7.20	Electron alpha and small clusters spectra compared to full spectrum, from underground measurements with N <sub>2</sub> flushing. . . . .	69
7.21	Accumulated tracks of alphas in 2.5 - 3 MeV region from the LNGS measurements (with 10 cm Pb shielding and N <sub>2</sub> flushing against Rn) with CdTe SPD. . . . .	70

7.22	Accumulated tracks of electrons in 2.5 - 3 MeV region from the LNGS measurements (with 10 cm Pb shielding and N <sub>2</sub> flushing against Rn) with CdTe SPD. . . . .	71
8.1	The schematic of readout electronics for the TGV II measurement setup (DET - detectors 1 to 32 including preamplifiers, SA - spectroscopic amplifier, ADC - analog to digital converter, LE - leading edge discriminator, S - shaper, MT - master trigger, AZOTE - LN2 filling facility). . . . .	74
8.2	TGV II shielding outer view. . . . .	75
8.3	TGV II inner Pb shielding and electronics. . . . .	75
8.4	Scatter plot (2 $\mu$ s vs 8 $\mu$ s shaping times) of SA output from TGV II detectors for raw data (blue), coincident events (green) and events satisfying coincidence and microphonic noise suppression (red). . . . .	76
8.5	Full spectrum comparison between all events, coincident events (satisfying multiplicity criterion) and events satisfying coincidence and microphonic suppression criteria (all criteria) of TGV II background measurement. . .	76
8.6	Full spectrum of background measured using CERN Si SPD in the underground, shielded with 5 cm Pb (219 h). The background rate was 3612 events/day. . . . .	78
8.7	SSE spectrum from background measured using CERN Si SPD in the underground, shielded with 5 cm Pb (219 h). The SSE background rate was 59 events/day. . . . .	78
8.8	SSE distance distribution of CERN Si SPD from underground background measurements shielded with 5 cm Pb (219 h). . . . .	79
8.9	Spectra from CuFlon SPT surface measurements, with 5 cm Pb shielding (15.5 h of measurement) and without any shielding (25 h of measurement). The observed background rate was 42599 events/day for unshielded measurement and 6574 events/day for shielded measurements. . . . .	80
8.10	Spectra of all DSE and SSE events from CuFlon SPT surface measurements without any shielding. Total time of measurement was 25 h. The observed SSE background rate was 390 events/day and DSE rate was 482 events/day.	81
8.11	Distance distribution of all DSE and SSE events from CuFlon SPT surface measurements without any shielding. Total time of measurement was 25 h.	81
8.12	CuFlon SPT inside 5 cm Pb shielding in the LSM underground laboratory, without top layer shielding. . . . .	82
8.13	Comparison of CuFlon SPT and SPD spectra from underground measurements with 5 cm of Pb shielding. Total time of measurement was 4118 hours and 219 hours for SPT and SPD, respectively. Spectra are normalized per detector per day for both measurements. . . . .	83
8.14	Distance distribution of SSE and DSE events from CuFlon SPT underground measurements using 5 cm Pb shielding, from 4118 hours of data.	84
8.15	Schematic illustration of the full shielding installed in the LSM underground laboratory for double beta experiments (SPT and COBRA) using pixel detectors. . . . .	85
8.16	View of the full shielding partially open. . . . .	85

8.17 Comparison of full spectra from underground measurements with full shielding and 5 cm Pb shielding using CuFlon SPT. Time of measurement was 1104 hours and 4118 hours for full shielding measurement and 5 cm Pb shielding measurement, respectively. . . . .	86
8.18 DSE and SSE energy spectra from CuFlon SPT underground measurements (46 days) with full shielding. . . . .	87
8.19 DSE and SSE distance distribution from CuFlon SPT underground measurements (46 days) with full shielding. . . . .	87
8.20 Scatter plot of DSE and SSE events from CuFlon SPT underground measurements with full shielding. Each point on the plot represents two coincident events represented by k1 and k2 (background events for $^{106}\text{Cd}$ $2\nu EC/EC$ decay signature). The region of interest (19 - 23 keV) is marked with a rectangle. . . . .	88
8.21 Spectrum from surface measurements with natural Cd foil between the pixel detectors in the Flex-Rigid SPT. Measurement was without shielding and duration of measurement was 125 hours. . . . .	89
8.22 Spectrum in the energy window 5-200 keV from surface measurements with natural Cd foil between the pixel detectors in the Flex-Rigid SPT (without shielding). The Cd X-ray peak is visible in the 19-23 keV region. . . . .	90
8.23 DSE and SSE distance distribution from Flex-Rigid SPT (with natural Cd foil between them) surface measurements (125 hours) without shielding. . . . .	90

# List of Tables

2.1	Selected results for $2\nu\beta\beta$ decay channel from different double beta experiments. . . . .	9
2.2	Selected results for $0\nu\beta\beta$ decay channel from different double beta experiments. All results except Heidelberg-Moscow (which is with $6\sigma$ ) is with 90% C.L. . . . .	9
3.1	List of double beta decay isotopes in CdZnTe, their possible decay modes and natural abundance. . . . .	19
4.1	List of Timepix DACs and description of their functions. . . . .	36
5.1	Intrinsic background measurement results of Timepix readout ASIC and bump-bonding materials, measured at the low background setup in the LSM laboratory (HPGe planar detector, $150\text{ cm}^2$ , range 20 keV- 1.5 MeV). . . . .	41
5.2	Intrinsic background measurement result of FR4 chip-carrier PCB measured at the low background setup in the LSM laboratory (HPGe planar detector, $150\text{ cm}^2$ , range 20 keV- 1.5 MeV). Mass of sample was 12.343 g and time of measurement was 83466 s. . . . .	41
5.3	Intrinsic background measurement result of CuFlon PCB material. CuFlon is made of Teflon and copper. . . . .	42
5.4	Results of measurements of radioactive impurities in selected flexible PCB materials. VonRoll Laminem KT50/A1 is single side copper and Kapton with glue. Dupot Pyralux FR 9151 is double side copper on kapton. . . . .	43
5.5	Results of radioactive impurities measurements for adhesive and solder mask (Coverlay FR 0210) used in flexible PCBs. Adhesive is used to glue more layers of flexible PCB layers. Solder mask is a layer covering the surface of PCB to protect copper from oxidation and other damages. . . . .	43
5.6	Intrinsic background measurement results of ceramic capacitor. Results are shown in both mBq/kg and mBq/unit where a unit is a single capacitor. . . . .	45
5.7	Intrinsic background measurement results of Tantalum capacitor. Results are shown in both mBq/kg and mBq/unit, where a unit is a single capacitor. . . . .	45
5.8	Intrinsic background measurement results of connector. . . . .	46
5.9	Intrinsic background measurement results of glue. . . . .	46
5.10	Intrinsic background measurement results of finished Pixel Telescope PCBs. . . . .	46
7.1	Estimated background rates from CdTe SPD surface measurements for a duration of 13.5 days. The region of interest (ROI) is 2.5 - 3 MeV. . . . .	61

7.2	Estimated background rates (all events) from surface and underground (with and without N <sub>2</sub> flushing) measurements using CdTe SPD. Total time of measurement was 13.5, 11 and 45 days for surface, underground without N <sub>2</sub> flushing and underground with N <sub>2</sub> flushing data, respectively. The region of interest is 2.5 - 3 MeV. . . . .	64
7.3	Estimated background rates from underground measurements (with and without N <sub>2</sub> flushing) in comparison to surface measurements (without N <sub>2</sub> flushing). Total time of measurement was 13.5, 11 and 45 days for surface, underground without N <sub>2</sub> flushing and underground with N <sub>2</sub> flushing data, respectively. The region of interest (ROI) is 2.5 - 3 MeV. . . . .	67
8.1	Estimated TGV II background rates from a background run with natural Cd foil between the detector pairs (all criteria $\Rightarrow$ with coincidence and microphonic suppression). Total duration of measurement was 2965 hours.	73
8.2	Results of Si SPD background measurements, from underground data (219 h) with 5 cm lead shielding. The region of interest (ROI) is 19 - 23 keV. All numbers are normalized per hour. . . . .	78
8.3	Estimated background rates from CuFlon SPT surface measurements, with (15.5 h of measurement) and without (25 h of measurement) lead shielding. The region of interest (ROI) is 19 - 23 keV. All numbers are normalized per hour. . . . .	80
8.4	Results of CuFlon SPT underground background measurements, with 5 cm lead shielding. The region of interest (ROI) is 19 - 23 keV. Total time of measurement was 4118 hours. . . . .	83
8.5	Results of CuFlon SPT underground background measurements, with full shielding. The region of interest (ROI) is 19 - 23 keV. All numbers are normalized per hour. . . . .	86
8.6	Comparison of background measurements for three different configurations (SPD, SPT with simple shielding and SPT with full shielding) conducted in the LSM underground laboratory. The region of interest (ROI) is 19 - 23 keV. SPD results are per one detector whereas the others are per detector pair. . . . .	91
8.7	Comparison of estimated SSE background rates for three different configurations (SPD, SPT with simple shielding and SPT with full shielding). The region of interest (ROI) is 19 - 23 keV. SPD results are per one detector whereas the others are per detector pair. . . . .	92
8.8	Comparison of estimated DSE background rates for SPT with simple shielding and full shielding. DSE events cannot be detected by SPD as it is a single detector. The region of interest (ROI) is 19 - 23 keV. . . . .	92
8.9	Comparison of TGV II and SPT backgrounds with full shielding. The region of interest (ROI) is 19 - 23 keV for SPT and TGV II DSE whereas the TGV II SSE ROI is 40 - 44 keV. All numbers are normalized per detector-pair per 1.96 cm <sup>2</sup> (SPT area) per hour. . . . .	92



# List of abbreviations

<b>ADC</b>	Analog to Digital Converter
<b>ASIC</b>	Application Specific Integrated Circuit
<b>BPE</b>	Borated Polyethylene
<b>CdTe</b>	Cadmium Telluride
<b>CdZnTe</b>	Cadmium Zinc Telluride
<b>CG</b>	Close Geometry
<b>COBRA</b>	Cadmium Zinc Telluride 0-Neutrino Double-Beta Research Apparatus
<b>CPG</b>	Co-Planar Grid
<b>CSA</b>	Charge Sensing Amplifier
<b>CZT</b>	Cadmium Zinc Telluride
<b>DAC</b>	Digital to Analog Converter
<b>DSE</b>	Double Side Event
<b>FG</b>	Far Geometry
<b>HPGe</b>	High Purity Germanium
<b>LNGS</b>	Laboratori Nazionali del Gran Sasso
<b>LSM</b>	Laboratoire Souterrain de Modane
<b>OTA</b>	Operational Trans-conductance Amplifier
<b>PCB</b>	Printed Circuit Board
<b>ROI</b>	Region of Interest
<b>SA</b>	Spectroscopic Amplifier
<b>SPD</b>	Single Pixel Detector
<b>SPT</b>	Silicon Pixel Telescope
<b>SSE</b>	Single Side Event
<b>TGV</b>	Telescope Germanium Vertical
<b>TOA</b>	Time Of Arrival
<b>TOT</b>	Time Over Threshold



# Chapter 1

## Introduction

The double beta ( $\beta\beta$ ) decay is very attractive frontier for physicists around the world. It is known for long time that significant portion of our universe is formed by neutrinos [1], still interesting properties of them are yet to be identified. The discovery of the neutrino oscillations indicates that they have non-zero mass, though very small. Observation of neutrinoless double beta decay ( $0\nu\beta\beta$ ) will reveal basic property of neutrino (Dirac or Majorana particle) and will challenge the Standard Model by lepton number violation. It will also help to estimate the absolute mass scale of these particles. However, these experiments demand very high sensitivity and strong background reduction.

The group at IEAP, CTU in Prague (in the framework of TGV [2] and COBRA [3] collaborations) has been performing intensive R&D towards the use of hybrid pixel detector Timepix in the  $\beta\beta$  decay experiments. Timepix ASIC has  $256 \times 256$  pixels with size  $55 \times 55 \mu m^2$  and it can be bump-bonded to different sensor materials (such as Si, CdTe, GaAs, etc.) [4]. Pixel detectors can identify the background signals very effectively and thus improve the S/B ratio. The Timepix ASIC, operated in Time Over Threshold (TOT) mode, provides spectroscopic capabilities in each individual pixel [4]. The main advantage of such detector is its ability to identify and reject background signals (e.g. tracks made by electrons, alpha particles, muons, etc.) from the 2D signature generated by the particle interaction [5]. It would also efficiently recognize the signals of  $\beta\beta$  decay processes. Pixel detectors were planned to arrange as "Pixel Telescope", where the sensors are placed in the face-to-face arrangement, and are operated in coincidence. This coincidence unit is considered as the solution for both experiments (Si sensors for TGV and CdTe for COBRA).

In TGV experiment,  $2\nu EC/EC$  of  $^{106}\text{Cd}$  (from g.s. to g.s.) is point of interest, and two coincident X-rays each with 21 keV is the signature of the decay trying to observe [6]. Silicon Pixel Telescope (SPT) is an extension of TGV II experiment, where Silicon Timepix detectors (Timepix ASIC bump-bonded with Si sensor) are planned as the detectors [7]. A pair of detectors with the Cd foil (made of enriched  $^{106}\text{Cd}$  isotope) in between them forms the detection unit. TGV experiment is a passive source experiment where source of decay and detector are separate entities. The location of TGV experiment is in the LSM underground laboratory, Modane, France.

The COBRA experiment aims to study double beta decay using CZT semiconductor detectors [3]. The emphasis is on the  $0\nu\beta\beta$  decay of  $^{116}\text{Cd}$  due to high Q value of the decay. This decay channel has the signature of double electrons (two simultaneous electrons starting from a common point) with total energy at Q value of the decay ( $\sim 2.8$  MeV). CdTe Timepix detectors (Timepix ASIC bump-bonded with CdTe sensor) are one of the possibilities for this experiment. The CdTe sensors will be finally fabricated from enriched material, thus the sensors act as the source of decay (active source experiment). The COBRA experiment is located in the LNGS underground laboratory, Gran Sasso, Italy.

Main aims of this thesis were to propose suitable experimental setup for both experiments (SPT and COBRA) using pixel detectors, select low background materials for construction of setups, fabricate prototype units, investigate the origin and level of background in pixel setups, thus study the feasibility of pixel detectors for  $\beta\beta$  decay experiments and pave the way for a larger experimental setup.

The structure of the thesis is as follows. Chapter 2 gives a brief description of history of double beta decay, presents past and current experiments in the field and explains the need for the background measurements. Chapter 3 introduces the experiments TGV, SPT and COBRA. Chapter 4 gives a brief description of Timepix detector system. Chapter 5 presents the results from intrinsic background studies. Chapter 6 presents the hardware developments associated with this work. Chapter 7 gives the results of COBRA background measurements and chapter 8 gives the results of SPT background measurements. Chapter 9 concludes the thesis. The statement of author's contributions, list of relevant publications and other outputs and statements from co-authors are give in the appendix section.

# Chapter 2

## Theoretical background

### 2.1 Brief history and basic physics of the neutrino

In the late 1920's and early 1930's the beta decay spectrum has been measured as continuous (in contrast to alpha and gamma ray spectrum) [8]. The 'missing energy' in this decay was explained by W. Pauli in 1930, who introduced the concept of a new particle (light, neutral, spin = 1/2). He called this particle as 'neutron'. E. Fermi in 1931 gave the name 'neutrino' to the new unknown particle. Fermi further developed the theory of beta decay [9]. Only in 1956, Reines and Cowan detected neutrino by reaction of inverse beta decay ( $\bar{\nu}_e + p \rightarrow n + e^+$ ) [10].

At present, three types of neutrinos are known, electron neutrino ( $\nu_e$ ), muon neutrino ( $\nu_\mu$ ) and tau neutrino ( $\nu_\tau$ ). The first two types of neutrinos were detected, while  $\nu_\tau$  is known only indirectly from the  $\tau$  decay modes. Due to the results from several oscillation experiments like Super-Kamiokande [11], SNO [12] and KamLAND [13], the proofs of non-zero mass of neutrino exist. Unfortunately, neutrino oscillation experiments are not sensitive to the neutrino mass and give no information about the absolute neutrino mass scale. The most promising test of the neutrino nature (Majorana type  $\nu = \bar{\nu}$  or Dirac type  $\nu \neq \bar{\nu}$ ) is neutrinoless double beta decay, while the mass of  $\nu_e$  can be obtained from the measurement of single beta decay energy spectrum (e.g. KATRIN experiment [14]).

### 2.2 Brief description of double beta decay

There are several reviews, e.g. [15] and [16], fully covering this subject. Double beta decay was first considered in 1935 paper by Maria Goeppert Mayer [17]. She proposed the following process:

$$(A, Z) \rightarrow (A, Z + 2) + 2e^- + 2\bar{\nu}, \quad (2.1)$$

which is called two neutrino double beta decay ( $2\nu\beta\beta$ ). The neutrinoless mode was proposed by W. H. Furry [18] in 1939 as:

$$(A, Z) \rightarrow (A, Z + 2) + 2e^-, \quad (2.2)$$

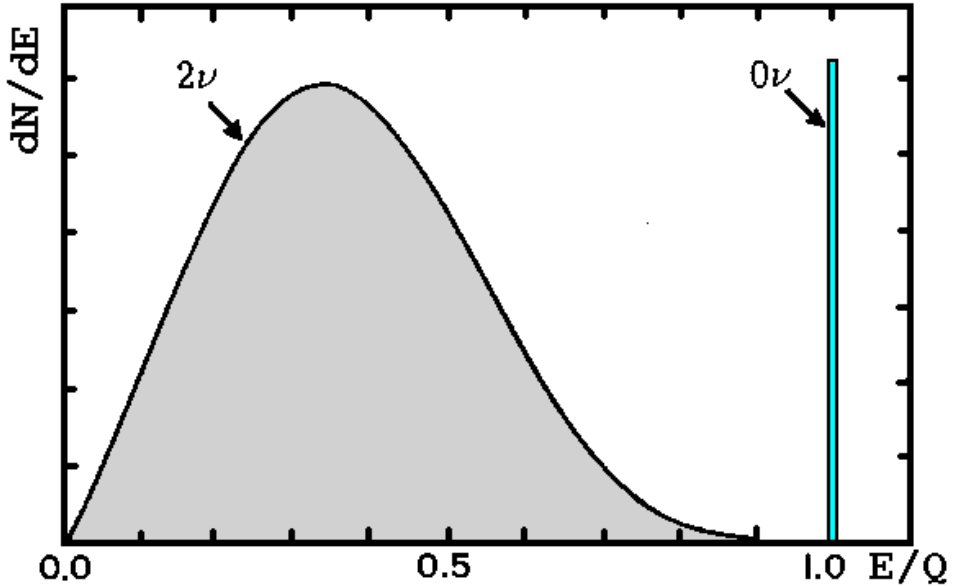
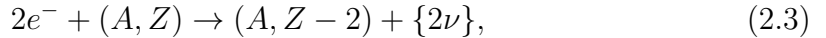


Figure 2.1: Illustration of double beta decay spectrum with expected neutrinoless decay peak.

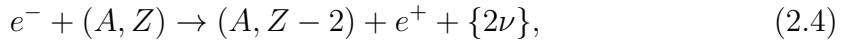
where  $A$  and  $Z$  are the mass and atomic numbers of the parent nucleus, respectively. The sum spectrum of the two emitted electrons for both modes are shown in Figure 2.1.

$2\nu\beta\beta$  exists in the framework of the Standard Model and has been measured for ten isotopes. The measured half lives are in the range of  $10^{19} - 10^{21}$  years [19]. These results are very important for the further developments in nuclear matrix elements calculations.  $0\nu\beta\beta$  process is an extremely slow lepton number violating nuclear transition (expected  $T_{1/2} > 10^{25}$  years) and may occur if neutrinos are massive and are its own anti-particle [20]. In addition to the above mentioned  $\beta\beta$  process, some other processes are also important such as:

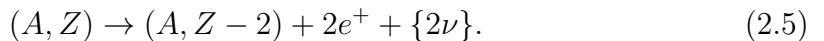
- The capture of bound atomic electrons ( $EC/EC$ ):



- The capture of one bound atomic electron and emission of one positron ( $\beta^+/EC$ ):



- The emission of two positrons ( $\beta^+\beta^+$ ):



In comparison with  $\beta^-\beta^-$  decay, other channels such as  $EC/EC$ ,  $\beta^+/EC$  and  $\beta^+\beta^+$  are suppressed by small available kinetic energy, or by Coulomb repulsion on positron, or due to a small overlap of bound electron wave function with nucleus.

The double beta experiments provide half lives of  $2\nu\beta\beta$  ( $T_{1/2}^{2\nu}$ ) and  $0\nu\beta\beta$  ( $T_{1/2}^{0\nu}$ ), which are related to other parameters as follows:

$$(T_{1/2}^{2\nu})^{-1} = G^{2\nu} |M_{GT}^{2\nu}|^2, \quad (2.6)$$

$$(T_{1/2}^{0\nu})^{-1} = G^{0\nu} |M_{GT}^{0\nu}|^2 \langle m_{\beta\beta} \rangle^2, \quad (2.7)$$

where  $G$  is phase space factor,  $|M_{GT}|$  is nuclear matrix element and  $\langle m_{\beta\beta} \rangle$  is effective Majorana mass. From the measurements of  $0\nu\beta\beta$  half-life only  $|M_{GT}^{0\nu}| \langle m_{\beta\beta} \rangle$  is obtained, where the nuclear matrix element (NME) calculations are model dependent [21].

## 2.3 Experimental sensitivity

As pointed before,  $0\nu\beta\beta$  decay is extremely slow transition (experimental half-life,  $T_{1/2}^{0\nu} \geq 10^{25}$  y).  $0\nu\beta\beta$  experiments today have several tens of kilograms of the parent nuclei running for several years. An approximate analytic expression for the half-life of the experiment with a given level of background is defined in [20] as:

$$T_{1/2}^{0\nu}(n_\sigma) = \frac{4.16 \times 10^{26} y}{n_\sigma} \left( \frac{\epsilon \cdot a}{W} \right) \sqrt{\frac{M \cdot t}{b \cdot \Delta E}}, \quad (2.8)$$

where  $n_\sigma$  is the number of standard deviations corresponding to a given confidence level (e.g. CL of 99.73 %  $\Rightarrow n_\sigma = 3$ ),  $\epsilon$  is the efficiency of registration,  $a$  is the isotopic abundance of the source,  $W$  is the molecular weight of the source material,  $M$  is the total mass of the source,  $t$  is the time of measurement,  $b$  is the specific background rate in counts/keV/kg/y, and  $\Delta E$  is the energy resolution of the detector. This equation is valid only if the background rate is large enough so that the uncertainty is proportional to  $\sqrt{b \cdot \Delta E}$ . To reach a sensitivity of  $\langle m_{\beta\beta} \rangle^2 \approx 0.1$  eV, an experiment must be able to observe a half-life of  $10^{26} - 10^{27}$  y. Thus, next generation of experiments in this field will require hundreds of kg of parent isotopes and significant decrease in the background (below 0.1 counts/keV/kg/y) [20].

## 2.4 Experimental approaches and aspects

There are different approaches for double beta decay experiments. They are broadly classified into two groups:

- Indirect experiments,
- Direct experiments.

Indirect experiments can be again divided into geochemical and radiochemical experiments. The existence of  $\beta\beta$  decay was first established by the geochemical method. This is based on the search for daughter products accumulated in old minerals that are rich in parent isotope. The quantity of daughter products is determined by chemical analysis or by mass spectroscopy. Advantage of this method is large time of accumulation (billions of

years), but disadvantage is the missing energy information (thus impossible to distinguish different  $\beta\beta$  decay modes). One of the first geochemical experiments was for  $\beta\beta$  decay of  $^{130}\text{Te}$  to  $^{130}\text{Xe}$  by Inghram and Reynolds which observed a half-life  $T_{1/2}^{\beta\beta} = 1.4 \times 10^{21}$  years [22]. On the other hand, radiochemical experiments measure the daughter isotopes from a specific interaction. The isotopes used are  $^{238}\text{U}$ ,  $^{232}\text{Th}$  and  $^{244}\text{Pu}$ . One of the earliest such experiments was for  $\beta\beta$  of  $^{238}\text{U}$  to  $^{238}\text{Pu}$  with a half-life of 87.7 years [23]. Because of its low  $Q_{\beta\beta}$  value and high observed decay rate compared to the theoretically predicted half-life, the result was interpreted as an evidence of  $0\nu\beta\beta$  decay [20]. Radiochemical experiments too are insensitive to different modes of  $\beta\beta$  decay.

The decay modes of  $\beta\beta$  can be distinguished in direct experiments. Direct experiments can be subdivide into active and passive source experiments. In active source experiment, the detector is constructed with  $\beta\beta$  isotope (eg.  $^{76}\text{Ge}$ ). One of the first such attempts were done by Mateosian and Goldhaber for  $^{48}\text{Ca}$  using calcium fluoride crystals [24]. In 1967, Fiorini et al. used Ge(Li) detectors which marked beginning of semiconductor detectors in the field of  $\beta\beta$  decay [25]. On the other hand, in passive source experiments, detector and source are separate.

Currently there are several experiments around the world trying to solve double beta decay problem. Some of the interesting experiments (past and present) are briefly described below.

## The Heidelberg-Moscow experiment

The Heidelberg-Moscow experiment is a completed experiment which searched for the neutrinoless double beta decay of  $^{76}\text{Ge}$  [26]. It operated with five Germanium detectors (overall weight of 10.9 kg and enriched with 86%  $^{76}\text{Ge}$ ) in the Laboratori Nazionali del Gran Sasso (LNGS) underground laboratory. A sub-group of this collaboration has claimed the detection of the neutrinoless double beta decay ( $T_{1/2}^{0\nu\beta\beta} = 2.23^{+0.44}_{-0.31} \times 10^{25}$ ) [27].

## Enriched Xenon Observatory (EXO)

Enriched Xenon Observatory (EXO) is an experiment searching for double beta decay of  $^{136}\text{Xe}$  with a Q value of 2.48 MeV [28]. The setup consists of a large amount of isotopically enriched liquid  $^{136}\text{Xe}$  in a time projection chamber (TPC). The electrons interacting in liquid Xe produce scintillation light, and are detected using avalanche photodiodes. Also, the ionized electrons are electrostatically collected on the other end of the TPC. Currently, a prototype of 200 kg liquid Xe (enriched up to 80%) is being operated and a lower limit on the half-life of neutrinoless double beta decay,  $T_{1/2}^{0\nu\beta\beta} > 1.6 \times 10^{25}$  y (90% C.L.) has been achieved [29]. The final aim of EXO collaboration is to have a tonne-scale experiment.

## The GERmanium Detector Array (GERDA)

The GERDA experiment searches for neutrinoless double beta decay of  $^{76}\text{Ge}$  [30]. The experiment is located at the Laboratori Nazionali del Gran Sasso, INFN, Italy. Detec-

tor used is high purity germanium diode. The setup uses high purity liquid argon as coolant and water as the neutron shielding. The experiment aims to verify the claims of Heidelberg-Moscow experiment, and in the second phase to increase the amount of Ge detectors significantly and to achieve a background rate of  $1 \times 10^{-3}$  counts/keV/kg/y at  $Q_{\beta\beta}$ . Currently, they have published the phase-1 results with a total exposure of 21.6 kg.y and the lower limit on the half-life of  $0\nu\beta\beta$ ,  $T_{1/2}^{0\nu\beta\beta} > 2.1 \times 10^{25}$  y (90% C.L.) [31].

## CUORICINO, CUORE

CUORICINO was a pilot experiment located in the LNGS laboratory for the next generation experiment CUORE. It was an array of 62  $\text{TeO}_2$  bolometers to search for neutrinoless double beta decay of  $^{130}\text{Te}$  [32]. The setup had a total mass of 40.7 kg of  $\text{TeO}_2$ , which corresponds to about 11 kg of  $^{130}\text{Te}$ . The experiment aimed to reach a sensitivity of the order of 0.1 - 0.5 eV. From a total exposure of 19.75 kg.y of  $^{130}\text{Te}$ , experiment set the lower bound on the  $0\nu\beta\beta$  half-life,  $T_{1/2}^{0\nu\beta\beta} > 2.8 \times 10^{24}$  y (90% C.L.) [33]. The CUORE experiment (according to the proposal) will consists of 988  $\text{TeO}_2$  bolometers, each having a volume of 5 cm<sup>3</sup> and mass of 750 g [34]. CUORE aims to reach the neutrino mass sensitivity at the level of 0.02 - 0.05 eV.

## SNO+

SNO+ is a kilo-tonne scale experiment to study neutrinos in wide fields (low energy solar neutrinos, reactor neutrinos, geo-neutrinos, supernova neutrinos, etc.), and it is a modified extension of SNO [35]. The experiment is located in an old mine near Sudbury, Ontario, Canada. The setup consists of 12 meter diameter acrylic sphere, filled with approximately 800 tonnes of liquid scintillator (primarily comprised of linear alkyl benzene) floating in a water bath. Neutrinos when interacted with electrons and nuclei produce charge particle which generate light in the scintillation medium which are picked by photomultiplier tubes around. The SNO+ collaboration has also plans to add double beta decay isotope into SNO+ liquid scintillator to measure neutrinoless double beta decay. Currently they plan to use  $^{130}\text{Te}$  as the decay isotope.

## NEMO and SuperNEMO experiments

NEMO experiments are series of experiments (NEMO-1, NEMO-2 and NEMO-3) to measure two neutrino and neutrinoless double beta decay [36]. They were located in the LSM (Laboratoire Souterrain de Modane) underground laboratory, Modane, France. The NEMO-1 and NEMO-2 experiments were two prototype detectors. The NEMO-3 experimental setup had a cylindrical shape, comprised of twenty equal sectors. In each sector, different double beta decay emitters ( $^{100}\text{Mo}$ ,  $^{82}\text{Se}$ ,  $^{116}\text{Cd}$ ,  $^{150}\text{Nd}$ ,  $^{96}\text{Zr}$ ,  $^{48}\text{Ca}$  and  $^{130}\text{Te}$ ) were placed in the form of foils, with tracking detectors on both side of the foils which detected electrons and positrons. The tracking volume was surrounded by calorimeter measuring the energy of detected particle. Data collection had started in January 2003 and finished in 2011 without observing any neutrinoless double beta decay, but providing precise measurements of  $2\nu\beta\beta$  of several isotopes (e.g.  $^{100}\text{Mo}$ ,  $^{82}\text{Se}$ ,  $^{116}\text{Cd}$ ,

Experiment	Isotope	$T_{1/2}^{2\nu}$ (y, with 90% C.L.)
Heidelberg-Moscow	$^{76}\text{Ge}$	$1.55 \pm 0.01(\text{stat})^{+0.19}_{-0.15}(\text{syst}) \times 10^{21}$ [39]
GERDA	$^{76}\text{Ge}$	$1.84^{+0.14}_{-0.10} \times 10^{21}$ [40]
KamLAND-Zen	$^{136}\text{Xe}$	$2.30 \pm 0.02(\text{stat}) \pm 0.12(\text{syst}) \times 10^{21}$ [41]
EXO-200	$^{136}\text{Xe}$	$2.165 \pm 0.016(\text{stat}) \pm 0.059(\text{syst}) \times 10^{21}$ [42]
CUORICINO	$^{130}\text{Te}$	$6.1 \pm 1.4(\text{stat})^{+2.9}_{-3.5}(\text{syst}) \times 10^{20}$ [43]
NEMO-3	$^{100}\text{Mo}$	$0.711 \pm 0.002(\text{stat}) \pm 0.054(\text{syst}) \times 10^{19}$ [37]
NEMO-3	$^{82}\text{Se}$	$9.6 \pm 0.3(\text{stat}) \pm 1.0(\text{syst}) \times 10^{19}$ [37]

Table 2.1: Selected results for  $2\nu\beta\beta$  decay channel from different double beta experiments.

Experiment	Isotope	$T_{1/2}^{0\nu}$ (y)	$\langle m_{\beta\beta} \rangle$ (eV)
Heidelberg-Moscow <sup>a</sup>	$^{76}\text{Ge}$	$= 2.23^{+0.44}_{-0.31} \times 10^{25}$ [27]	$= 0.32^{+0.03}_{-0.03}$
GERDA	$^{76}\text{Ge}$	$> 3.0 \times 10^{25}$ [31]	$< 0.09 - 0.29$
KamLAND-Zen	$^{136}\text{Xe}$	$> 1.9 \times 10^{25}$ [44]	$< 0.12 - 0.25$
EXO-200	$^{136}\text{Xe}$	$> 1.6 \times 10^{25}$ [29]	$< 0.14 - 0.38$
CUORICINO	$^{130}\text{Te}$	$> 2.8 \times 10^{24}$ [33]	$< 0.3 - 0.71$
NEMO-3	e.g. $^{100}\text{Mo}$	$> 1.0 \times 10^{24}$ [37]	$< 0.31 - 0.79$
NEMO-3	$^{82}\text{Se}$	$> 3.2 \times 10^{23}$ [37]	$< 0.94 - 2.6$

Table 2.2: Selected results for  $0\nu\beta\beta$  decay channel from different double beta experiments. All results except Heidelberg-Moscow (which is with  $6\sigma$ ) is with 90% C.L.

<sup>a</sup>This result is widely discussed.

etc.) including processes to excited states (eg. for  $^{100}\text{Mo}$ ). The lower limits for  $0\nu\beta\beta$  half-life were found to be,  $T_{1/2}^{0\nu\beta\beta} > 1.0 \times 10^{24}$  y (90% C.L.) for  $^{100}\text{Mo}$  and  $T_{1/2}^{0\nu\beta\beta} > 3.2 \times 10^{23}$  y (90% C.L.) for  $^{82}\text{Se}$  [37]. The next generation experiment SuperNEMO will comprise of 20 modules, aiming to improve the sensitivity to  $0\nu\beta\beta$  decay in the range  $T_{1/2}^{0\nu\beta\beta} > 10^{26}$  y [38].

## 2.5 Current results

There are many experiments, past and present, which have achieved interesting results in the field. The indirect experiments have proved some success, but they are insensitive to different modes of  $\beta\beta$  decay. The best results are provided by the direct measurements. Some of the important results are listed in Table 2.1 for  $2\nu\beta\beta$  and 2.2 for  $0\nu\beta\beta$ .

## 2.6 Sources of background and suppression of background events

Double beta decay is a very rare process with the half-life at the level of  $10^{20}$  years and longer. Understanding the level and composition of background signals is thus one of the most important issues here. Background events can be broadly classified into two

categories, intrinsic and external backgrounds. Intrinsic background is generated directly from the materials of the detector setup, while external background has origin outside the detector system. The background signals have many different origins (see e.g. [45]) such as:

- cosmological,
- due to natural decay chains,
- neutrons (cosmic, environmental),
- radon and its progenies,
- man made.

Cosmic rays (e.g. muons, electrons) can generate neutrons, bremsstrahlung, electromagnetic shower and also unwanted radioisotopes. As an example, cosmic rays interaction can create isotopes like  $^{57}\text{Co}$ ,  $^{58}\text{Co}$ ,  $^{60}\text{Co}$  and  $^{54}\text{Mn}$  in copper which is usually a material for inner shielding of low counting experiments, or  $^{68}\text{Ge}$ ,  $^{60}\text{Co}$  and  $^{65}\text{Zn}$  in germanium detectors. Experiments are therefore located in the underground laboratories to suppress the cosmic ray induced background.

Another source of background is natural radioactivity. The radioactive decays of primordial elements from the uranium and thorium series and from  $^{40}\text{K}$  generate  $\alpha$ ,  $\beta$  and  $\gamma$  radiations. The  $^{40}\text{K}$  is long-lived decay isotope (average concentration in the upper crust is 850 Bq/kg) even found in human sweat. Effective passive shielding (electroplated copper, archaeological lead) is used for suppression of this kind of background. All materials used for the construction of detector setup should be tested for radioactivity and especially detectors have to be fabricated from very pure components ( $\sim 1 \mu\text{Bq/kg}$ ).

Neutron background has two major origins: fission or  $(\alpha, n)$  reactions. Spontaneous fission occurs from uranium and thorium in surrounding materials and rocks. Also muon interaction on rocks generate neutrons. Newly born neutrons generate radioactive isotopes via  $(n, \gamma)$ ,  $(n, n' \gamma)$  or  $(n, x)$  reactions [20]. Fast neutrons can excite lead by  $(n, n' \gamma)$  reaction, which is very common shielding material, emitting  $\gamma$  rays with energy  $\sim 3$  MeV. Particularly in CdZnTe,  $^{113}\text{Cd}$  is a thermal neutron absorber with the emission of  $\gamma$  rays above 2 MeV. Standard neutron shielding consists of a mixture of moderator and absorber material (e.g. borated polyethylene) and is usually used as an outer shielding of the experimental setup.

Radon (Rn) and its progenies are another threat. It is a colorless, odorless gas which is generated in the U and Th decay chains. Two main Rn isotopes are  $^{220}\text{Rn}$  (half-life of 55.6 s, undergoes alpha decay with energy 6.3 MeV and known as thoron) and  $^{222}\text{Rn}$  (half-life of 3.8 days, undergoes alpha decay with energy 5.59 MeV and known as radon). The important radon progenies and corresponding alpha decay energies are  $^{218}\text{Po}$  ( $E_\alpha = 6003$  keV) and  $^{214}\text{Po}$  ( $E_\alpha = 7687$  keV) both from  $^{222}\text{Rn}$  series, and  $^{216}\text{Po}$  ( $E_\alpha = 6778$  keV) and  $^{212}\text{Bi}$  ( $E_\alpha = 6090$  keV) from  $^{220}\text{Rn}$  series. Rn can stick to the surface of the detector and even diffuse into the detector active area during long-term measurements.

Radon suppression is usually achieved by air-tight construction of the setup and flushing with nitrogen or radon free air.

Human activities have generated some background, too. The nuclear weapon testing, nuclear power plants, use of radioactive materials in industry are human causes of background radiation. Some examples of such products are  $^{60}\text{Co}$ ,  $^{90}\text{Sr}$ ,  $^{134}\text{Cs}$ ,  $^{137}\text{Cs}$ ,  $^{207}\text{Bi}$ , etc.

Suppression of all types of background is very critical for  $\beta\beta$  experiments. The requirement of the current experiments is to reach background in the Region of Interest (ROI) at the level of 1 count/kg/y [20]. To achieve this goal, it is important to understand the sources of background and then make preventive steps. Intrinsic background could be minimized by careful selection of the materials for the setup and clean handling of the detectors. Proper construction of external shielding (Pb, Cu inner shielding, and neutron outer shielding) is important. Rn should also be suppressed. Experiments should be installed in the underground laboratory to reduce cosmic rays. Coincidence measurement techniques are also very helpful in identifying false events. Particle identification (tracking) techniques, precise energy measurements, time of detection, etc., can also be used to reduce the background events.

# Chapter 3

## Experiments TGV, SPT and COBRA

The experimental physics group at IEAP, CTU in Prague is involved in two different double beta decay experiments: TGV [46] and COBRA [3]. TGV collaboration has been established in 1994 and its first experiment (TGV I) was designed for the measurement of  $2\nu\beta\beta$  decay of  $^{48}\text{Ca}$  [47]. In 2000, the experiment TGV II for the measurement of  $2\nu\beta\beta$  decay of  $^{106}\text{Cd}$  was started according to proposal published in [6]. On the contrary, experiment COBRA is a  $0\nu\beta\beta$  experiment with CdZnTe semiconductor detectors with the detector elements itself constituting the decay isotopes [3]. Brief descriptions of both experiments are given in the following sections. Also, the motivations for the pixel detector studies for above mentioned experiments are presented.

### 3.1 TGV II

Up to now in double beta experiment community, major attention is paid towards  $\beta^-\beta^-$  decay mode. There are also other interesting channels (see section 2.2) of  $\beta\beta$  decay, in particular the double electron capture ( $EC/EC$ ) of two bound atomic electrons. In contrast to the  $\beta^-\beta^-$  decay, where  $2\nu\beta^-\beta^-$  mode has been experimentally measured, other double beta decay processes (neither two-neutrino nor neutrinoless mode) have never been observed in the direct experiment, only half-life of  $2\nu EC/EC$  decay of  $^{130}\text{Ba}$  was detected by geochemical experiment as  $(2.2 \pm 0.5) \times 10^{21}$  [48]. The  $^{106}\text{Cd}$  isotope is one of the candidates for studying  $EC/EC$  decay due to the high decay energy ( $Q_{EC/EC} = 2770 \pm 7.2 \text{ keV}$ ). The decay schemes of  $^{106}\text{Cd}$  is shown in Figure 3.1. The  $2\nu EC/EC$  decay of  $^{106}\text{Cd}$  with the transition to the ground state of  $^{106}\text{Pd}$  ( $0_{g.s.}^+ \rightarrow 0_{g.s.}^+$ ) is characterized by emission of two coincident X-rays each with an energy of  $\approx 21 \text{ keV}$ :

$$2e^- + {}_{48}^{106}\text{Cd} \rightarrow {}_{46}^{106}\text{Pd} + 2\nu_e + (\gamma, X - rays);$$
$$Q_{EC/EC} = 2778 \text{ keV}, ROI^1 = 19 \text{ keV} \leq E_X \leq 23 \text{ keV}.$$

---

<sup>1</sup>Region of interest

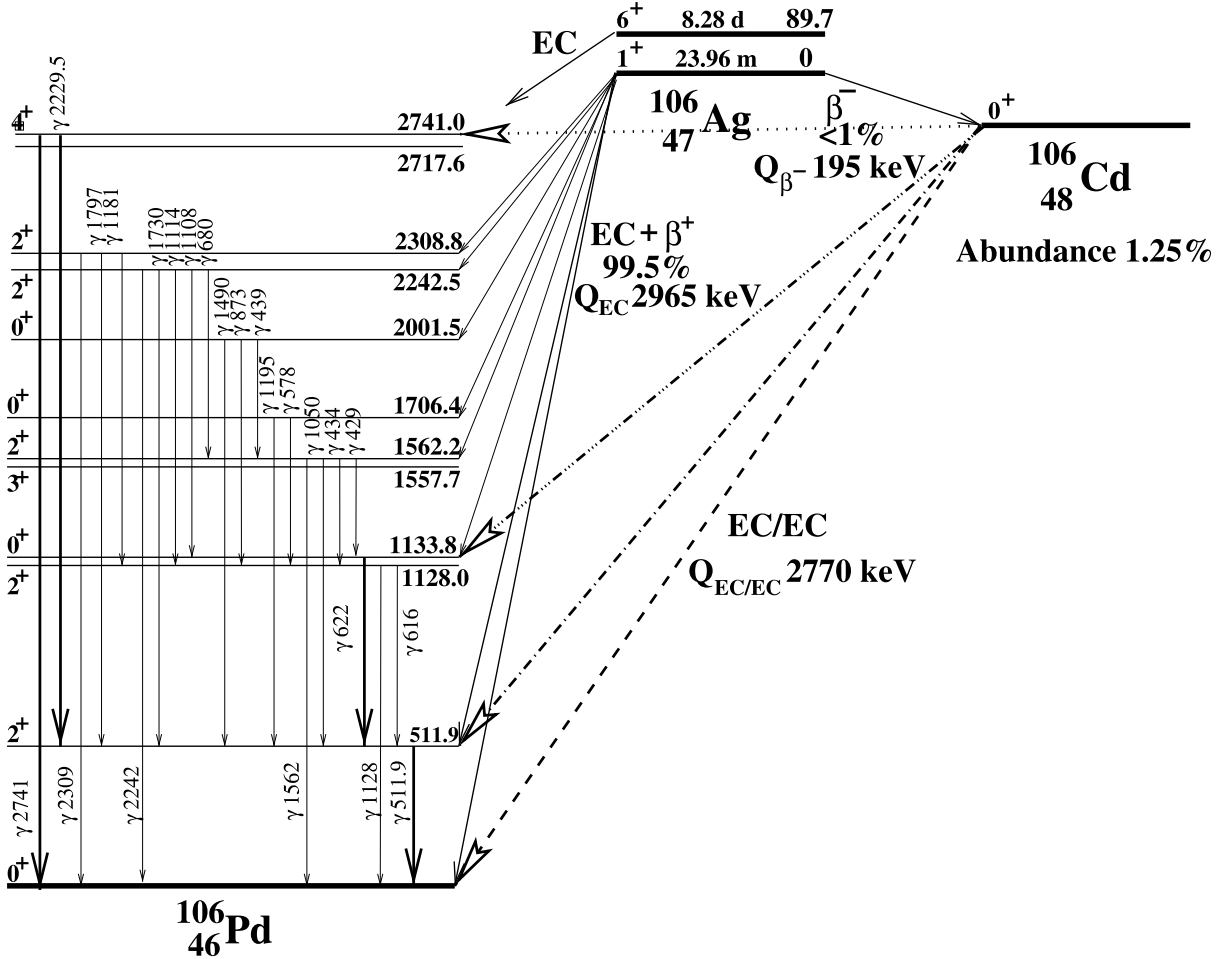


Figure 3.1: The decay scheme of  $^{106}\text{Cd}$ .

Investigation of  $EC/EC$  decay of  $^{106}\text{Cd}$  has been carried out in the LSM underground laboratory, Modane, France, using the low background spectrometer TGV II (Telescope Germanium Vertical) [49]. The location of the experiment (LSM underground laboratory) has an overburden of 4800 mwe (meter water equivalent) and the muon flux is very low ( $4.2 \text{ m}^{-2}\text{day}^{-1}$ ). The spectrometer is comprised of 32 HPGe planar type detectors (16 pairs) with the sensitive volume of  $20.4 \text{ cm}^2 \times 0.6 \text{ cm}^2$  each. Figure 3.2 illustrates in details the detector configuration. Thin foil of  $^{106}\text{Cd}$  ( $\phi$  52 mm,  $50 \mu\text{m}$  thickness) was inserted between pairs of HPGe detectors (16 samples with total mass of 13.6 g) forming a 'sandwich-like' configuration (see Figure 3.2). The total mass of the detectors (of germanium) is about 3 kg, and total sensitive volume is as large as  $400 \text{ cm}^2$ . The setup had a passive shielding made of copper ( $\approx 20$  cm thickness), lead ( $\approx 10$  cm thickness) and neutron shielding (16 cm of borated polyethylene). Currently, a half-life limit of  $\geq 4.2 \times 10^{20}$  years has been achieved by TGV for the above mentioned decay channel [46]. The Figure 3.3 is a schematic view of the passive shielding and detector arrangement in the TGV II.

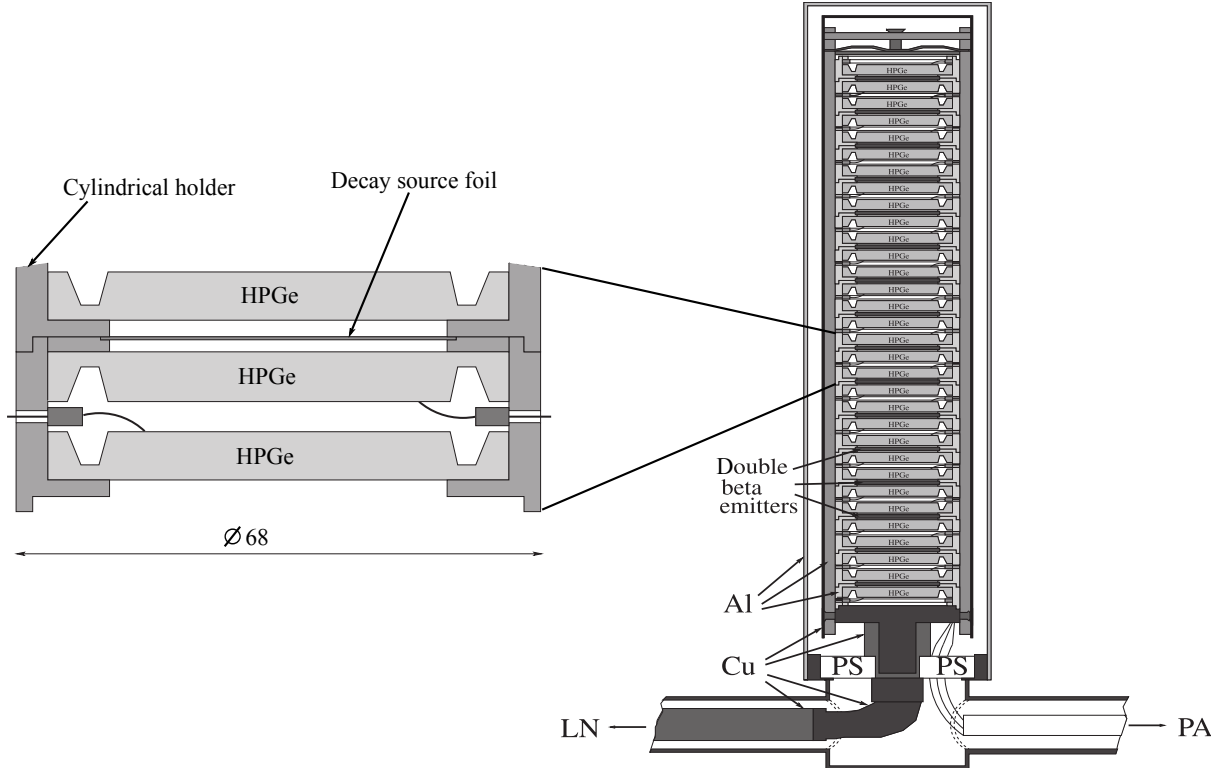


Figure 3.2: Schematic cross-section of TGV II setup. It has 16 HPGe detector pairs. In the Figure LN is liquid nitrogen pipe, PA is pre-amplifier, PS is polispider, Cu is parts made of copper and Al is Al-Si alloy parts.

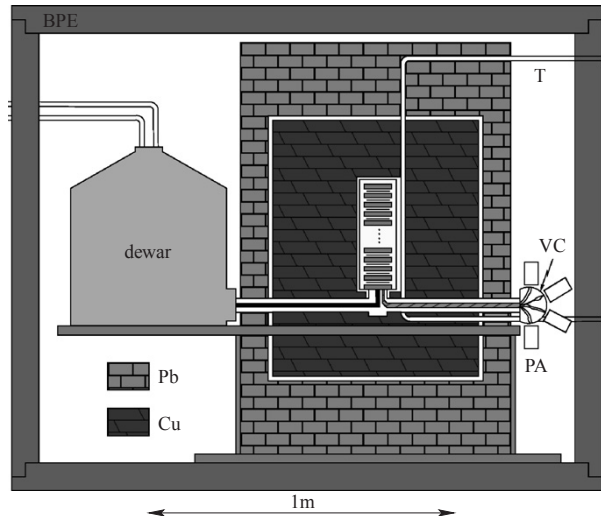


Figure 3.3: The schematic of the passive shielding for the TGV II measurement setup. In the Figure BPE is borated polyethylene (outermost shielding layer, 16 cm thickness), Pb is lead shielding (10 cm thickness), Cu is copper shielding (20 cm thickness) and T is tube for calibration source.

### 3.2 Silicon Pixel Telescope (Pixel detectors in EC/EC)

Research and development is being carried out at IEAP to utilize pixel detectors in the next generation of double beta experiments [50]. The TGV collaboration has proposed to use Timepix detectors in double electron capture of  $^{106}\text{Cd}$  [7]. The experimental setup using pixel detector for double electron capture (next stage of TGV II) is termed as Silicon Pixel Telescope (SPT). The TGV detection philosophy is a pair of detectors with decay foil in between them. In this configuration, if the coincident signature events (two Pd X-rays, say  $k_1, k_2$ ) deposit on same detector it is termed as Single Side Event (SSE); and if they deposit on opposite detectors it is termed as Double Side Event (DSE). In TGV II detector, SSE event is unreliable as the two simultaneous events will be registered as single event, resulting only DSE event providing useful information. Whereas, in SPT (see Figure 3.4) the HPGe detectors are replaced by Si pixel detectors. Enriched Cd foil is placed in between pixel detector pairs, forming the detection unit. SPT can utilize both SSE and DSE events as both coincident events can be distinguished even in same detector. This improves the geometrical efficiency by a factor of two over current TGV II [7].

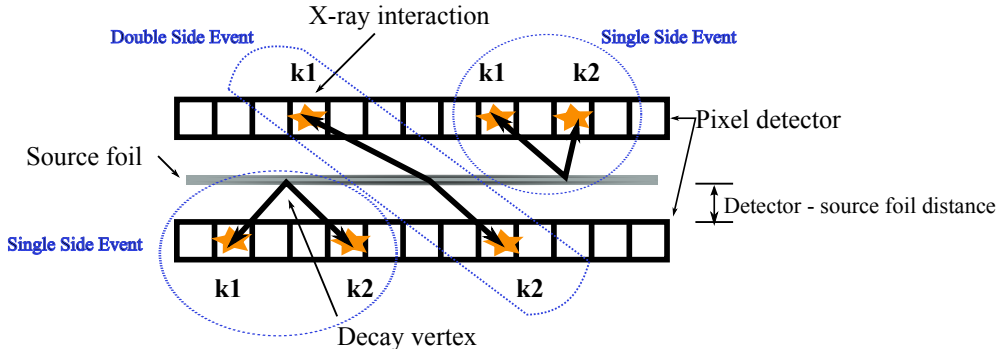


Figure 3.4: Schematic illustration of SPT detection unit. The good signature events in the pixel detector pair form either Single Side Events (SSE) or Double Side Events (DSE)

To estimate the efficiency of detection process in the SPT setup extensive simulations were performed by the collaboration. The simulations were done using ROOT VMC [51, 52] and GEANT4 [53]. The physics list used was the standard Geant4 EM process [54] and the DECAY0 code [55] was used for generating primaries for the simulations. Some of the important results obtained are presented here. The simulated SPT geometry was stack of two pixel detectors (with Si sensor arranged in face-to-face configuration) with enriched Cd foil as the decay source in between the detectors. The area of the pixel detector matches as that of Si Timepix ( $1.4 \text{ cm} \times 1.4 \text{ cm}$ ) and the Cd source foil had a dimension of  $1.2 \text{ cm} \times 1.2 \text{ cm}$ . The vertex of the decay considered was double 21 keV X-rays (from  $^{106}\text{Pd}$ ) emitted in full isotropic solid angle from a random point in the bulk of source foil. The valid signature events of decay were either Single Side Events or Double Side Events which can be identified in the above pixel detector configuration. The following parameters were studied in MC simulations: distance between detectors (detector - source foil gap, see Figure 3.4), Cd foil thickness, pixel pitch dimension and thickness of Si sensor. The preliminary results from this simulation studies were published in the article [7] by TGV collaboration.

The detection efficiency in SPT can depend on the detector to source foil distance (gap between the foil surface and detector surface). As the Cd foil and detectors are close to each other, more decay signature events pass through the detector volume (the detectors cover more solid angle of the decay path) and thus improves the detection efficiency. So two cases of source to detector distance were specially studied, namely Far-Geometry (FG) where detector-foil distance is 1 mm, and Close-Geometry (CG) where detector and foil surfaces are touching each other ( $\sim 1 \mu\text{m}$ ). From simulations performed with 50  $\mu\text{m}$  thick Cd foil and 2 mm thick Si sensor, in the case of FG, 12.71 % of the events were registered as good events. In the good events 44.11 % was DSE and 55.89 % was SSE. In the case of CG the total percentage of registered good events was 16.66 %, and 42.32 % of good events was DSE and 57.68 % was SSE. Foil thickness can also influence the detection efficiency of the  $EC/EC$  signature, as the X-rays can deposit in the foil itself. The calculated efficiencies for different source thickness is shown in Figure 3.5. Optimum thickness of the foil depends on the aim of the experiment. To increase the limit, the best option is 50  $\mu\text{m}$  foil thickness, while to detect the experimental signal, 20  $\mu\text{m}$  foil is most appropriate. A 30  $\mu\text{m}$  foil thickness could be a good compromise between both strategies.

The simulations for pixel pitch vs efficiency studies were performed with 2 mm thick Si sensor in CG using 50  $\mu\text{m}$  source foil for several pitch dimensions ( $16 \times 16$ ,  $32 \times 32$ ,  $64 \times 64$ ,  $128 \times 128$  and  $256 \times 256$ ). Obtained efficiencies for above pitch dimensions are the following: 14.03 % for  $16 \times 16$ , 16.64 % for  $32 \times 32$ , 18.09 % for  $64 \times 64$ , 17.91 % for  $128 \times 128$  and 16.66 % for  $256 \times 256$ . If the pixel pitch (single pixel area) is large, the chances for coincident events (SSE events) to register in same or adjacent clusters increases, making them indistinguishable, thus reducing the detection efficiency. As the pixel pitch is reduced, the loss percentage due to hits in the adjacent pixels decreases. Again, reducing the pixel pitch can decrease the efficiency as the cluster size (number of pixels fired) of the signature events increases and chances of energy loss due to under-threshold (for pixel electronics) events increases. The influence of Si sensor thickness on the efficiency is significant. Sensor thickness of 600  $\mu\text{m}$ , 1, 2, and 3 mm were studied and obtained efficiencies are 2.86 %, 11.03 %, 16.66 % and 18.74 %, respectively. If one consider the standard attenuation of 21 keV X-ray for above Si thickness, without considering any special geometry, the percentage of attenuation were 41.96, 59.63, 83.70 and 93.42 %, respectively for the above mentioned thicknesses. It can be seen that the geometry of the setup and need of coincidence detection influence the efficiency significantly. Also, a thicker sensor (2 mm or more) is desirable while standard pitch dimension ( $256 \times 256$ ) is reasonable.

Figure 3.6 shows the simulated distribution of distances between the coincident events from the decay in CG and FG. Figure 3.7 shows the distance distribution from background measurements (from underground) using Si Timepix detector. By comparing above mentioned distance distributions, it can be seen that the selection of double events hits where individual events are separated by a distance 0.7-4 mm rejects 75% of background events, rejecting 31.3 % and 33.5 % of  $2\nu EC/EC$  signals in Far-Geometry and Close-Geometry, respectively. By using such criterion, the overall S/B ratio can be improved by a factor

of  $\sim 2.7$ .

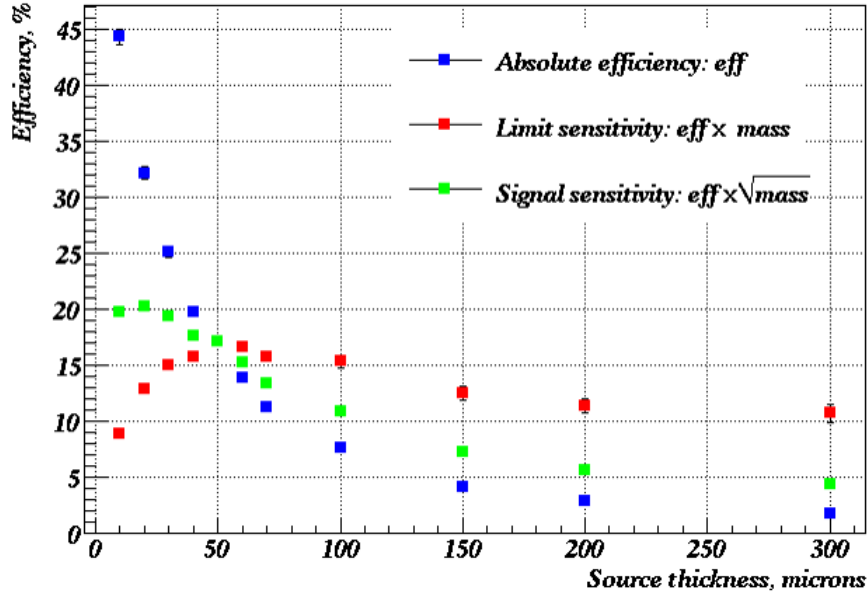


Figure 3.5: Simulated Efficiencies of  $^{106}\text{Cd}$   $2\nu EC/EC$  decay detection in the SPT cell (using Si Timepix detectors of dimension  $1.4\text{ cm} \times 1.4\text{ cm} \times 2\text{ mm}$ ) as a function of source foil thickness (mass normalized to 1 at  $50\text{ }\mu\text{m}$  foil thickness).

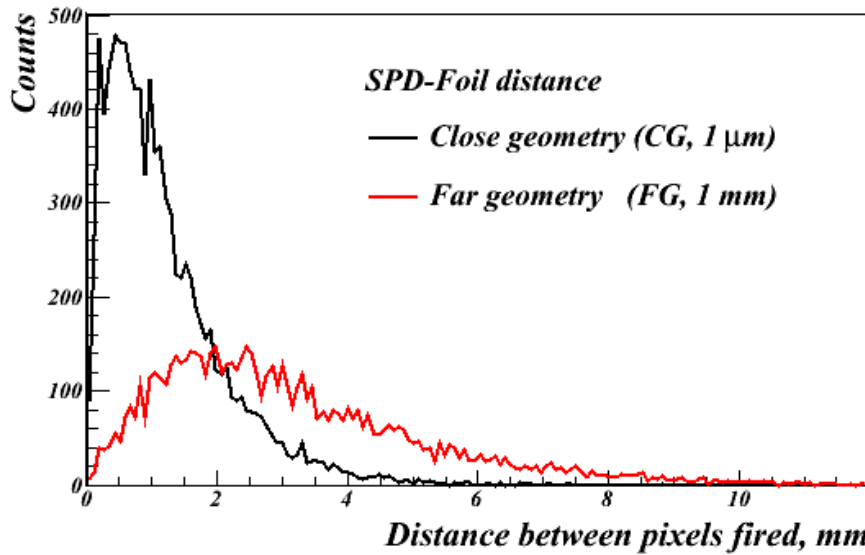


Figure 3.6: Simulated distance distribution between coincident X-rays (of  $^{106}\text{Cd}$   $2\nu EC/EC$  decay) interaction points. The mean distances between hit pixels are 3.2 and 1.2 mm for FG and CG, respectively.

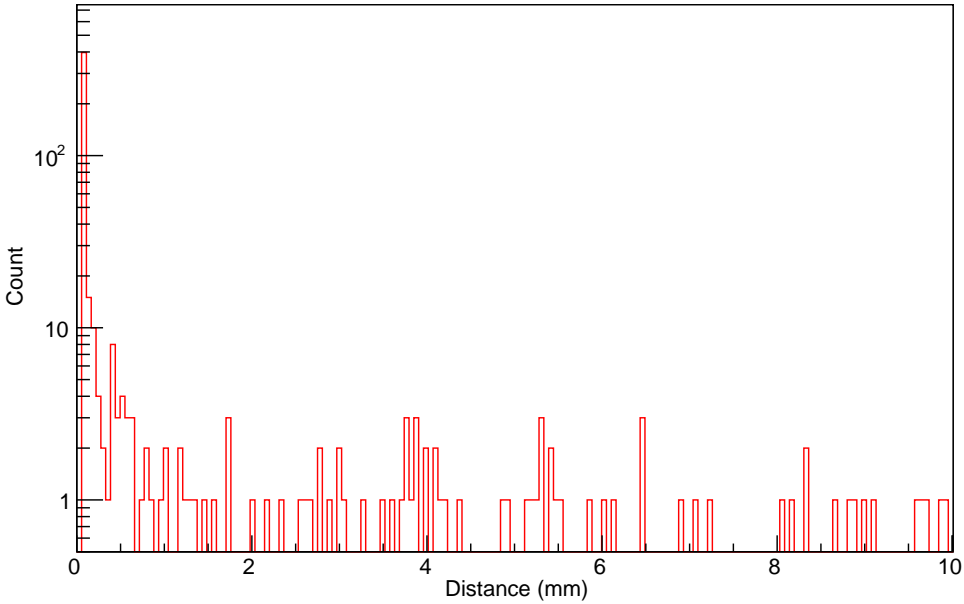


Figure 3.7: Distance distribution of background Single Side Events (SSE) measured using Si Timepix Single-Pixel-Detector in the underground laboratory.

### 3.3 COBRA

The COBRA (Cadmium Zinc Telluride 0-Neutrino Double-Beta Research Apparatus) experiment aims to study the double beta decay using large array of Cadmium Zinc Telluride (CZT) semiconductors [3]. Semiconductor detectors have very good energy resolution and particularly CZT can be operated in room temperature. Also, this experiment has source of decay elements in the detector itself. Of the known 35 double beta decay isotopes, CZT contains nine of them. The Table 3.1 shows the list of  $\beta\beta$  isotopes in CZT, their possible decay modes and percentage of natural abundance. The main focus is on the  $\beta^- \beta^-$  decay of  $^{116}\text{Cd}$ , due to its high Q-value, which is well above all the natural  $\gamma$ -rays background [3]. Other important isotopes in CZT are  $^{130}\text{Te}$  and  $^{106}\text{Cd}$ . The proposal is to have  $\sim 400$  kg of CZT crystal arrays with 90% Cd enrichment with  $^{116}\text{Cd}$ . The collaboration operates a small prototype setup in Laboratori Nazionali del Gran Sasso (LNGS) laboratory, Italy. The underground laboratory has 1400 meters of rock above it and the amount of uranium and thorium in the rocks are very low (thus low neutron flux). The muon flux in the laboratory is  $\sim 29 \text{ m}^{-2}\text{day}^{-1}$ .

The experiment COBRA is in the R&D stage and major activity is concentrated on the use of Co-Planar Grid detector (CPG) technology in the experiment. A prototype setup consisting of 64 CPG detector units ( $1 \text{ cm}^3$  crystal) arranged in four layers, each holding  $4 \times 4$  detectors in a Delrin support has been installed and data taking is undergoing. The Figure 3.8 shows a single CPG detector unit and Figure 3.9 shows one layer of the setup comprised of 16 units. The CPG detectors are kept inside a multi-layer shielding (see Figure 3.10). The inner most layer of shielding is made of ultra-pure copper. Above that

Isotope	Q value (keV)	Natural abundance (%)	Decay mode
$^{70}\text{Zn}$	1001	0.62	$\beta^-\beta^-$
$^{114}\text{Cd}$	534	28.7	$\beta^-\beta^-$
$^{116}\text{Cd}$	2809	7.5	$\beta^-\beta^-$
$^{128}\text{Te}$	868	31.7	$\beta^-\beta^-$
$^{130}\text{Te}$	2529	33.8	$\beta^-\beta^-$
$^{64}\text{Zn}$	1096	48.6	$\beta^+/EC$
$^{106}\text{Cd}$	2771	1.21	$\beta^+\beta^+$
$^{108}\text{Cd}$	231	0.9	$EC/EC$
$^{120}\text{Te}$	1722	0.1	$\beta^+/EC$

Table 3.1: List of double beta decay isotopes in CdZnTe, their possible decay modes and natural abundance.

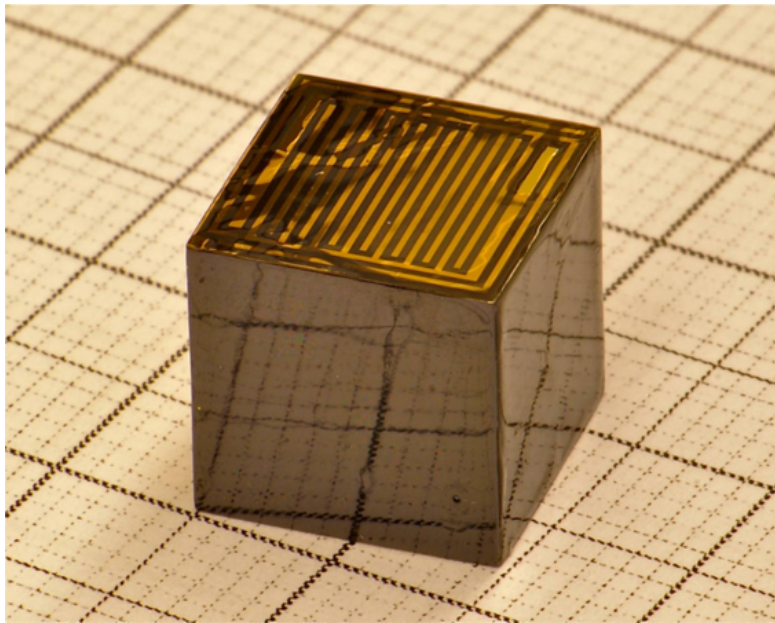


Figure 3.8: Co-Planar Grid (CPG) detector used in the COBRA experiment.

is low activity lead shielding. A Radon tight enclosure with nitrogen flushing covers the lead shielding. This inner shielding is covered by an EMI shielding. Finally, the outer most layer of shielding is made from borated polyethylene against neutron flux. The background rates as low as 1 count/keV/kg/y were reached in the 2.8 MeV region (see Figure 3.11). The collaboration is currently investigating the use of  $2 \times 2 \times 1.5 \text{ cm}^3$  CPG detectors for improving the detection efficiency.

Simulations were also performed by the collaboration for the feasibility of CdTe pixel detectors in COBRA experiment. CdTe pixel detector of dimension  $1 \times 1 \times 1 \text{ cm}^3$  was considered with three cases of pixel matrix sizes  $45 \times 45$  ( $220 \mu\text{m}$  pitch),  $90 \times 90$  ( $110 \mu\text{m}$  pitch) and  $180 \times 180$  ( $55 \mu\text{m}$  pitch). Primary particle used in the simulation was  $0\nu\beta\beta$  from  $^{116}\text{Cd}$ , and the vertex of decay was in the detector bulk. The parameters under study were track length (stopping range), cluster size and energy deposition in pixels.

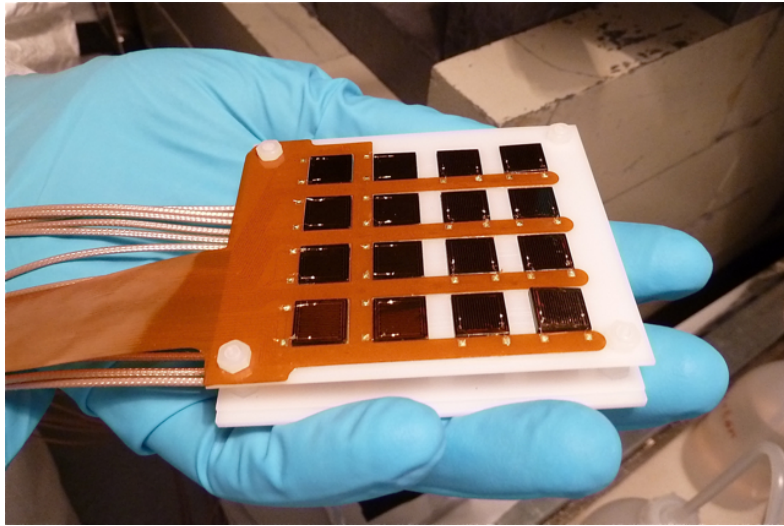


Figure 3.9: CPG detector layer ( $4 \times 4$  CdTe detectors) on Delrin support.

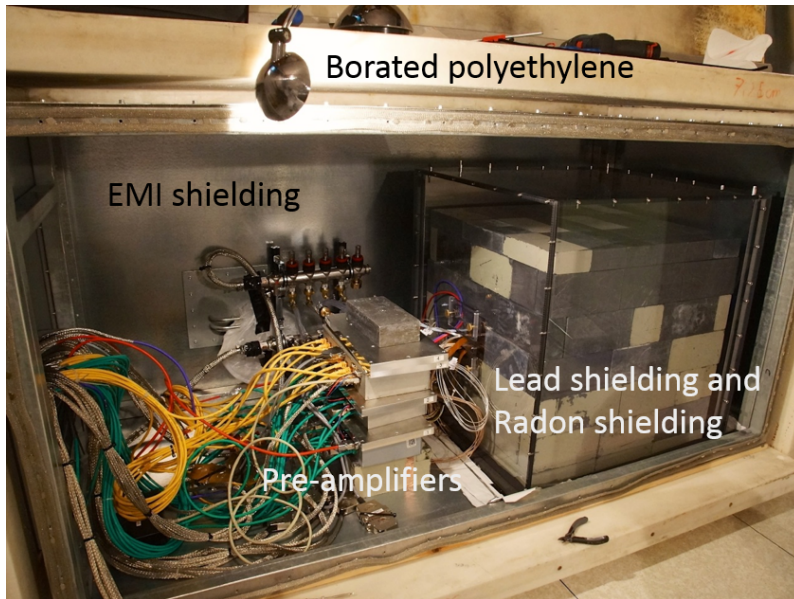


Figure 3.10: COBRA shielding constructed in the LNGS underground laboratory.

In Figure 3.12, the stopping ranges of double electrons (from  $0\nu\beta\beta$  decay of  $^{116}\text{Cd}$ ) of energy  $\sim 2.8$  MeV are shown for all three pixel pitches. The mean distance between stop and emitting point was found to be 4.25 mm which is as expected, same for all three pitch dimensions. The cluster sizes (number of hit pixels) of such signature events for three pixel pitches ( $220\ \mu\text{m}$ ,  $110\ \mu\text{m}$  and  $55\ \mu\text{m}$ ) are shown in Figure 3.13. The average cluster size in  $55\ \mu\text{m}$  pitch detector was  $\approx 30$  pixels whereas in  $110\ \mu\text{m}$  it was  $\approx 14$  pixels. The pixel size could be used as a strong criterion for identifying the signature events.

$0\nu\beta\beta$  signal is given by two electrons emitted from common pixel with two independent tracks for both electrons. MC simulations were performed to see if there is possibility

Figure 3.11: Result obtained from COBRA prototype unit (64 CPG detectors) after collection of  $82.2 \text{ kg}^*\text{days}$  of data. Background rate as low as 1 count/keV/kg/y was achieved in the 2.8 MeV region.

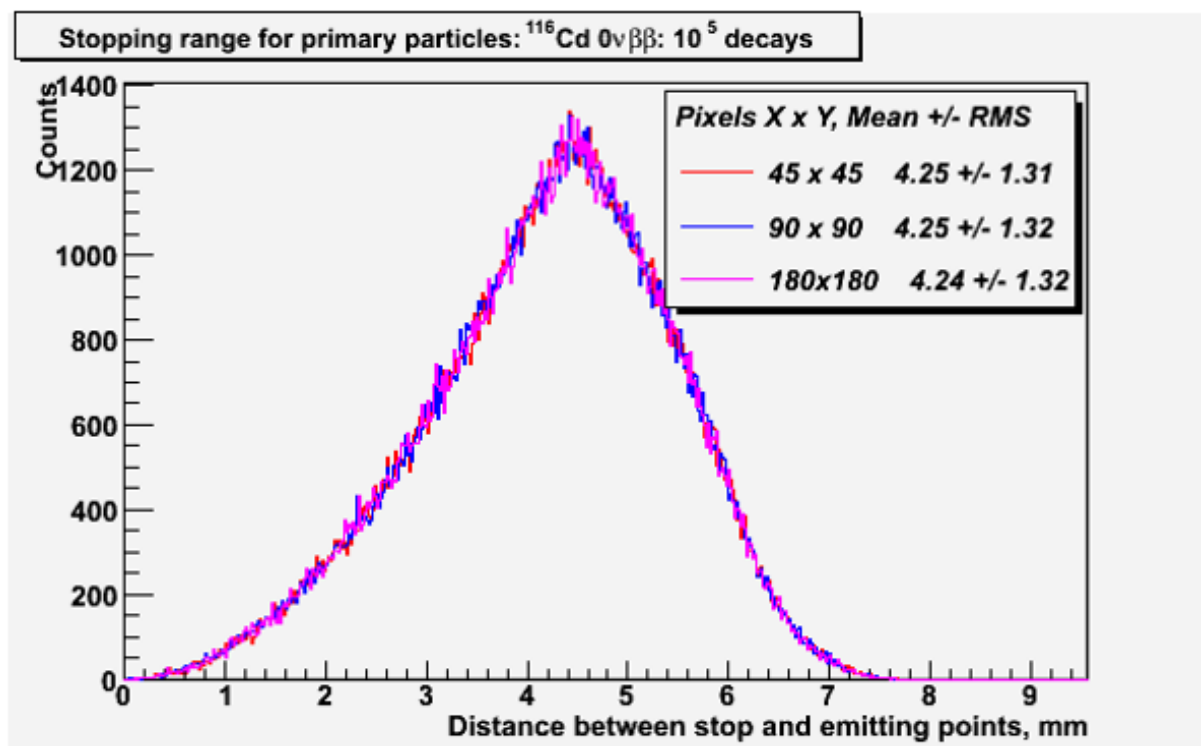


Figure 3.12: Simulated stopping ranges for primary particle (double electron of energy 2.8 MeV) in  $0\nu\beta\beta$  decay of  $^{116}\text{Cd}$  for three different pixel pitch configurations.

to distinguish the end pixels of both electron tracks. Interaction of electrons and its deposition of energy along the path is well defined by Bragg curve. Simulation results of energy deposited on the start, passed and the end pixels are shown in Figures 3.14 and 3.15 for pixel pitches  $110 \mu\text{m}$  and  $55 \mu\text{m}$ , respectively. The mean energy deposition in the end pixels is substantially higher than the other pixels. For a pixel pitch of  $55 \mu\text{m}$  the average energy deposited in the end pixels was  $\sim 454 \text{ keV}$  and 95.3 % of end pixel

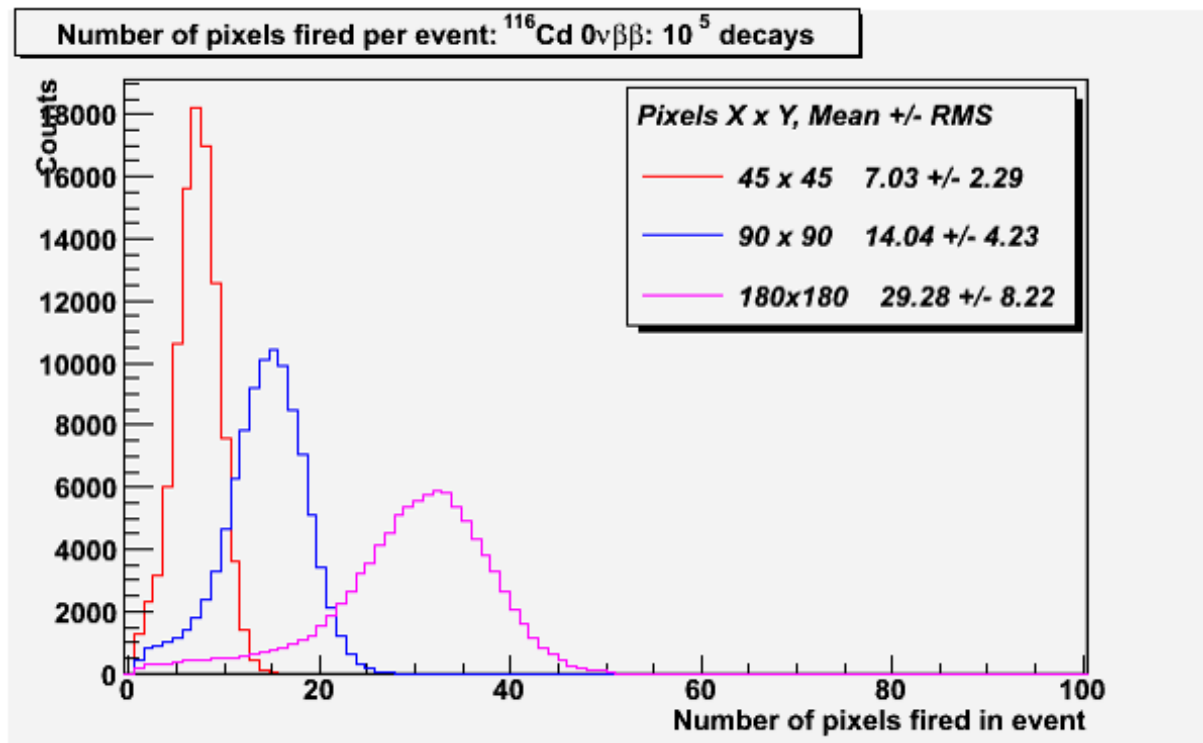


Figure 3.13: Simulated cluster sizes (total pixels in the event) for the  $0\nu\beta\beta$  decay (double electron of energy 2.8 MeV) of  $^{116}\text{Cd}$  in pixel detectors with different pixel pitches.

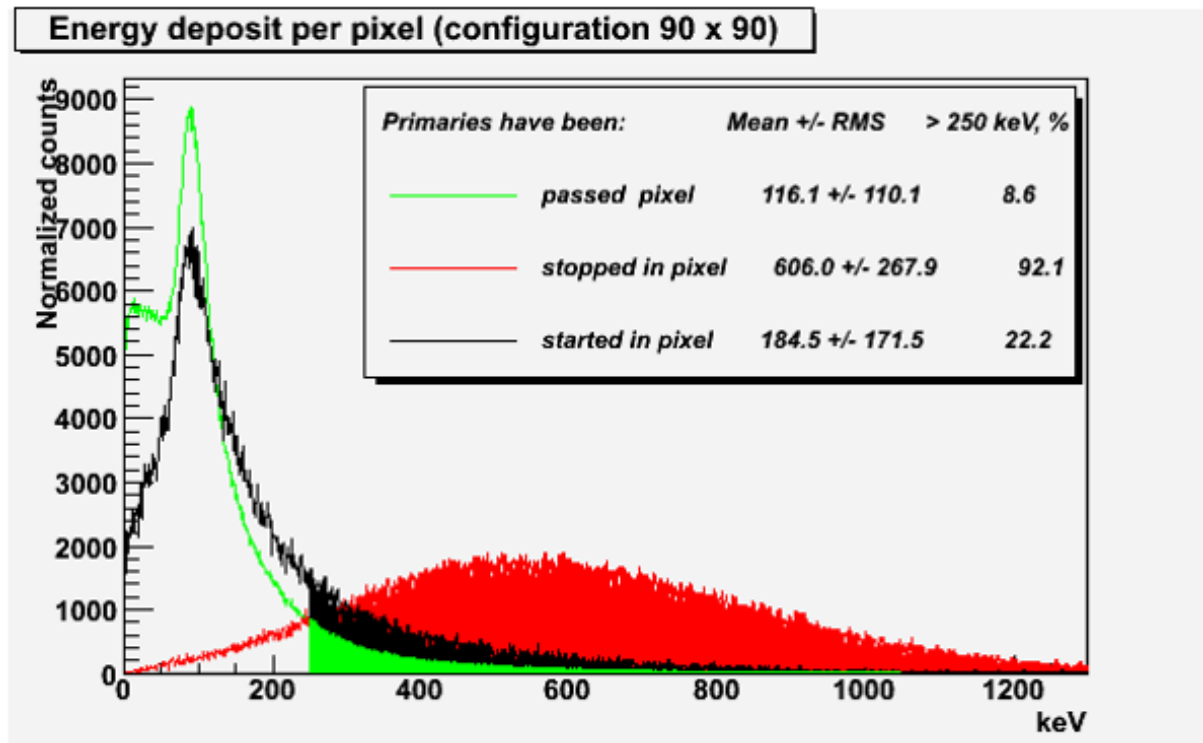


Figure 3.14: Distribution of energy deposited in start, passed and stopped pixels for 110  $\mu\text{m}$  pitch configuration.

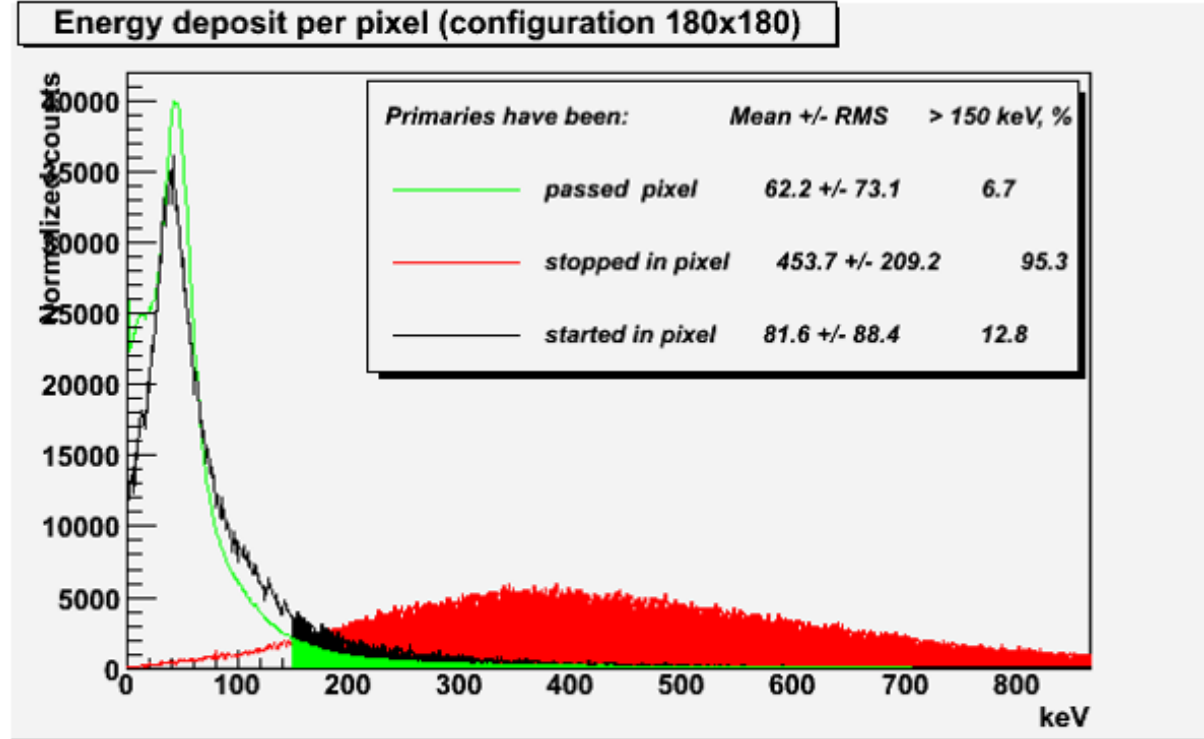
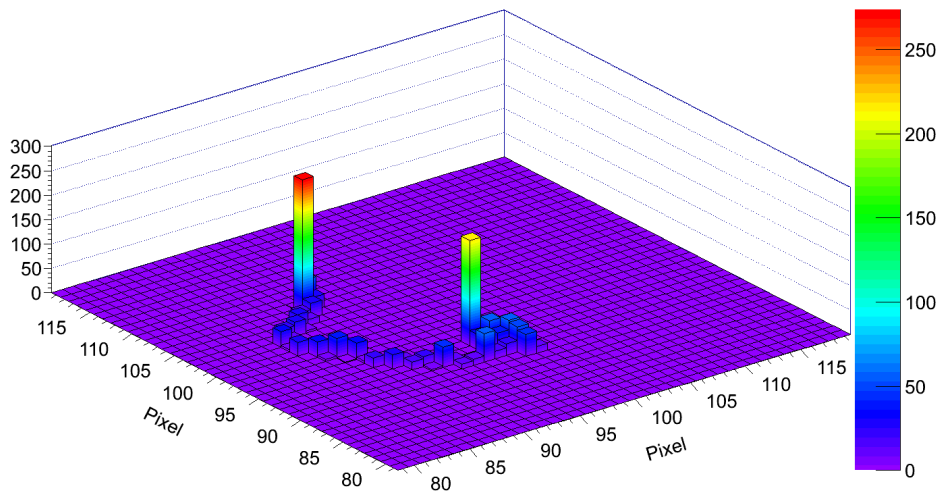
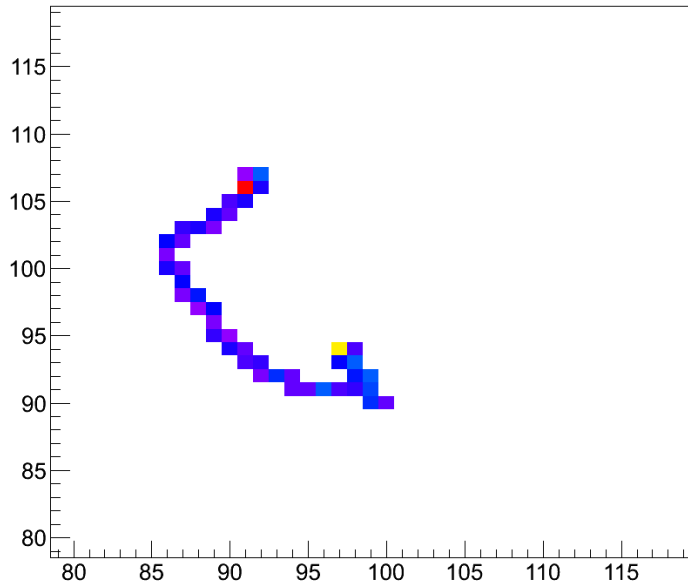


Figure 3.15: Distribution of energy deposited in start, passed and stopped pixels for 55  $\mu\text{m}$  pitch configuration.

events had energy deposition above 150 keV. While for the start pixel and intermediate (passed) pixels only 19.5 % of the events were above 150 keV. So, it is possible to identify in most cases the end pixels of electron tracks. The Figure 3.16 shows a simulated track which confirms the above argument. The tracks have well distinguishable end points with higher energy deposition than other pixels. A single electron can also create such a track, but the background electron events in the region of interest (2.5-3 MeV) is negligible.



(a) 3D view of the tracks.



(b) 2D plot of the tracks.

Figure 3.16: A simulated track of  $0\nu\beta^-\beta^-$  decay event from  $^{116}\text{Cd}$  generated in CdTe pixel detector of pitch  $55\ \mu\text{m}$ .

# Chapter 4

## Timepix pixel detector

Use of pixel detector in particle physics was consequence of different factors such as the convincing results obtained from CCD usage (in the NA32 experiment at CERN [56] and the SLD (SLAC Large Detector) collider experiment at SLAC [57, 58]), advancements in CMOS chip technology, success in the processing technology for Si micro-strip detectors [59]. CCD detector had lower read-out speed which limited several applications and physicists were looking for an alternative. Initial studies for the use of pixel detectors in particle physics were initiated for the vertex detectors in Superconducting Super Collider [60, 61] and at CERN [62, 63] by RD19 collaboration [59]. Pixel detectors in particle physics were used initially for vertex detection in collision experiments. Advantages of pixel detectors were their good spatial resolution, timing and triggering, long term operation performance and radiation hardness [59]. As the technology matured and enough experience obtained with the pixel operations, applications in imaging emerged. In imaging applications high dynamic range ( $\sim 15$  bits), high frame rate, low dead time, low threshold and low threshold dispersion were mattered the most [64]. The growth of pixel technology is marked by the increase in the area of device, lower threshold dispersion in pixels (difference in operating characteristics due to parameter variations of transistors in semiconductor), threshold compensation, sophistication in the pixel circuit, etc.

Pixel detector has two main functional parts, the readout ASIC and detection medium attached to it. Pixel detectors can be broadly classified into monolithic and hybrid type. In monolithic pixel detectors the readout electronics and sensors are in one substrate. Additionally, such system can achieve smaller pixel sizes ( $\sim 20 \mu\text{m} \times 20 \mu\text{m}$ ), low input capacitance, better signal amplification, low noise operation and low power consumption [65]. There are different approaches in monolithic branch such as CMOS active pixels, DEPFET pixels, etc. [66, 67].

Unlike monolithic pixel detectors where pixel readout and sensing element is on the same substrate, hybrid pixel detectors have them in separate wafers. The readout and the sensor are connected together by flip-chip bonding. The flip-chip technology was introduced by IBM in 60s, where two substrates are connected together by bump-bonds. This approach has the advantage that both pixel circuit and sensing material can be optimized separately. Hybridization helps to use high 'Z' elements as sensor material. Figure 4.1 shows the schematic illustration of hybrid pixel detector.

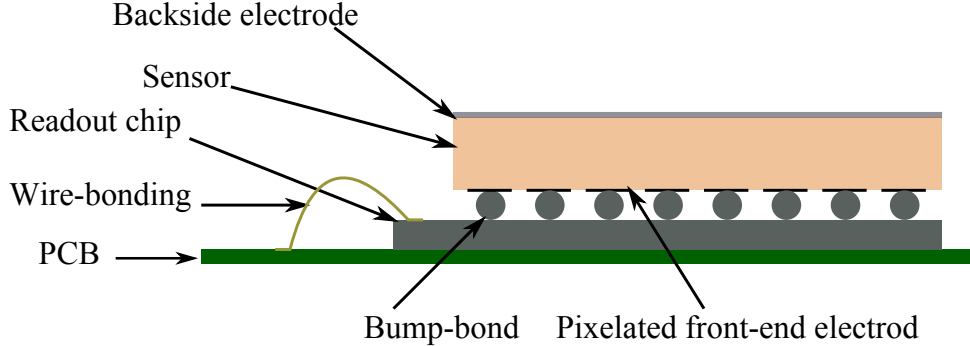


Figure 4.1: Illustration of hybrid pixel detector attached to a Printed Circuit Board (PCB).

There are different successful pixel detector systems around the world now. Each pixel system has its own characteristics and operating principle. For example, the ATLAS detector has  $50\text{ }\mu\text{m} \times 400\text{ }\mu\text{m}$  pixels and pixel height information (digital output) is generated on the hit pixels [64]. It has threshold dispersion of  $600\text{ e}^-$  without compensation and  $50\text{ e}^-$  with 7 bit threshold adjustment [65]. The CMS pixel detector has  $100\text{ }\mu\text{m} \times 150\text{ }\mu\text{m}$  pixels with analog readout [64]. The PILATUS II CMOS readout chip has  $172\text{ }\mu\text{m} \times 172\text{ }\mu\text{m}$  pixels, charge sensing preamplifier, single level comparator, counter and control logic in each pixels. Threshold dispersion of  $30\text{ e}^-$  is achieved using 6 bit DAC in each pixels. It has a dynamic range of 20 bit and a frame rate of 200 Hz [68].

## 4.1 Timepix Detector

Timepix belongs to the class of hybrid pixel detectors. Timepix readout chip was derived from the Medipix2 CMOS ASIC by Medipix collaboration [69] at the request of the EUDet collaboration [70]. The chip is intended as readout system for different kinds of radiation detectors such as semiconductor, gaseous time projection chambers, etc. The notable features of Timepix are summarized as follows:

- ◊  $256 \times 256$  pixels of size  $55\text{ }\mu\text{m} \times 55\text{ }\mu\text{m}$ .
- ◊ Choice of sensor material and bias polarity (both electron and hole collection possible).
- ◊ Pixel-wise energy threshold adjustment for uniform performance of the whole detecting area.
- ◊ Three different modes of operation per each pixel
  - \* Medipix (single particle counting)
  - \* Time Over Threshold or TOT (spectroscopic mode)
  - \* Time Of Arrival or TOA (time coincidence).

A detailed description of Timepix is covered in reference [4]. The Timepix pixel detectors have broad range of applications in diverse fields such as life science [73], material testing [74], study of cosmic radiation [75, 76], etc. A network of Timepix detectors was also installed around the ATLAS detector to monitor the radiation environment [77]. The experimental physics group at IEAP, CTU in Prague has proposed to use such progressive technology in double beta decay experiments TGV and COBRA. A brief description of Timepix ASIC follows in the next section.

## 4.2 Timepix pixel cell

Each pixel in the Timepix ASIC can be considered as a full spectroscopic channel having charge sensing amplifier, threshold discrimination and digitization. The pixel electronics can be broadly classified into analog and digital section. Schematic illustration of Timepix pixel electronics is given in the Figure 4.2.

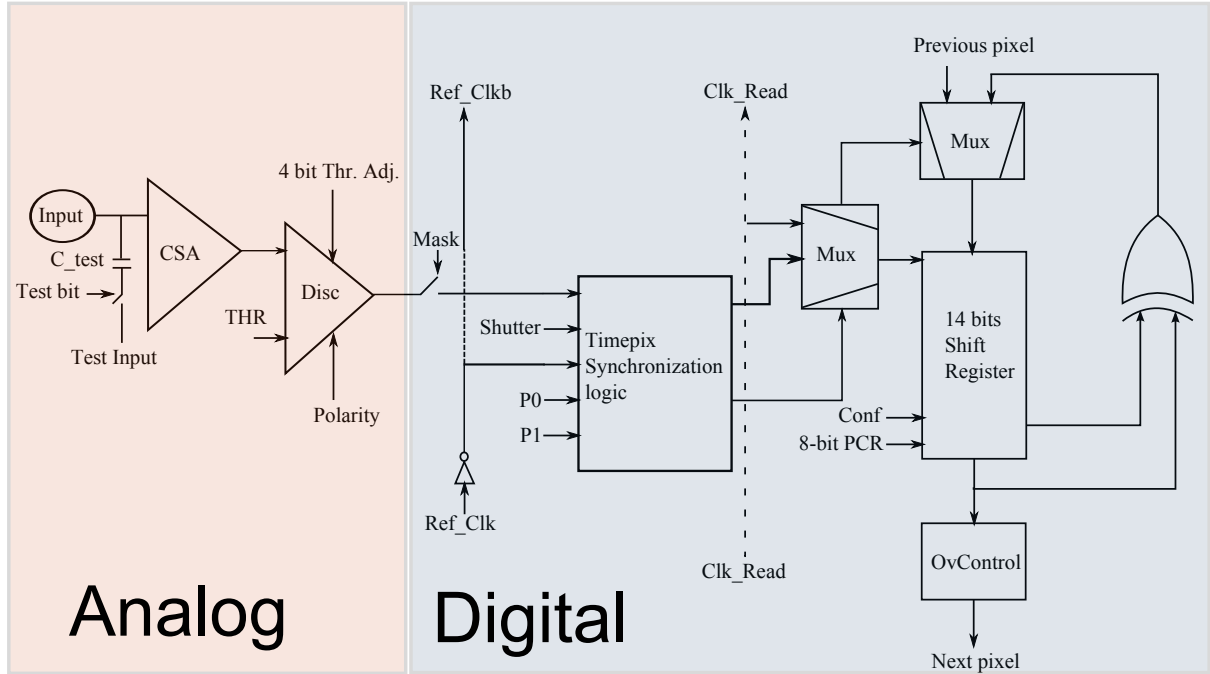


Figure 4.2: Schematic of Timepix pixel electronics [4].

### 4.2.1 Analog section

Main constituents of the analog section are test pulse circuit, Charge Sensitive Amplifier (CSA) and discriminator with threshold equalization. The test pulse circuitry is a simple capacitor ( $\sim 8$  fF) connected to CSA input, through which the test pulse is applied to amplifier. The CSA circuit integrates the input charge for both polarities, shapes the pulse and compensate for input DC leakage current. Simplified block diagram of CSA is given in Figure 4.3 and its response is shown in Figure 4.4. CSA operation is controlled

by five Digital to Analog Converters (DAC), and by configuring these DACs ( $I_{PreAmp}$ ,  $I_{KRUM}$ ,  $V_{FBK}$ ,  $V_{CAS}$  and  $V_{GND}$ ) the amplifier response is tuned.  $I_{PreAmp}$  provides bias current for the CSA and controls the gain of the amplifier thus the amplitude of the pulse.  $I_{KRUM}$  affects the discharge time of the output pulse (pulse shaping).  $I_{KRUM}$  has inverse relationship to discharge time.  $I_{KRUM}$  can compensate positive leakage current up to  $\sim I_{KRUM}$  (in hole collection mode), negative leakage current up to  $\sim I_{KRUM}/2$ . Even though, it is desirable to have longer discharge time to have better energy resolution, pile-up can occur if  $I_{KRUM}$  is set to very low in some applications. If the detector is noisy the  $I_{KRUM}$  has to be set to a higher value which results in fast discharge (eg. for  $I_{KRUM}$  value 1.5 nA return to zero takes 10  $\mu$ s). Gain of the CSA is sensitive to variations in both  $I_{PreAmp}$  (direct relationship) and  $I_{KRUM}$  (inverse relationship). The  $V_{CAS}$  helps to reduce input capacitance of CSA, thus improves S/B ratio with the expense of reduced dynamic range. Input node DC voltage (voltage on the bump-bonds) is set through  $V_{GND}$ . The difference between  $V_{GND}$  and the input voltage ( $V_{in} - V_{GND}$ ) is amplified in the CSA. The output baseline (DC voltage) is set by  $V_{FBK}$  which controls the output dynamic range of the Charge Sensitive Amplifier. The full output range of 900mV is explored by setting  $V_{FBK}$  to 1.5 V in hole collection mode and 0.6 V in electron collection mode.

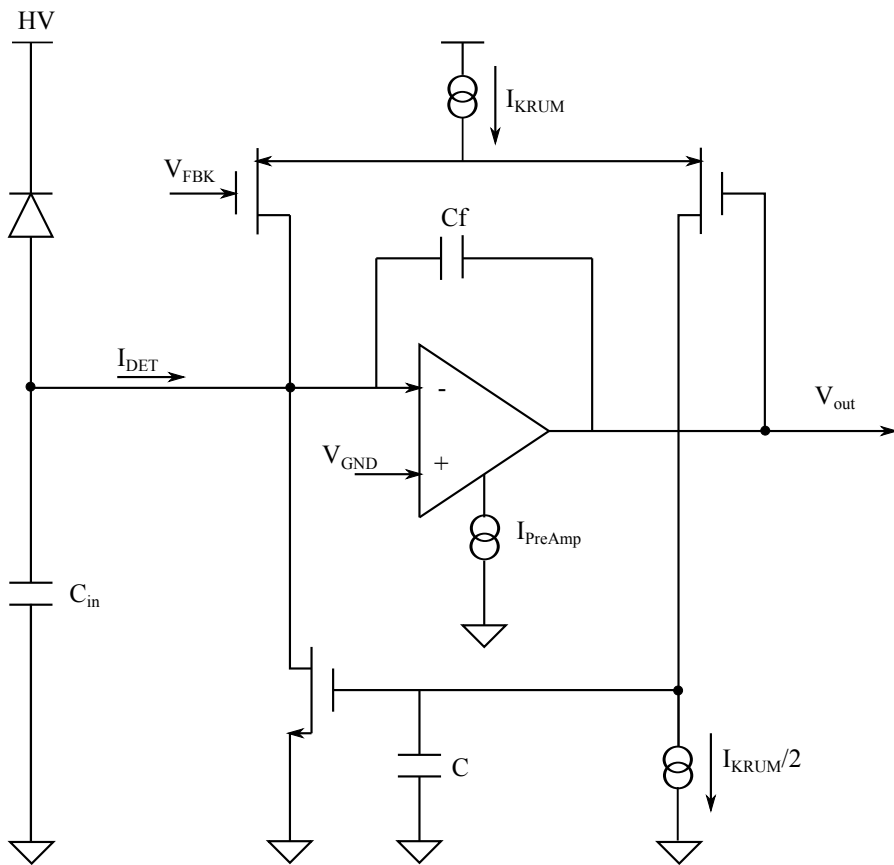


Figure 4.3: Block diagram of Timepix Charge Sensitive Amplifier.

Signal from Charge Sensitive Amplifier is DC coupled to discriminator (see Figure 4.5 for a simplified block diagram). The discriminator has five main blocks: a multiplexer with polarity pin, Operational Trans-conductance Amplifier (OTA), four bit threshold

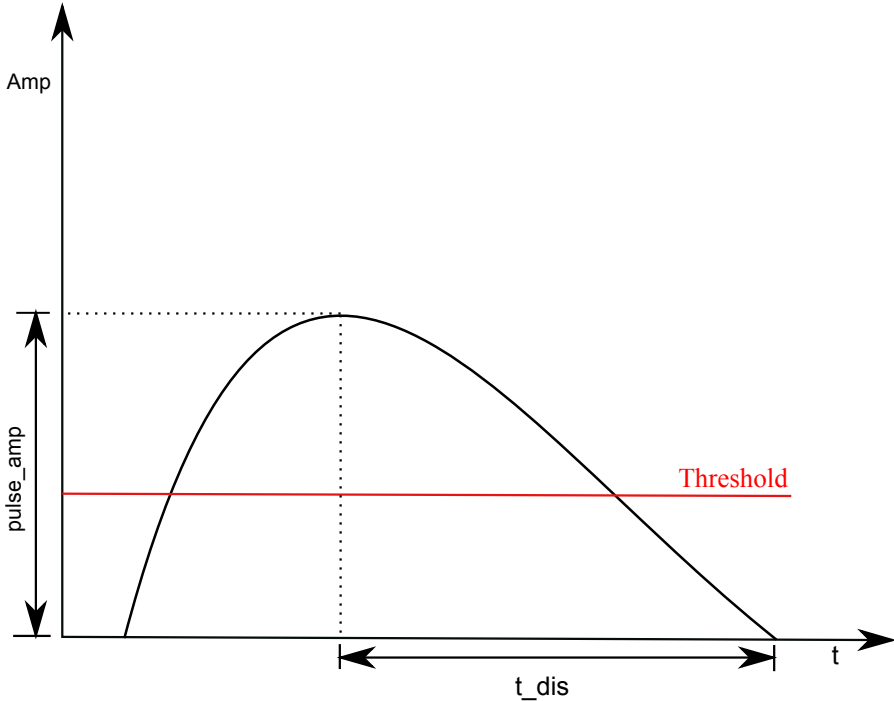


Figure 4.4: Timepix Charge Sensitive Amplifier response to input charge.

adjustment circuitry, FastDiscLogic circuitry (FDL, a zero crossing discriminator circuitry) and the hysteresis compensation circuitry. The discriminator circuit is controlled by DACs  $V_{THL}$ ,  $I_{DISC}$ ,  $V_{THS}$  and  $I_{HYST}$ . The multiplexer keep the discriminator output logic independent of input polarity by interchanging the inputs of the OTA. Thus discriminator can work in both polarities (hole or electron collection mode). Discriminator threshold is tuned by the  $V_{THL}$  which set the threshold for input to OTA. OTA converts input voltage signal (from CSA) into current which is compensated in the next stage using configurable current sources. OTA has a common mode threshold of 600mV, thus the operational input range is limited from 0.6 to 2.2 V.  $I_{DISC}$  gives the bias current for discriminator circuit and controls the gain of the OTA.

Bump bonding can make non uniform pad capacitance thus different noise in different pixels. Additionally, local transistor parameter mismatches and power distribution voltage drops can create threshold variations among the pixels. Threshold equalization circuit has four selectable current sources (with output currents  $I_{th}$ ,  $I_{th}/2$ ,  $I_{th}/4$  and  $I_{th}/8$ ) to minimize pixel to pixel threshold variations, where  $I_{th}$  can be tuned between 0 - 50 nA by adjusting the DAC called  $V_{THS}$ . Current generated by these four sources are added to the OTA output current before feeding to the FDL circuit. These individual current sources are selected by the appropriate bits in pixel configuration register (PCR) in each pixels to generate different levels of compensation. FDL circuit generates the output pulse when it detects the zero crossing. Hysteresis circuit eliminate high frequency pulses at the discriminator output (controlled by  $I_{HYST}$ ) that might upset following circuitry.

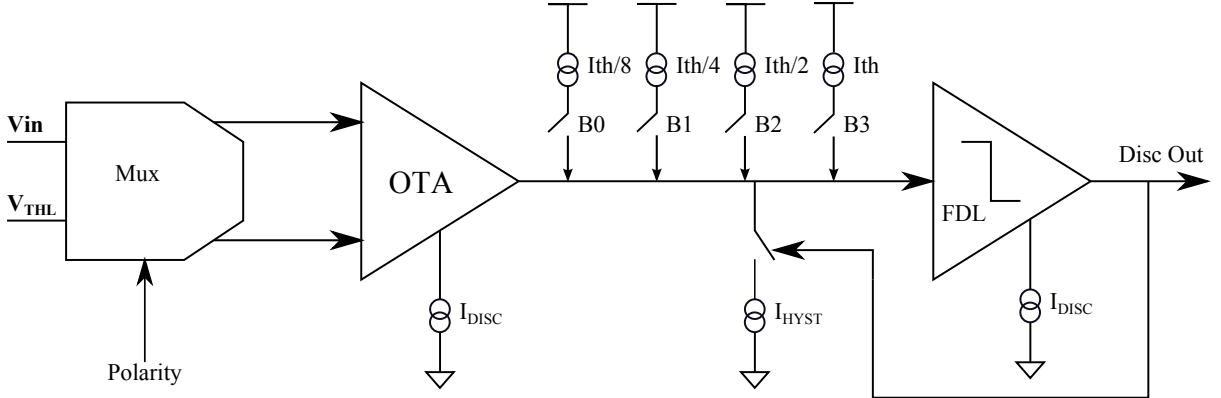


Figure 4.5: Block diagram of discriminator.

#### 4.2.2 Digital section

The digital part of the pixel contains pixel configuration register (PCR), 14 bit shift register/counter and Timepix synchronization logic. The eight bit pixel configuration register contains bits which control the pixel behavior. It contains the threshold equalization configuration, mode selection bits and a bit to mask pixel (stops further processing of the signal in the digital side). With appropriate configuration each pixel can operate in three different modes known as 'Time of Arrival' (TOA), 'Time Over Threshold' (TOT) and 'Medipix'. The clock signal and shutter signal are given to each pixel (in daisy chain on each column) externally. The counter starts counting (according to the mode setting) when there is output signal from discriminator and if the shutter signal is active. The 14 bit shift register can count up to 11810.

The different modes of operation are illustrated in the Figure 4.6. In the Medipix mode, pixel count once every time the signal is over the threshold. This mode is suitable for photon counting. In TOT mode the counter count for the time when the signal is above the threshold. In this mode pixel can measure the energy deposited, as the CSA discharge time depends on the input charge. In TOA mode the counter start counting from the moment the signal crosses the threshold till the end of the shutter. This mode is useful to check the coincidence of the events. Each pixel can be independently configured in any of the modes but it cannot work in more than one mode at a time.

### 4.3 Timepix periphery and readout

The periphery section of the Timepix ASIC contains (see Figure 4.7) all the DACs to operate the pixel circuits, Input/output units, 256 bit Fast Shift Register (FSR) and analog buffers. Most important are the DACs which provide necessary voltage or current for the proper functioning of the pixel circuits. There are eight 8-bit linear current DACs, four 8-bit linear voltage DACs and one 14 bit linear voltage DAC ( $V_{THL}$  for threshold setting). Analog buffers are used for several analog blocks of the chip and  $I_{BuffA}$  and  $I_{BuffB}$  manages the biasing of these buffers.  $I_{LVDS_{tx}}$  and  $V_{Ref\,LVDS_{tx}}$  are the DACs for LVDS circuitry. Table 4.1 lists all the DACs and brief description of their functions.

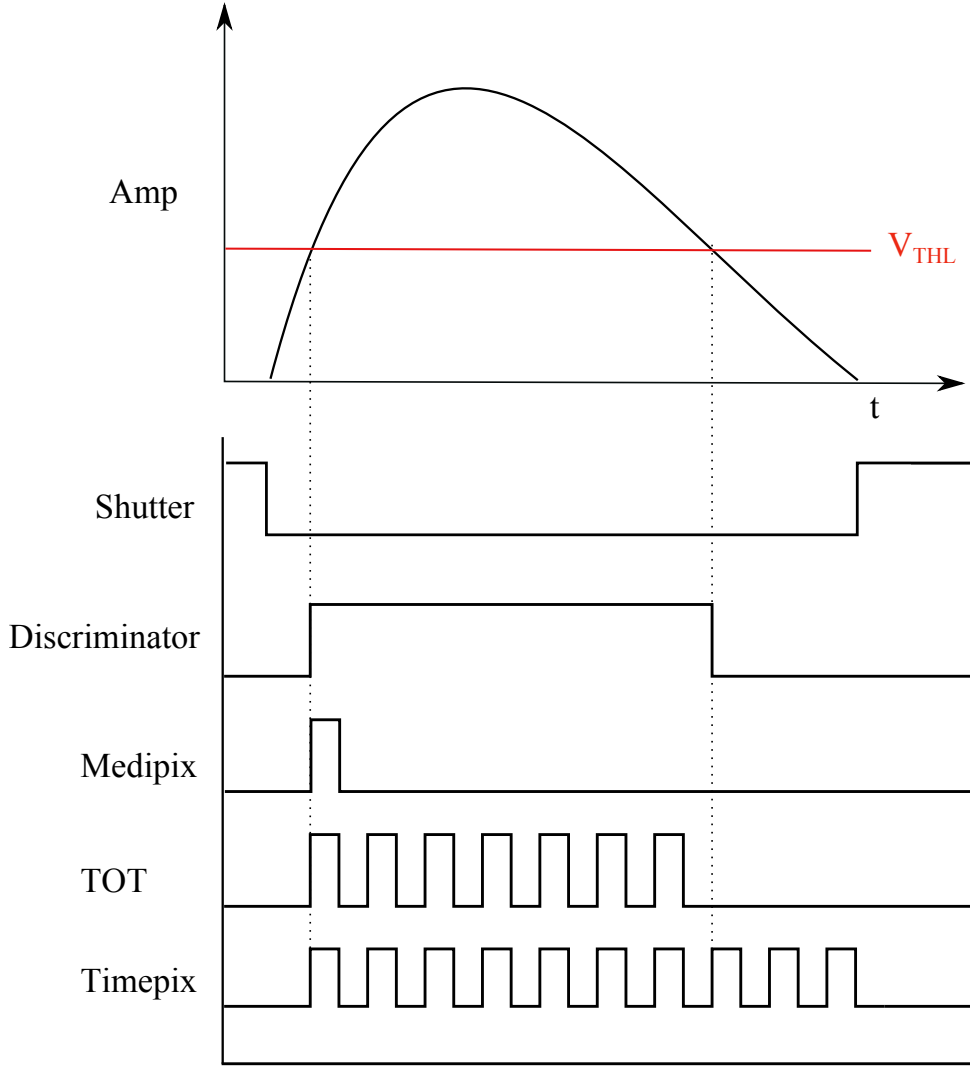


Figure 4.6: Illustration of Timepix pixel operation modes.

Input/output circuitry (Serial LVDS or parallel CMOS readout) is situated in this area, too. The serial readout time is 9.17 ms and parallel readout time is 287  $\mu$ s at 100 MHz clock. The dead time of the Timepix detector is dominated by the frame readout time. Timepix has a maximum analog power consumption of 440 mW (6.5  $\mu$ W/pixel) and maximum digital power consumption of  $\sim$  450 mW (7  $\mu$ W / pixel) at clock frequency of 80 MHz. In order to operate the Timepix pixel detector, USB readout system developed by Medipix group at IEAP, CTU in Prague is used. The readout system FITPix can read up to 80 frames per second from a single Timepix unit [71]. Figure 4.8 shows the FITPix unit connected to Timepix detector. Pixelman software package is used to perform equalization and calibration and as the DAQ software [72].

## 4.4 Equalization and calibration of Timepix

Before using the Timepix detectors it must be equalized and a proper calibration must be prepared. Equalization is the process of compensating the pixel-wise difference in the

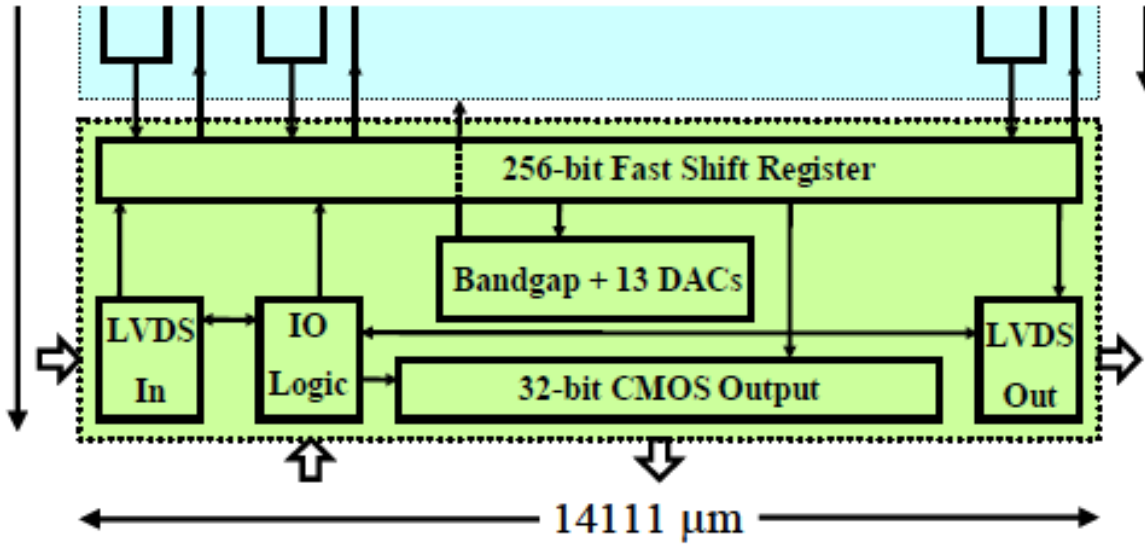


Figure 4.7: Schematic illustration of Timepix periphery [4].

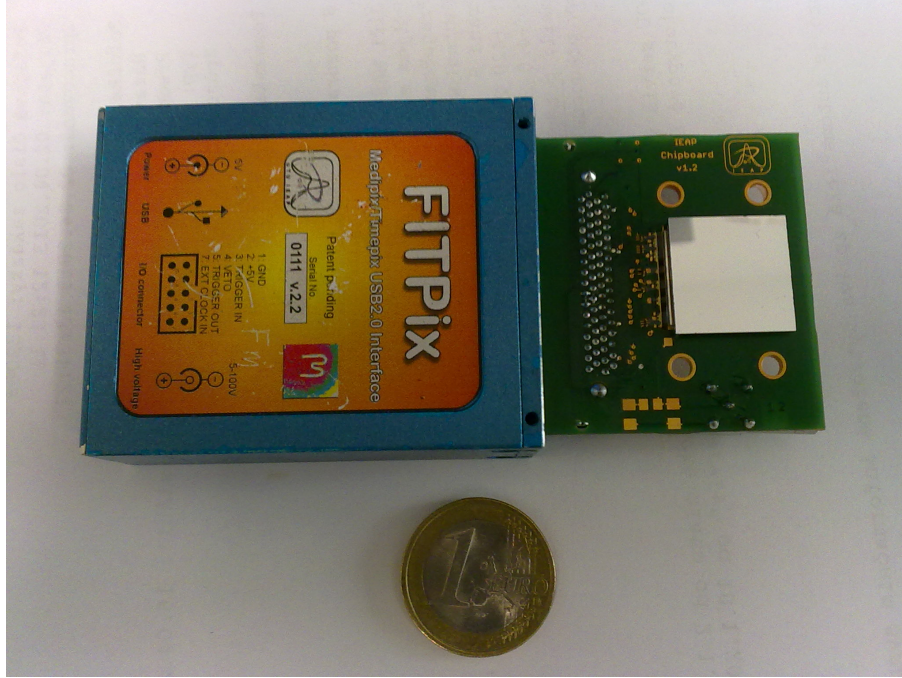


Figure 4.8: FITPix USB readout module.

response caused by parametric variations in the pixels. Equalization is done by finding the right configuration bits (4-bits stored in the PCR). This process also optimizes the value of  $V_{THS}$  for least threshold dispersion across the detector. The un-equalized threshold variation is  $\sim 240$  e $^-$  rms and after equalization it reduces to  $\sim 35$  e $^-$  rms. Minimum detectable charge before equalization and after equalization are  $\sim 1600$  e $^-$  and  $\sim 650$  e $^-$ , respectively. To use the Time Over Threshold mode (spectroscopic) Timepix detectors should be calibrated. All other modes can be used without an energy calibration. Cali-

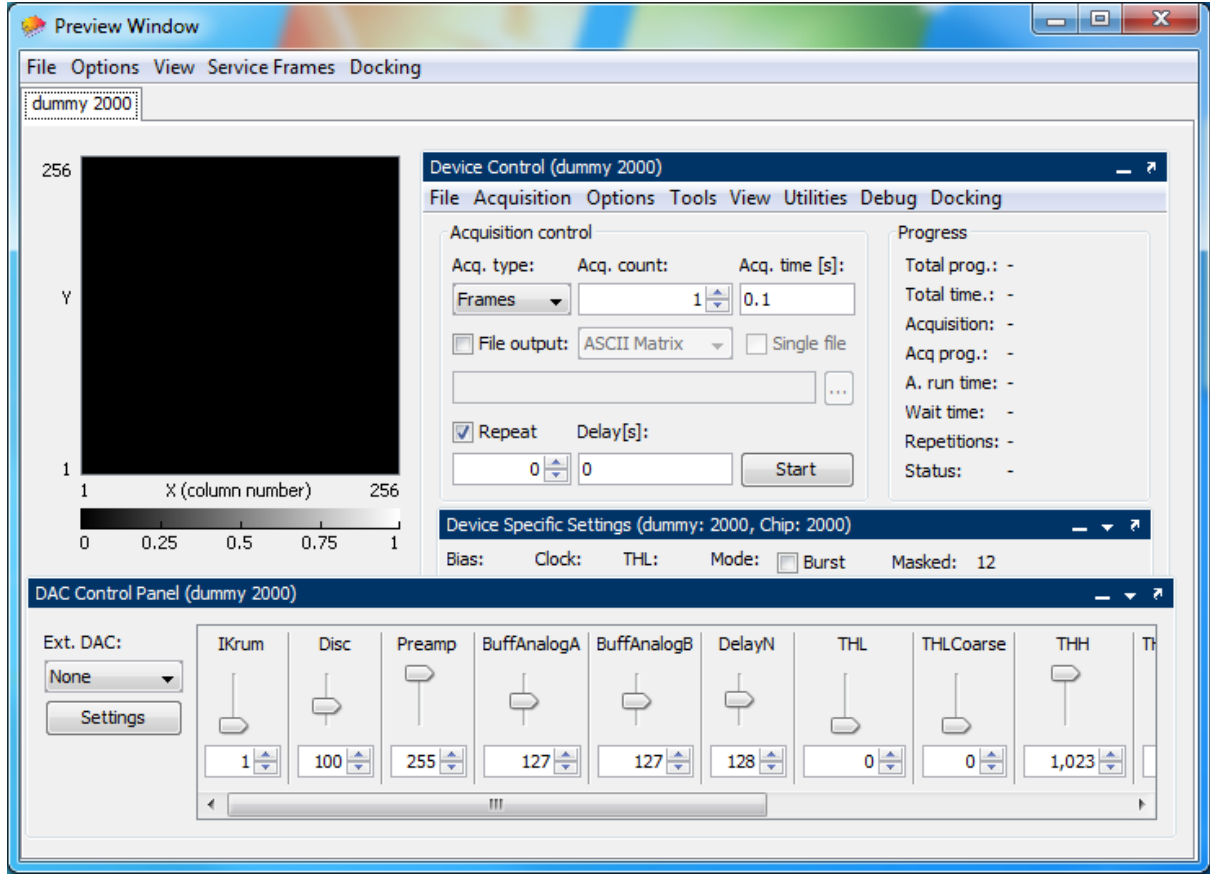


Figure 4.9: Example of Pixelman software Graphical User Interface.

bration is performed for each pixel since each pixel has its own front-end electronics and the response can vary pixel by pixel. The calibration procedure is explained in the publications [78], [79] and [80]. The relationship between TOT count and energy ( $E$ ) can be described by a nonlinear surrogate function as illustrated in Figure 4.10. The calibration function can be considered as a combination of a linear and a curved nonlinear region. The parameters  $a$  and  $b$  account for the linear part which defines the straight line. Parameters  $t$  and  $c$  represent the curved part. Energy resolution (sigma of Gaussian fit) of the Timepix pixel detector is measured to be 3 keV at 60 keV.

$$TOT(E) = a.E + b + \frac{c}{E - t}. \quad (4.1)$$

## 4.5 Tracking capabilities of Timepix

Due to the pixelization of the Timepix detectors, the separate events registered by different pixels on same detector can be distinguished, thus spatial information is achieved along with energy information. Figure 4.11 gives an example of spatial information available from pixel detectors which helps to reduce the background significantly.

The 2D information from the pixels can effectively identify particle types, there by

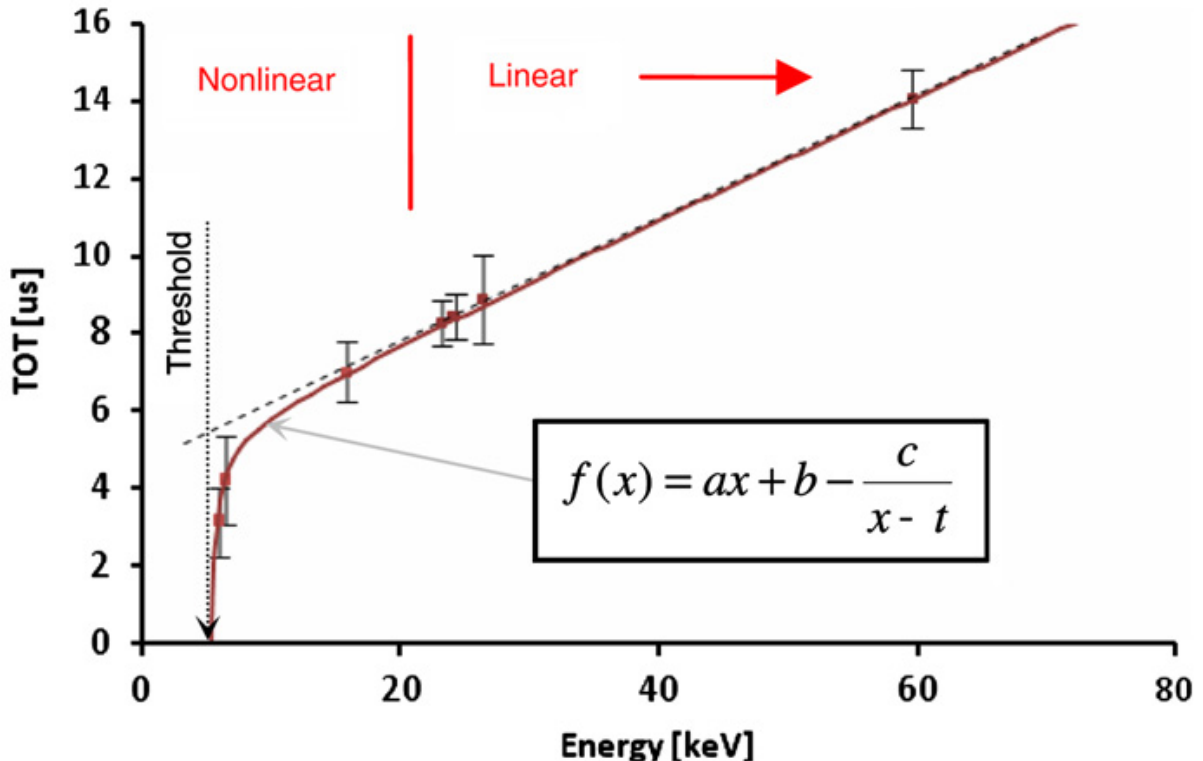


Figure 4.10: Illustration of Timepix pixel calibration curve [80] in TOT mode.

achieving significant signal to background improvements. Figures 4.12, 4.13 and 4.14 present different particle types (alpha, electron and Muon/MIP) detected by Timepix detector, which give a clear idea of the power of pixel detector in background reduction. All above events have comparable energy deposition but different track signature. In a non-pixelated detector these interactions are indistinguishable. The pixel detector response clearly gives more details of the particles. The alpha particle has round cluster shape with maximum energy deposition at the central pixels, the electron has curly tracks with end pixels collecting more charge as indicated by Bragg curve, while the muon/MIP interaction deposit energy in pixels according to Landau distribution [50]. Mathematical methods used in the identification of different particles detected by pixel detector are described in [81].

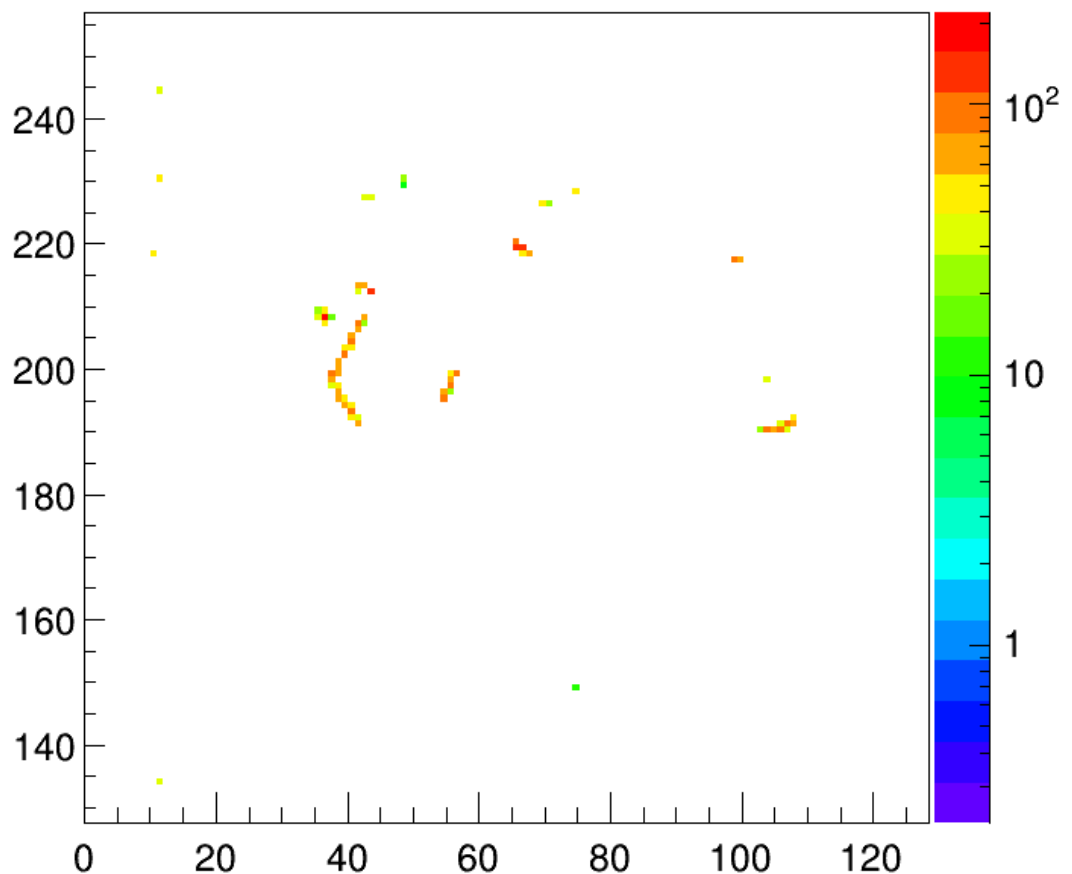


Figure 4.11: Registered events on Si pixel detector in 1 s time window. Pixel detectors can give spatial information along with energy of the events.

Pixel circuit	DAC name	Function	Type	Size (Bits)	Range
CSA	$I_{PreAmp}$	CSA gain, influence the amplitude of the pulse	I	8	0-2 $\mu A$
	$I_{KRUM}$	Discharge time of CSA output, compensates the leakage current	I	8	0-140 nA
	$V_{FBK}$	Sets baseline of CSA output	V	8	0-2.2 V
	$V_{CAS}$	Tunes the input capacitance of CSA	V	8	0-2.2 V
	$V_{GND}$	Sets input baseline voltage of CSA	V	8	0-2.2 V
Discriminator	$I_{DISC}$	Discriminator biasing	I	8	0-1.67 $\mu A$
	$I_{THS}$	Sets the basic unit of compensation current for pixel-wise threshold equalization	I	8	0-40 nA
	$I_{HYST}$	To remove glitches in Discriminator output	I	8	0-200 nA
	$V_{THL}$	Global pixel threshold setting	V	14	0-2.2 V
Analog Driver	$I_{BuffA}$	Bias for analog buffers	I	8	0-10.2 $\mu A$
	$I_{BuffB}$		I	8	0-391 $\mu A$
LVDS Driver	$I_{LVDS_{tx}}$	Bias for LVDS circuits	I	8	0-392 $\mu A$
	$V_{Ref\,LVDS_{tx}}$		V	8	0-817 mA

Table 4.1: List of Timepix DACs and description of their functions.

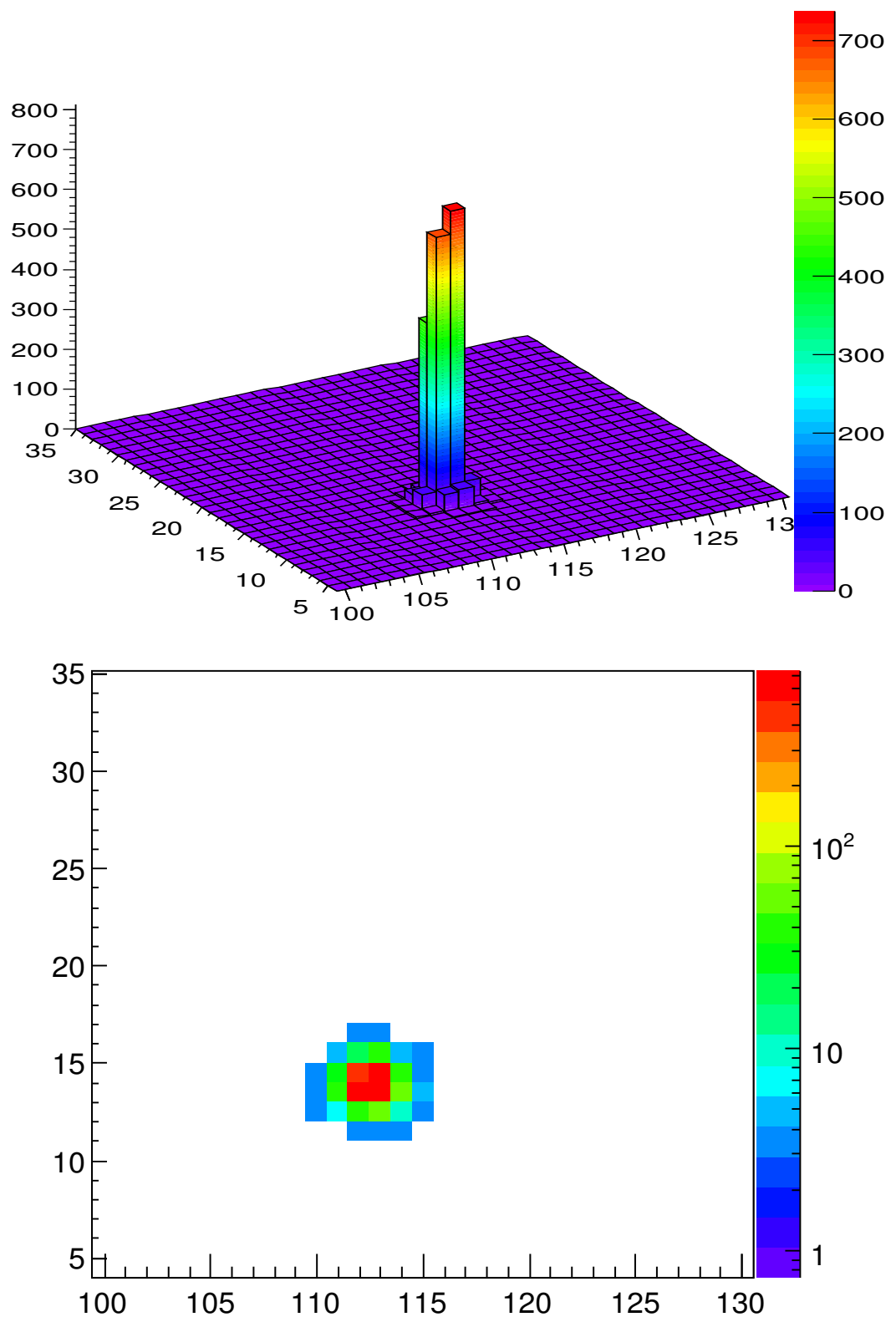


Figure 4.12: 2D track of alpha particle (2869 keV) generated in a  $55 \mu\text{m}$  pitch Si Timepix.

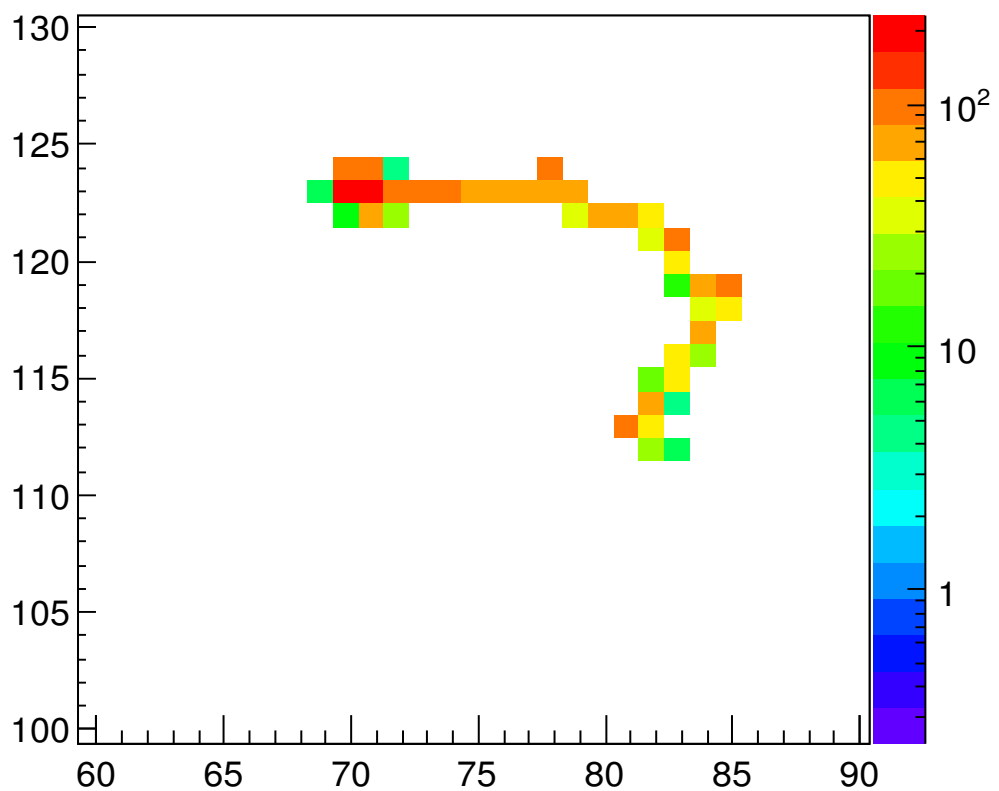
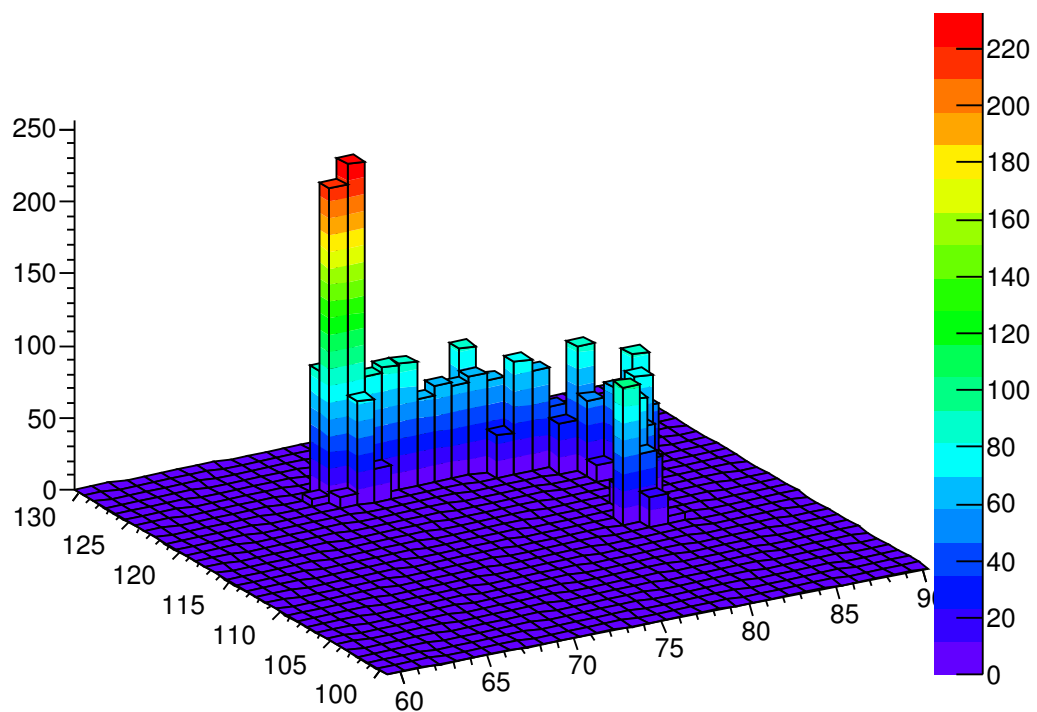


Figure 4.13: 2D track of electron (2524 keV) generated in a  $55\text{ }\mu\text{m}$  pitch Si Timepix.

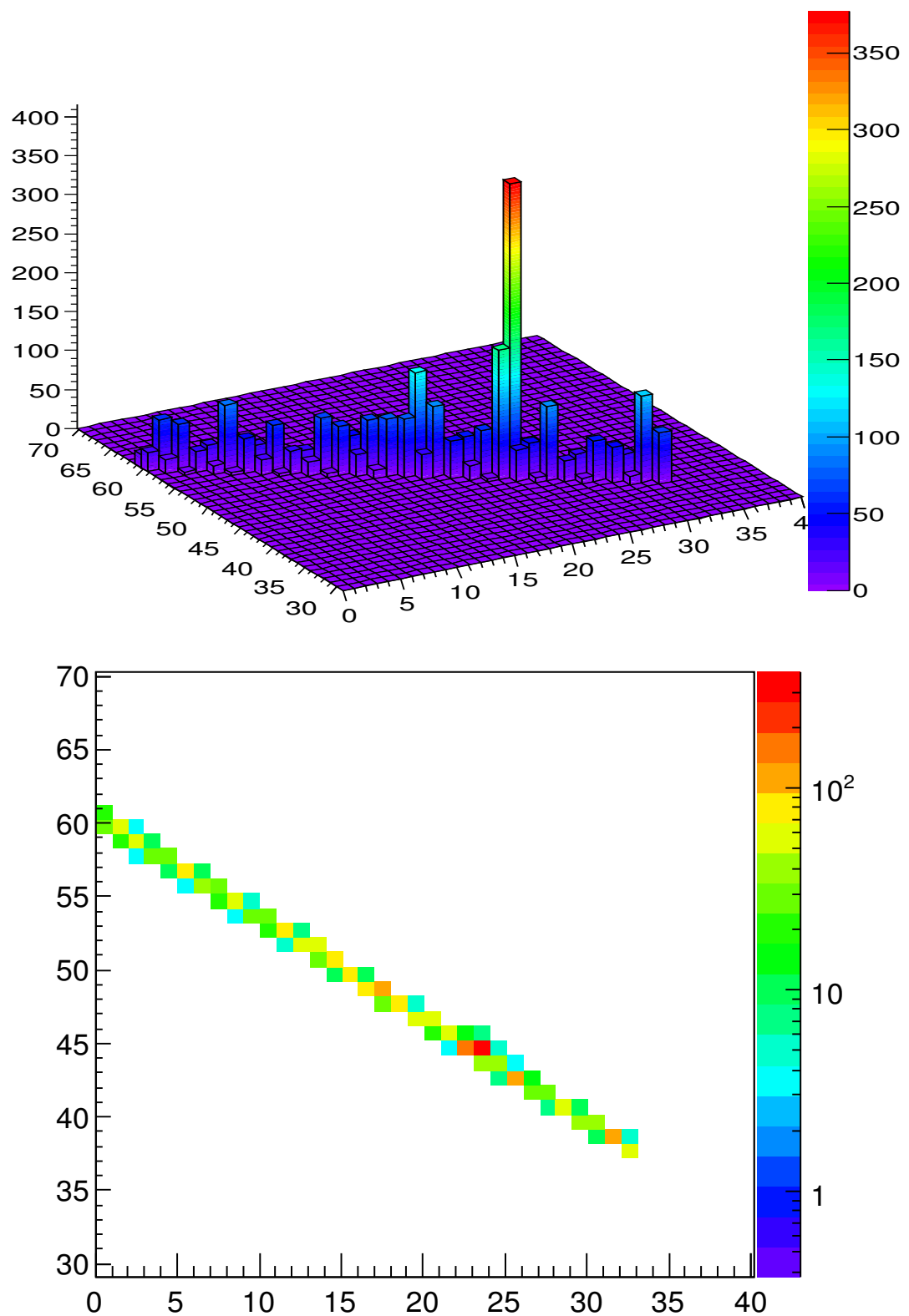


Figure 4.14: 2D track of Muon/MIP (2795 keV) generated in a 55  $\mu\text{m}$  pitch Si Timepix.

# Chapter 5

## Intrinsic background studies

The intrinsic contamination in the measurement setup is a big concern for low counting experiments. The unwanted radioactive contaminants in the construction materials pose big threat to double beta decay experiments. It is very important to properly understand the background contaminants in the fabrication materials for the setup and to choose the right ones with low contamination. In the case of pixel detectors significant amount of materials are present near the detection medium which can spoil the measurement (see Figure 5.1). Pixel detectors need a Printed Circuit Board (PCB) to make electrical connections and it also functions as a mechanical support and a cooling medium. Other materials to be considered are electronic components (such as capacitors), glue (to fix detectors on the PCB) and connectors (for interconnecting chip-carrier<sup>1</sup> boards to form detector stack) in the setup. All the constituent materials mentioned above were tested at the low background setup in the LSM underground laboratory. The detector used for the measurements was High Purity Germanium (HPGe) planar detector with an area of 150 cm<sup>2</sup> and the detection range was 20 keV - 1.5 MeV. Background tests for low radioactivities (especially using small amount of materials) are time consuming tasks. Therefore, very often results presented in this chapter are just limits for radioactive impurities, but which are acceptable for our needs.

As a first step, different parts of standard pixel detector setup such as Timepix ASIC, chip-carrier PCB and bump-bonding materials were measured for intrinsic background. The background rates of pixel detector parts are presented in Table 5.1. Bump-bonding material and readout ASIC (Timepix chip) were not contaminated by radioactive materials (measurements gave just limits), while it was observed that chip-carrier board (made of FR4 material) on which the Timepix detector is normally mounted had significant contribution to background (see Table 5.2) caused mainly by U/Th contamination.

### 5.1 PCB materials tests and selection

Because of the high contamination in standard PCB, it was decided to study more precisely sources of contamination and find out the best alternative material. Printed Circuit Board (PCB) is a combination of different layers of materials. Figure 5.2 shows the

---

<sup>1</sup>PCB board on which pixel detector is mounted and thus 'carrier' of the chip.

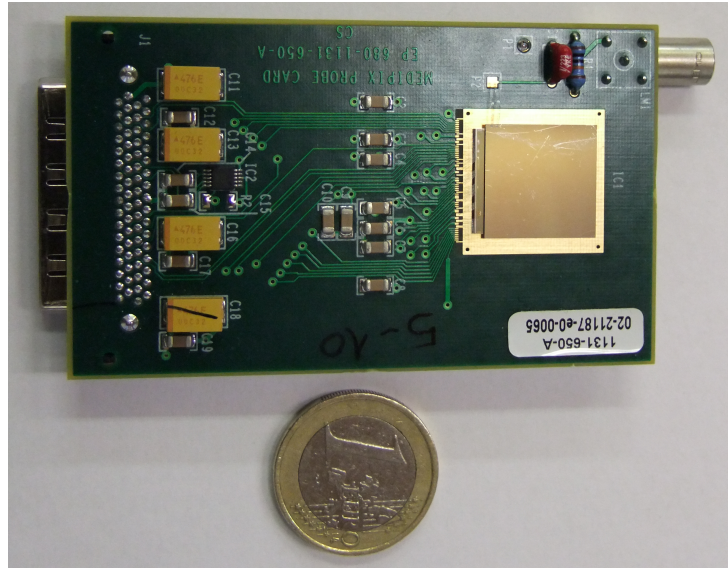


Figure 5.1: Timepix pixel detector mounted on FR4 chip-carrier PCB. The materials close to Si sensor can influence the intrinsic background level of the measurement system.

Material, mass of sample and time of measurement	Radionuclides (mBq/kg)				
	$^{228}\text{Th}$	$^{234}\text{Th}$	$^{40}\text{K}$	$^{60}\text{Co}$	$^{137}\text{Cs}$
Bump-bond material (In), 1.1 g, 601882 s	< 245	< 3642	< 3909	< 270	< 151
Bump-bond material (Sn), 0.725 g, 593200 s	< 471	< 4141	< 3593	< 413	< 350
Readout ASIC (Si), 0.398 g, 329770 s	< 428	< 2312	< 16000	< 1300	< 716

Table 5.1: Intrinsic background measurement results of Timepix readout ASIC and bump-bonding materials, measured at the low background setup in the LSM laboratory (HPGe planar detector,  $150 \text{ cm}^2$ , range 20 keV- 1.5 MeV).

Radioactive impurities in FR4 chip-carrier PCB (mBq/kg)					
$^{228}\text{Th}$	$^{234}\text{Th}$	$^{40}\text{K}$	$^{228}\text{Ra}$	$^{210}\text{Pb}$	$^{226}\text{Ra}$
$21308 \pm 648$	$13611 \pm 891$	$< 2025$	$17660 \pm 972$	$10693 \pm 1620$	$14177 \pm 486$

Table 5.2: Intrinsic background measurement result of FR4 chip-carrier PCB measured at the low background setup in the LSM laboratory (HPGe planar detector,  $150 \text{ cm}^2$ , range 20 keV- 1.5 MeV). Mass of sample was 12.343 g and time of measurement was 83466 s.

schematic view of two layer PCB. Mainly, it has the copper layer on which the electrical circuit is etched in and the dielectric material which hold the copper layer and act as the

Mass of sample, Time of measurement	Radioactive impurities in CuFlon (mBq/kg)						
	$^{226}\text{Ra}$	$^{210}\text{Pb}$	$^{228}\text{Ra}$	$^{228}\text{Th}$	$^{60}\text{Co}$	$^{137}\text{Cs}$	$^{40}\text{K}$
14.1 g , 684738 s	<15	<134	<39	<16	<20	<14	<280

Table 5.3: Intrinsic background measurement result of CuFlon PCB material. CuFlon is made of Teflon and copper.

insulation between copper layers. Chemical or mechanical etching is done for making the circuits in the copper layer. There are additional layers like 'silkscreen' (line-art and texts printed on the PCB) and 'solder mask' (surface layer protecting copper from oxidization). Additionally, glue is used for making multiple layer PCBs. The standard PCB commonly known as FR4 is made of glass-reinforced epoxy laminate sheets as dielectric. Multilayer PCB is formed by gluing additional copper sheets and insulation layers. In the case of flexible PCB the usual dielectric material is kapton tape [82].

Different available PCB materials such as CuFlon<sup>®</sup> (pure Teflon is the insulation layer) [83] and components of flexible PCB were collected and measured at the same low background setup. Table 5.3 lists the intrinsic contamination of CuFlon PCB material. It can be seen that the CuFlon material is very clean in terms of radioactive impurities. The Table 5.4 compares the detected activities in two flexible PCB materials: VonRoll Laminem KT50/A1 and Dupot Pyralux FR 9151. VonRoll Laminem KT50/A1 is single side copper on Kapton with other side having a glue layer, whereas Dupot Pyralux FR 9151 is double side copper on kapton. Both materials were found to be far better than FR4 material. Table 5.5 is measurement result of adhesive and solder mask used in the flexible PCB technology. Flexible PCB materials are relatively light-weight and found to be very clean. The measurement results validate the use of CuFlon and flexible PCB for the final setup.

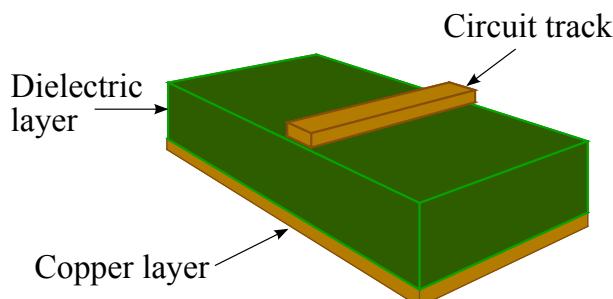


Figure 5.2: Schematic view of two layer PCB. Two layers of copper separated by an insulating layer.

## 5.2 Test of components

The components used very near to the Timepix detectors are decoupling capacitors (Figures 5.3a and 5.3b), connectors for forming the stack (Figure 5.3c) and glue for fixing the detectors to PCB (Figure 5.3d). These components could influence the level of back-

Radionuclide	Activity (mBq/kg)	
	VonRoll Laminem KT50/A1	Dupot Pyralux FR 9151
<sup>226</sup> Ra	207±76	<50
<sup>210</sup> Pb	<3200	<1250
<sup>228</sup> Ra	<215	<125
<sup>228</sup> Th	170±76	<125
<sup>60</sup> Co	<290	<100 6
<sup>137</sup> Cs	<132	<46
<sup>40</sup> K	<1760	<1020

Table 5.4: Results of measurements of radioactive impurities in selected flexible PCB materials. VonRoll Laminem KT50/A1 is single side copper and Kapton with glue. Dupot Pyralux FR 9151 is double side copper on kapton.

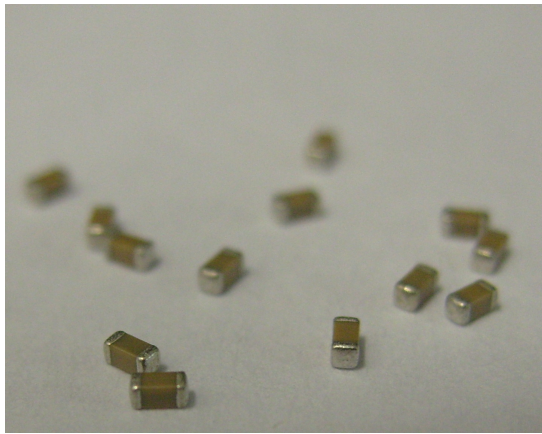
Radionuclide	Activity (mBq/kg)	
	Adhesive	Coverlay FR 0210
<sup>226</sup> Ra	<556	<1500
<sup>210</sup> Pb	<16000	<40000
<sup>228</sup> Ra	<1400	<3500
<sup>228</sup> Th	<1400	<3500
<sup>60</sup> Co	<700	<3000
<sup>137</sup> Cs	<400	<1800
<sup>40</sup> K	<9000	<28000

Table 5.5: Results of radioactive impurities measurements for adhesive and solder mask (Coverlay FR 0210) used in flexible PCBs. Adhesive is used to glue more layers of flexible PCB layers. Solder mask is a layer covering the surface of PCB to protect copper from oxidation and other damages.

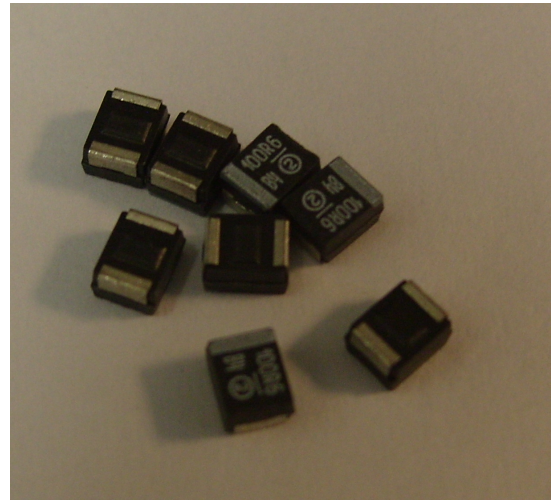
ground significantly. These items were also measured to determine the background rates and obtained results of radiopurity levels are shown in Tables 5.6 (ceramic capacitors), 5.7 (tantalum capacitors), 5.8 (connectors) and 5.9 (glue). The levels of impurities are high in the stacking connectors and ceramic capacitors. Based on the obtained results, special attention has to be paid on the location of capacitors and connectors on the board. Later it was found that the ceramic capacitors (with had high background rates) were not cleaned in the ultrasonic bath before measurement. It is a procedure to clean the sample before the measurements to remove any surface contamination. Based on this experience, after soldering the components boards are thoroughly cleaned in the ultrasonic cleaner using isopropyl alcohol. This step could help to remove the surface contamination as much as possible.

### 5.3 Test of finished PCBs

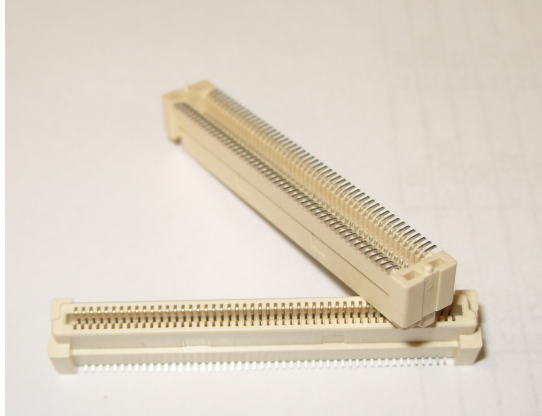
Based on the results of the intrinsic background study, CuFlon and flex-rigid PCB using CuFlon were finalized for the production of the detector setups. Boards produced from



(a) Ceramic capacitor.



(b) Tantalum capacitor.



(c) Connectors.



(d) Glue.

Figure 5.3: Components, connectors and glue used in the pixel telescope. These items were measured for intrinsic contamination.

these selected materials were again tested in the same HPGe measurement setup. The aim was to check the fabrication procedure from the point of view of additional radioactive impurities. Three sets of measurements were performed: using plain CuFlon PCB, CuFlon PCB with components soldered to it (see Figure 5.4a) and plain flex-rigid PCB (see Figure 5.4b). The results of these measurements (limits) are presented in Table 5.10. It can be seen that production procedure and soldering did not add significant impurities to the board.

Ceramic Capacitors		
Mass of sample = 0.48 g		
Time of measurement = 233570 s		
Radionuclide	Activity (mBq/kg)	Activity (mBq/unit)
$^{226}\text{Ra}$	$27216 \pm 5538$	$0.19 \pm 0.04$
$^{210}\text{Pb}$	<32900	<0.23
$^{228}\text{Ra}$	<1659	<0.01
$^{228}\text{Th}$	$3363 \pm 773$	$0.024 \pm 0.005$
$^{60}\text{Co}$	<1500	<0.01
$^{137}\text{Cs}$	<833	<0.006
$^{40}\text{K}$	<13343	<0.09

Table 5.6: Intrinsic background measurement results of ceramic capacitor. Results are shown in both mBq/kg and mBq/unit where a unit is a single capacitor.

Tantalum Capacitors		
Mass of sample = 0.57 g		
Time of measurement = 495160 s		
Radionuclide	Activity (mBq/kg)	Activity (mBq/unit)
$^{226}\text{Ra}$	<1283	<0.09
$^{210}\text{Pb}$	<65485	<5
$^{228}\text{Ra}$	<839	<0.06
$^{228}\text{Th}$	<419	<0.03
$^{60}\text{Co}$	<700	<0.05
$^{137}\text{Cs}$	<420	<0.03
$^{40}\text{K}$	<6480	<0.46

Table 5.7: Intrinsic background measurement results of Tantalum capacitor. Results are shown in both mBq/kg and mBq/unit, where a unit is a single capacitor.

Stacking connectors	
Radionuclide	Activity (mBq/kg)
$^{210}\text{Pb}$	$4.03 \pm 1.44$
$^{238}\text{U}$	$3.97 \pm 1.53$
$^{226}\text{Ra}$	$< 6.70 \times 10^{-1}$
$^{228}\text{Th}$	$2.72 \pm 2.48 \times 10^{-1}$
$^{235}\text{U}$	$1.89 \times 10^{-1} \pm 7.30 \times 10^{-2}$
$^{228}\text{Ra}$	$< 6.33 \times 10^{-1}$
$^{137}\text{Cs}$	$< 7.86 \times 10^{-1}$
$^{227}\text{Ac}$	$170.29 \pm 10.31$

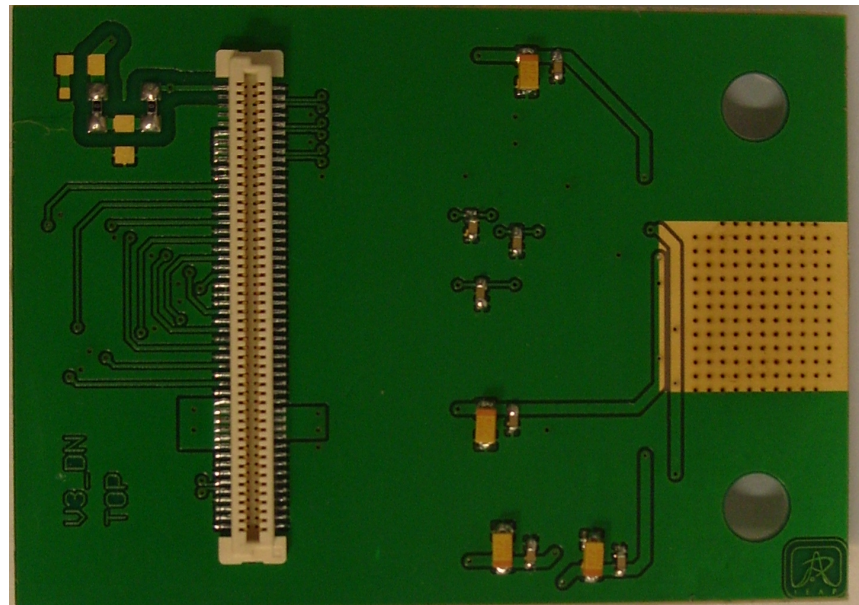
Table 5.8: Intrinsic background measurement results of connector.

Material	Radionuclides (mBq/kg)					
	$^{210}\text{Pb}$	$^{238}\text{U}$	$^{226}\text{Ra}$	$^{228}\text{Th}$	$^{228}\text{Ra}$	$^{137}\text{Cs}$
Glue	$< 222$	$< 174$	$< 104$	$< 131$	$< 111$	$< 57$

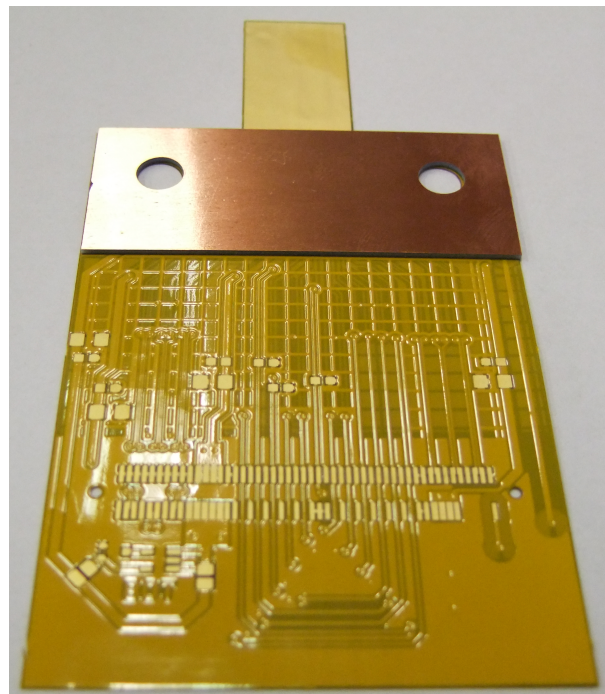
Table 5.9: Intrinsic background measurement results of glue.

Board type	Radionuclides (mBq/kg)					
	$^{210}\text{Pb}$	$^{238}\text{U}$	$^{226}\text{Ra}$	$^{228}\text{Th}$	$^{228}\text{Ra}$	$^{137}\text{Cs}$
CuFlon	$< 222$	$< 154$	$< 75$	$< 38$	$< 155$	$< 57$
CuFlon soldered	$< 222$	$< 174$	$< 104$	$< 131$	$< 111$	$< 57$
Flex-rigid	$< 434$	$< 181$	$< 670$	$< 31$	$< 155$	$< 88$

Table 5.10: Intrinsic background measurement results of finished Pixel Telescope PCBs.



(a) Soldered CuFlon PCB.



(b) plain Flex-rigid PCB.

Figure 5.4: Finished Pixel Telescope PCBs used in the measurements for intrinsic contamination.

# Chapter 6

## Hardware developments

The nature of the double beta decay experiments demand very stringent conditions on hardware developments. The amount of materials near to detector volume should be kept as low as possible and the background produced from these materials should be reduced, which make the material selection difficult. Pixel detectors are composition of sensor and pixelated readout ASIC. Usually pixel detectors are mounted on a chip-carrier PCB (Printed Circuit Board) and the electrical connections between ASIC and PCB are made by wire-bonding. The Figure 6.1 shows the CERN chip-carrier board using FR4 PCB, which is a standard widely used with Timepix. FR4 is a commonly used substrate in PCB manufacturing.

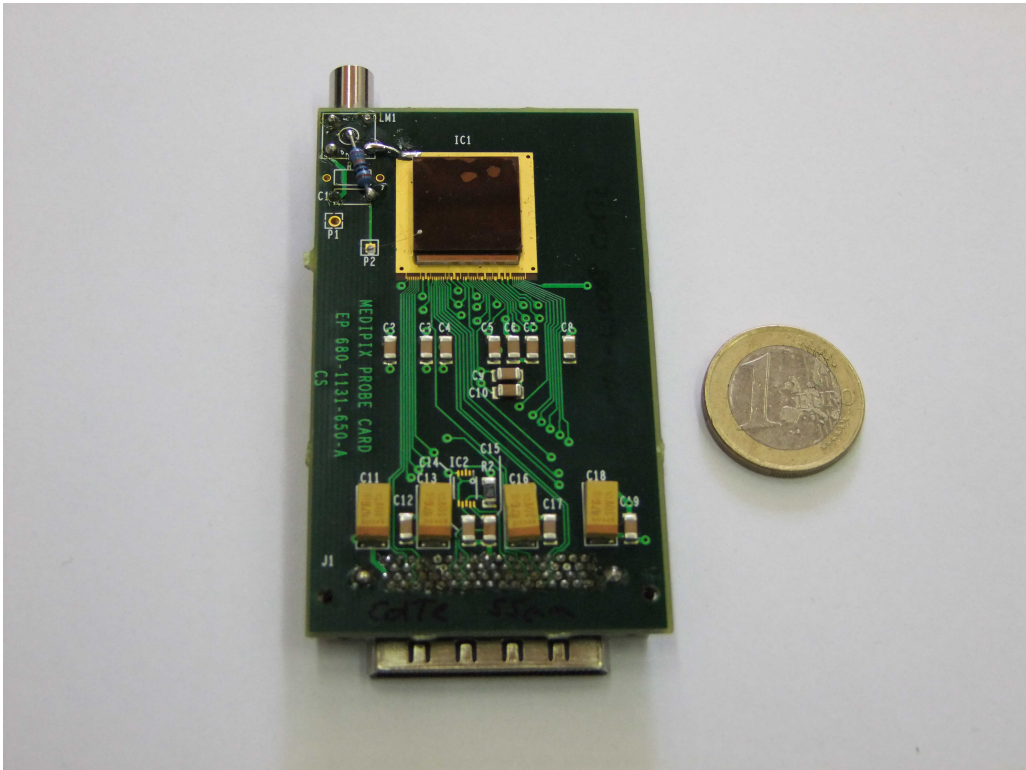


Figure 6.1: CERN chip-carrier board with Timepix detector (using CdTe sensor). The PCB is produced from FR4 material.

Intrinsic background of the PCB material is very crucial in the construction of pixel setup. The PCB is very close to the pixel detector and that is the reason it was optimized for radiopurity. The FR4 material has significant amount of radioisotopes and it is undesirable for double beta setup (see discussions in section 5.1). Different PCB materials were collected and tested to find the best choice for the setup. CuFlon [83] and flexible PCB were found to be the best choice with significantly less contamination. Details of the measurements and obtained results were presented in chapter 5. Pixel detector hardware must be fabricated using these materials. For the purpose of double beta experiments (TGV and COBRA) several geometries were also tested. The stacking geometry was found to have advantage of keeping the detectors very close and aligned, thus improving the detection efficiency. A number of modifications and improvements were done on chip-carrier PCB. A detailed description of all the hardware developments is presented in this chapter.

Both experiments (SPT and COBRA) need coincidence measurements with detectors to increase the efficiency and to improve the S/B ratio. To form the best geometry, detectors should be aligned vertically with sensors facing each other. Also the detectors should be able to connect in a daisy-chain to the FITPix readout. The pixel telescope design is the first step towards this goal (see Figure 6.2). The pixel telescope unit is comprised of motherboard and chip-carrier PCBs. Chip-carrier PCB carry the pixel detector and a pair of chip-carrier boards constitute a detection unit. The bottom chip-carrier board contains the detector facing up and the top chip-carrier board contains the detector facing down. Detectors in this pair are thus arranged in a "face-to-face" geometry and aligned each other vertically. Two detectors are connected in a daisy-chain and are attached to a motherboard. Motherboard interconnects the detection unit to FITPix readout. All detectors in the daisy-chain are triggered in coincidence. All electrical connections (bias voltage, control signals, data lines) are made to each Timepix detector through 100 pin stacking connectors. Chip-carrier PCBs are firmly positioned using Delrin (radiopure material) screws and nuts.

## 6.1 CuFlon Pixel Telescope

CuFlon is relatively new material (pure Teflon and copper) and processing of this material is still not easy. The adhesion between Teflon and copper is very weak. The wire-bonding pads require very dense and narrow design. CuFlon PCB has some limitations for high dense routing and pads. A prototype of Pixel Telescope using CuFlon PCB material was designed and fabricated as the first step. Figure 6.2 shows the schematic of CuFlon Pixel Telescope. Figure 6.3a shows the single chip-carrier board of CuFlon Pixel Telescope with sensor. In Figure 6.3b a unit of CuFlon Pixel Telescope with CdTe sensor of 2 mm thickness is shown. Figure 6.3c shows a unit of CuFlon Si Pixel Telescope. In the Figure 6.3d a close-up view of pair of detectors in the CuFlon Si Pixel Telescope is given. In the CuFlon Pixel Telescope prototypes the distance between the chip-carrier boards is fixed (5 mm).

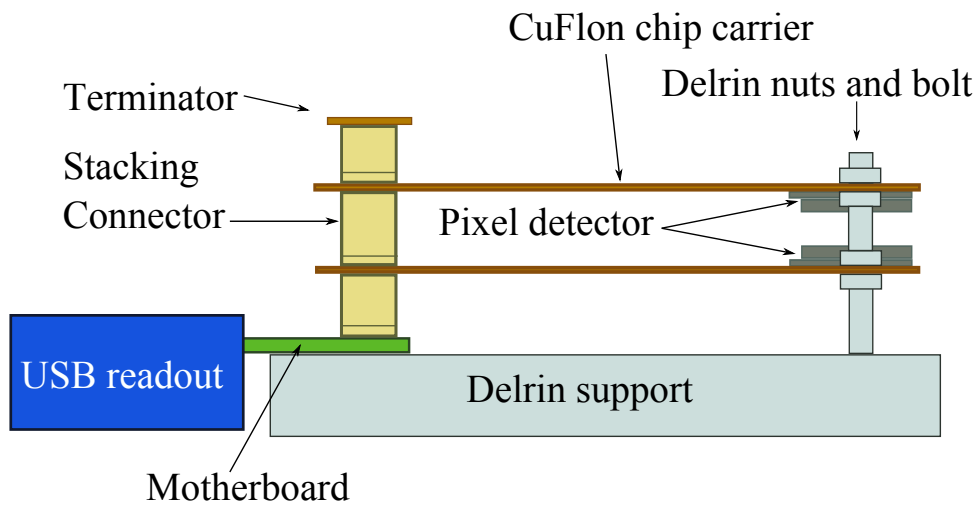
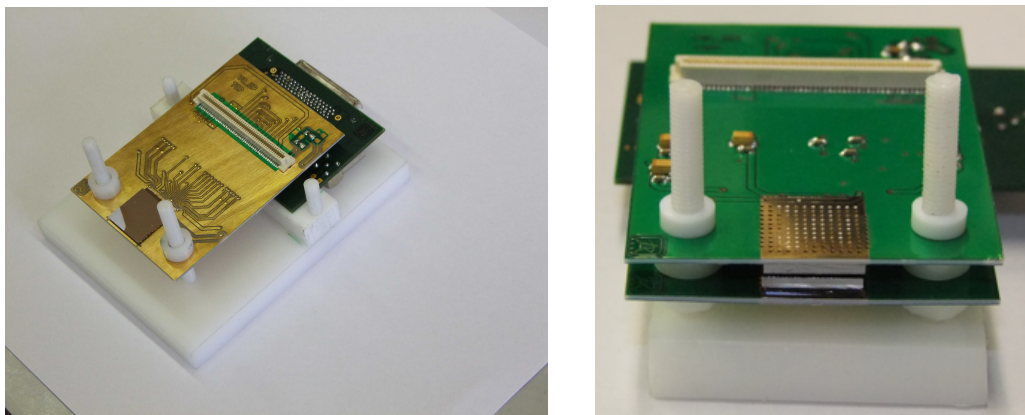
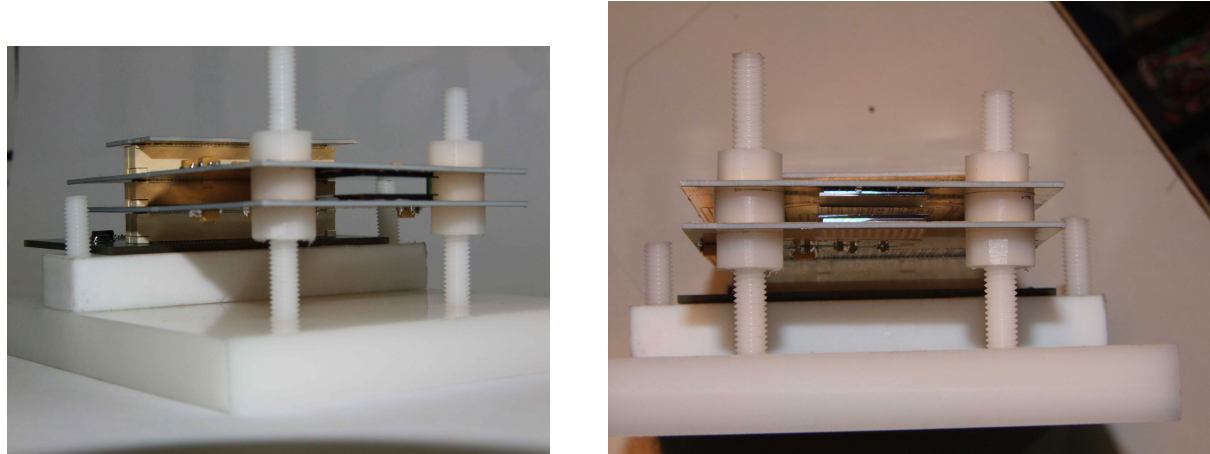


Figure 6.2: Schematic illustration of CuFlon Pixel Telescope.



(a) CuFlon chip-carrier PCB.

(b) CdTe pixel telescope produced using 2 mm thick sensors.



(c) CuFlon pixel telescope unit.

(d) CuFlon pixel telescope unit front view.

Figure 6.3: CuFlon Pixel Telescope.

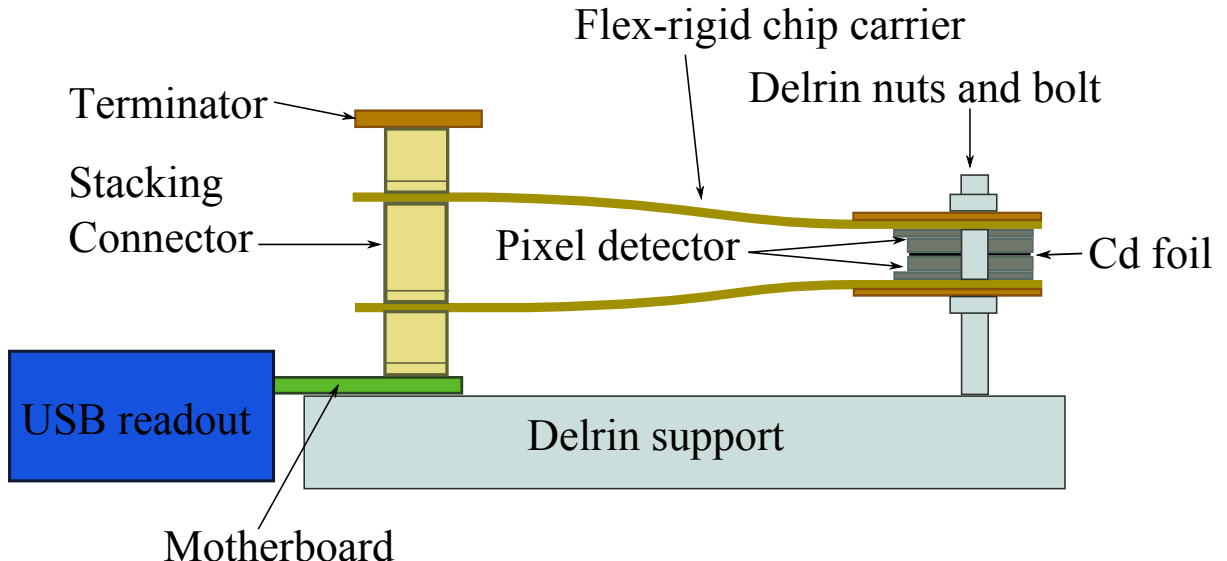
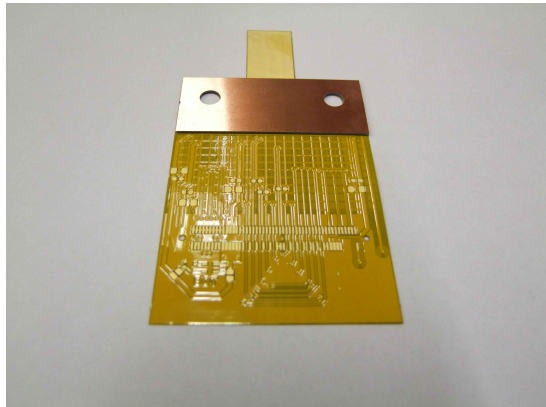


Figure 6.4: Schematic illustration of Flex-Rigid Pixel Telescope.

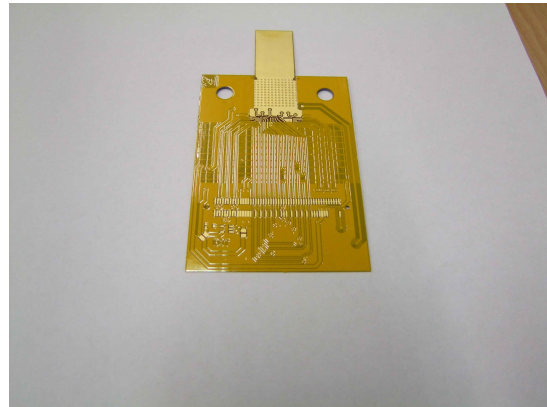
## 6.2 Flex-Rigid Pixel Telescope

For Si Pixel Telescope experiment (detection of  $2\nu$ EC/EC decay of  $^{106}\text{Cd}$  using silicon pixel detectors), the detection efficiency is increased when the distance between the pixel detectors in the pair are decreased (see discussions in the section 3.2). In order to achieve this close geometry, where detectors are almost touching each other, a flex-rigid PCB design is followed. Figure 6.4 illustrates the details of this design. The important fact is that flexible PCB materials also has very low background (see section 5.1). In this design the detector is mounted on a flex-rigid PCB with CuFlon board forming the rigid support below the detectors. This construction helps to adjust the distance between the detectors according to the needs, with the help of Delrin screws. Figures 6.5a and 6.5b show the CuFlon support side and detector mounting side of the flex-rigid chip-carrier PCB, respectively. Figure 6.5c shows the detector facing up with natural Cd foil on the surface. Figure 6.5d shows the complete Flex-Rigid Si Pixel Telescope unit. Figures 6.5e and 6.5f show the close-up view of the detector-Cd foil pair.

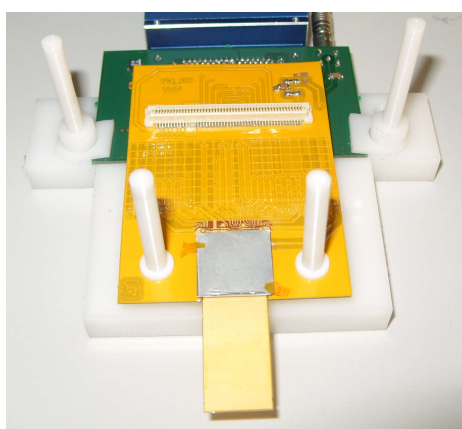
Another four units of Flex-Rigid Si Pixel Telescopes were already fabricated (Si sensor thicknesses 0.5 and 1 mm) and are being prepared for long-term underground background measurements (see Figure 6.6). In order to mount the detector vertically, a support structure using Delrin material was also designed. Delrin material was used because it is very clean from the point of view of radioactive impurities. Also, Delrin support was designed with the option to add additional shielding layer in between the detectors and readout units to reduce the background radiation originating from readout units (see Figure 6.7).



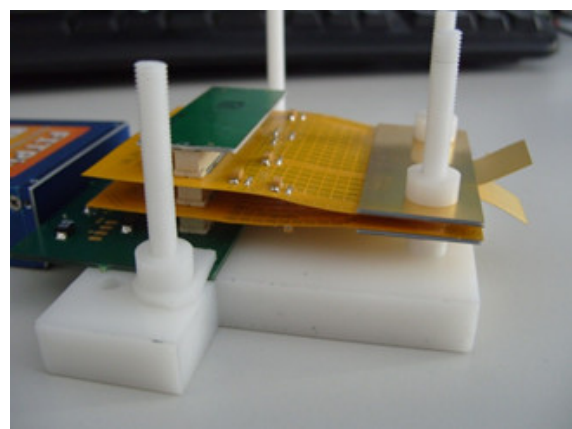
(a) CuFlon support side.



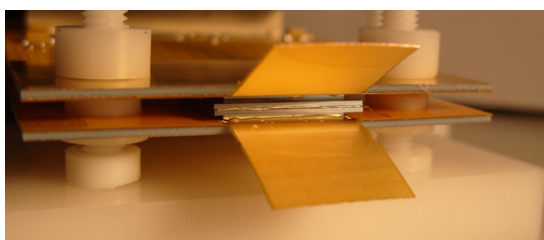
(b) Detector mounting side.



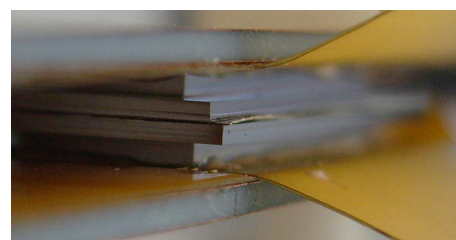
(c) CuFlon chip-carrier PCB.



(d) Flex-rigid pixel telescope unit.



(e) close-up view of Flex-Rigid Telescope unit with natural Cd foil.



(f) close-up view of Flex-Rigid Telescope unit with natural Cd foil.

Figure 6.5: CuFlon Silicon Pixel Telescope.

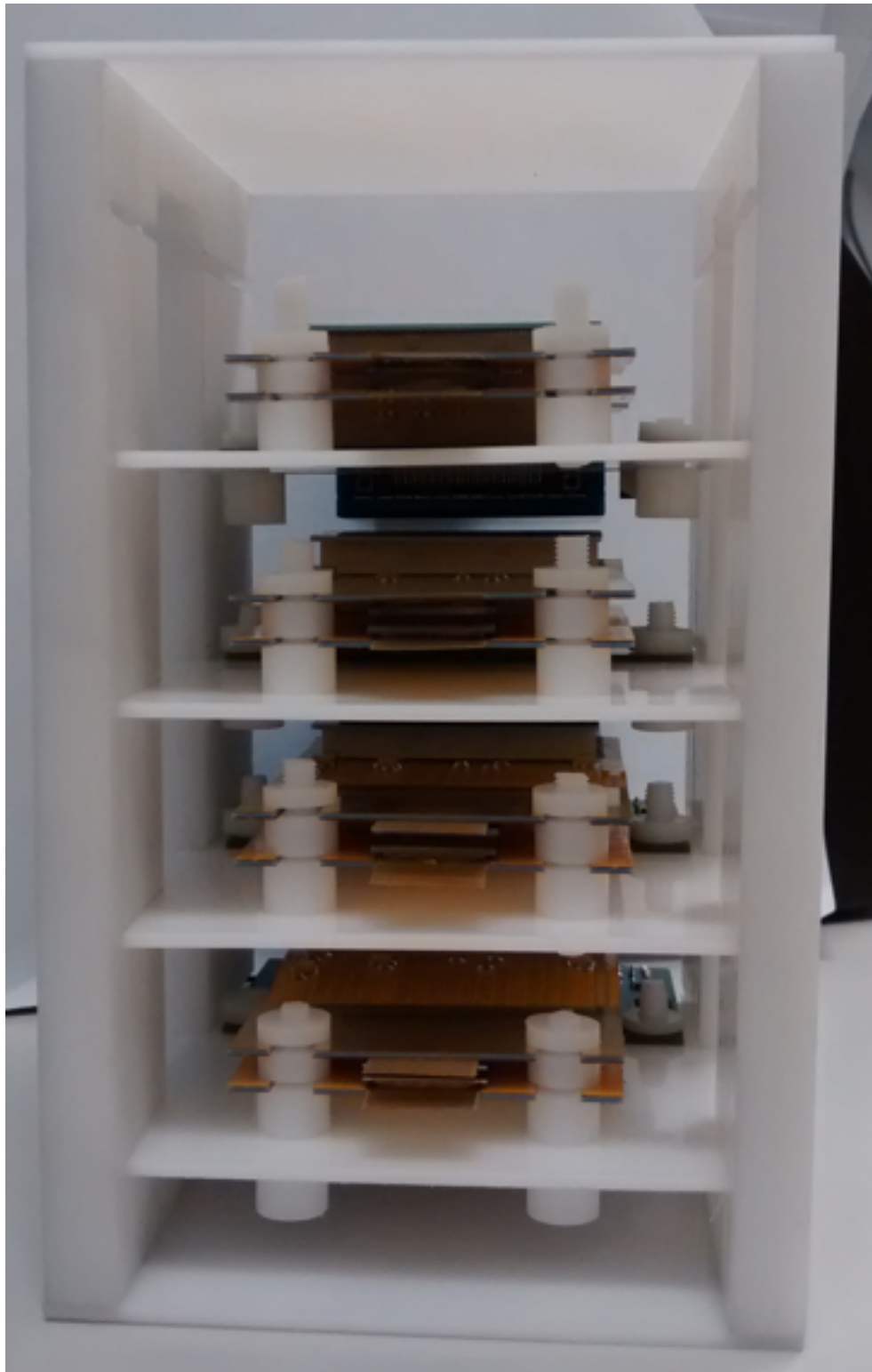


Figure 6.6: Newly produced Flex-Rigid Si Pixel Telescope units mounted in the Delrin support structure. Two units were made using 0.5 mm Si sensors and other two units were made using 1 mm Si sensors.

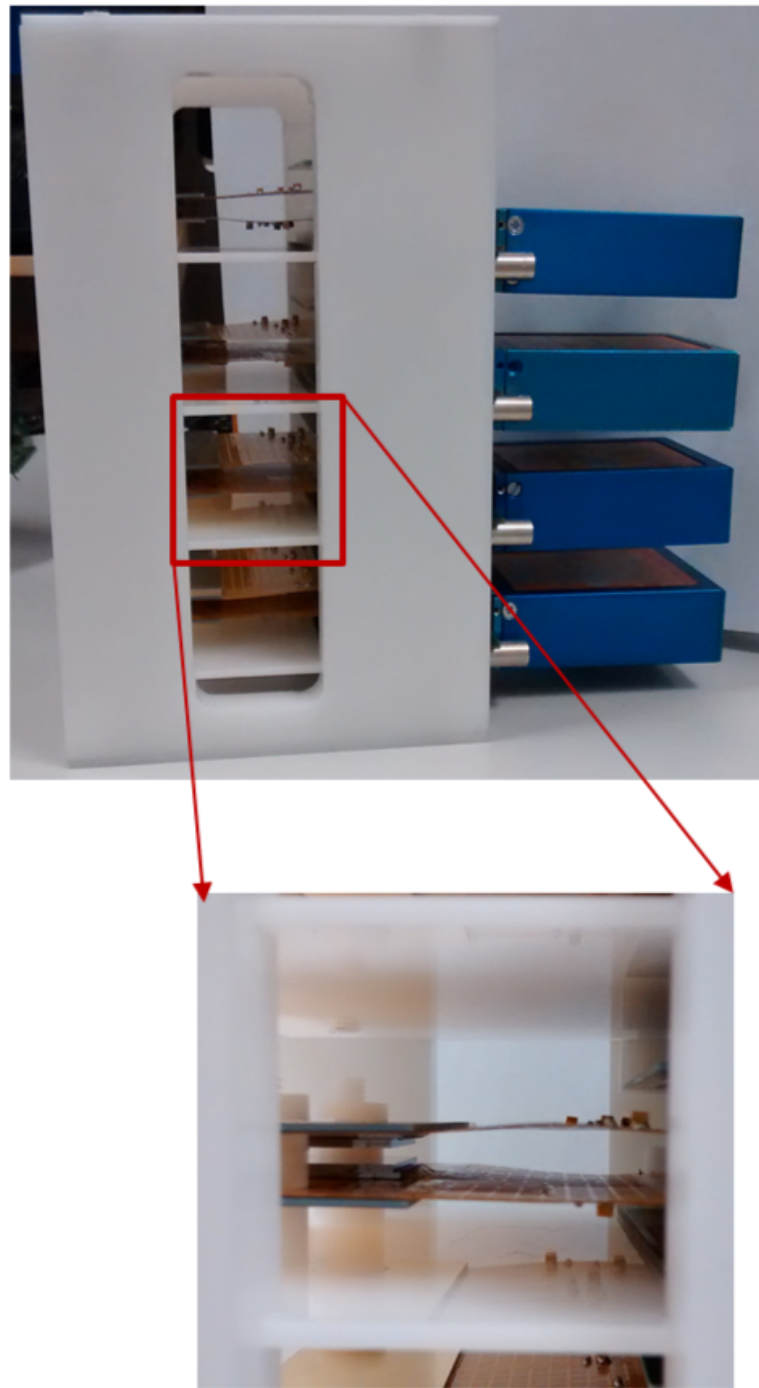


Figure 6.7: Side view of the Delrin structure. The opening to insert additional layer of shielding between the detectors and the readout units is highlighted.

# Chapter 7

## COBRA background measurements

As previously explained (in section 3.3), the COBRA collaboration plans to use CdZnTe for  $0\nu\beta^-\beta^-$  detection and the signature of this process is the double electrons generated from single point with the sum energy of 2.8 MeV from  $^{116}\text{Cd}$ . To understand the potential of pixel detectors for COBRA experiment, the background events detected in the Timepix pixel detectors were studied. A ‘Single Pixel Detector’ (SPD) with CdTe sensor was used for the background studies. The detector had a pixel pitch of 110  $\mu\text{m}$  and the CdTe sensor had a thickness of 1 mm. Figure 7.1 shows the SPD unit which was used in the measurements. Different sets of measurements were performed on the surface laboratory (at IEAP, CTU in Prague) and in the underground laboratory (LNGS, Gran Sasso, Italy). Results obtained from these measurements are presented in this chapter.

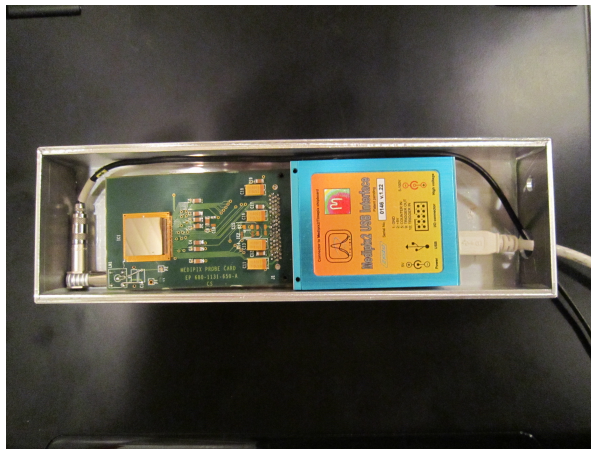


Figure 7.1: Timepix CdTe SPD (Single Pixel Detector) inside aluminium (Al) box, which was used in the background studies. Al box was used as a mechanical protection and also as a chamber to flush vaporised liquid Nitrogen ( $\text{N}_2$ ) to suppress the Radon.

Timepix pixel detectors can give tracks of particle interaction along with energy information. As mentioned in the section 4.4, the 2D signature of the events can be used to identify type of interaction by looking at the particle tracks based on the criteria such as cluster size, linearity, tortuosity, roundness and circularity of the clusters [5, 84, 81]. All these characteristics of clusters and cluster identification methods are described in detail in [81]. Pixelman [72] and Pixa [81] software tools were used to identify different types of particle interactions registered in the Timepix detector.

A cluster is a group of adjacent pixels from a single event. The cluster size (number of pixels) is very simple but crucial classification criteria to identify the particles. Generally, cluster size increases with the deposited energy and depends on type of incident particle. Usually alpha particles and electrons have higher number of pixels (cluster size proportional to energy) in their clusters, while gammas generate small clusters. High energy gammas scatter in the detector medium and may produce secondary particles such as electron, gamma or X-ray. Majority of such secondary events escape the scattered detector. It is very hard to judge such events as a single event, even if they were deposited in same detector.

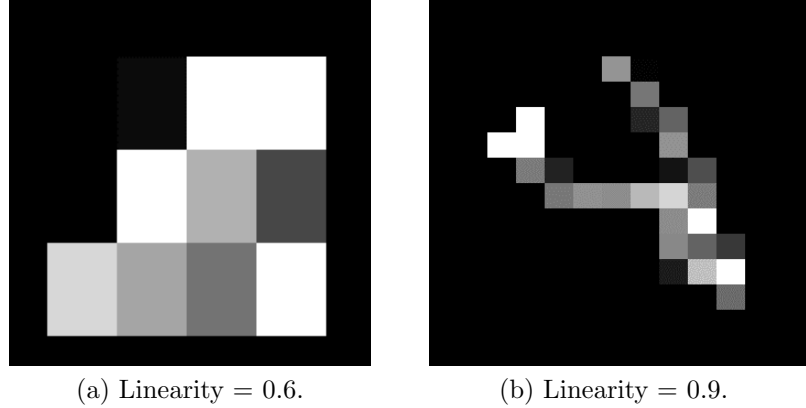


Figure 7.2: Examples of clusters with different linearities [81].

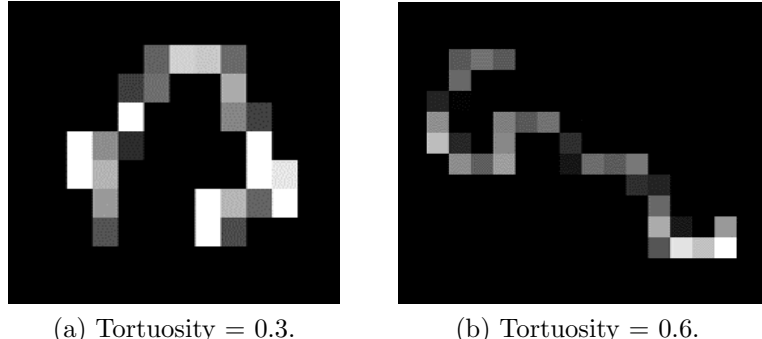


Figure 7.3: Examples of clusters with different tortuosity [81].

Linearity is a property which accounts for straightness of the cluster structure [81]. This property ranges from 0 to 1, where one corresponds to very straight cluster. For example, alphas have linearity close to zero while muon's linearity approaches one. Figure 7.2 compares two tracks with linearities 0.6 (7.2a) and 0.9 (7.2b). Tortuosity is another property which defines the curliness of the tracks and ranges from 0 to 1 [85]. For electron tracks the tortuosity is near to one, as they generate curly track in the detectors. As an example Figures 7.3a and 7.3b presents two tracks with tortuosities 0.3 and 0.6, respectively.

Roundness and circularity are the properties defining how round the shape of the clusters is. Roundness is the ratio between the inscribed and the circumscribed circles, and ranges from 0 to 1, with circle shape reaching one [81]. Figure 7.4a is a cluster with roundness 0.5 whereas 7.4b has roundness 0.8. Circularity is similar to roundness but it is ratio of the cluster area to area of circumscribed circle of cluster in pixels [81]. Circularity is again normalized to unity, ranges from 0 to 1. Figure 7.5a is a cluster with circularity 0.1 whereas 7.5b has circularity 0.6. An ideal alpha particle shape has circularity and roundness close to one.

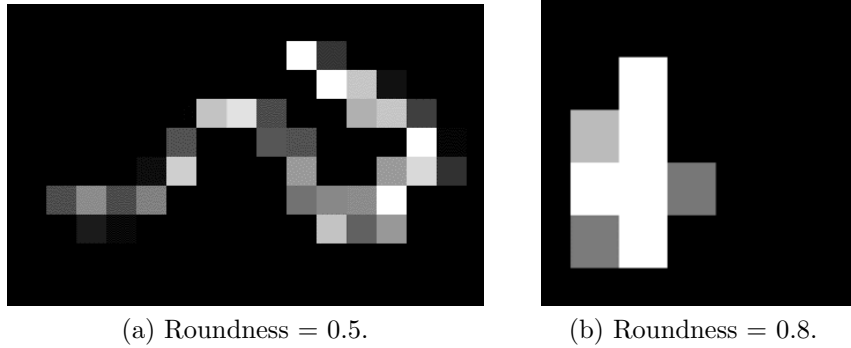


Figure 7.4: Examples of clusters with different roundness [81].

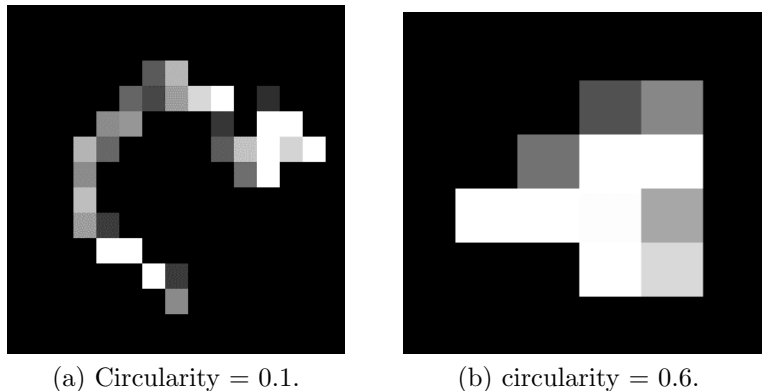


Figure 7.5: Examples of clusters with different circularities [81].

Alpha particle interactions generally create round clusters, while electrons generate curly tracks. To identify alpha particles, the criteria used were minimum cluster size 20, roundness 0.6 - 1 and circularity 0.6 - 1. For electrons identification, criteria were minimum cluster size of 10, maximum roundness 0.6, tortuosity 0.01 - 1, linearity 0.04 - 1 and maximum circularity 0.6. Alpha particles can be identified with high efficiency of recognition and thus background events due to them can be removed with high precision, while electrons are more difficult to identify. Gammas are identified mainly by their small cluster sizes. Due to their small cluster sizes, other cluster properties are less prominent and have less influence on identification.

## 7.1 Surface measurements

Measurements on the surface were performed at IEAP laboratory with 5 cm Pb shielding from all sides. Figure 7.6 shows the shielding used in the surface measurements. Results presented here are from a background run for the duration of 13.5 days. Figure 7.7 shows the full spectrum from the surface measurements and it includes contributions from different particle types (gamma rays, electrons, alphas, muons, etc.). The alpha peaks from Rn progenies are visible in the spectrum around 6 MeV (from  $^{218}\text{Po}$ ) and 7.69 MeV (from  $^{214}\text{Po}$ ). The rates of all events was 11818.46 per hour.



Figure 7.6: Lead shielding (5 cm thickness) used in the surface measurements.

Figure 7.8 shows the energy spectrum of alpha cluster identified using before mentioned conditions. The total number of alpha events identified was 5135 and thus the rate per hour was 15.85. The 6 MeV and 7.69 MeV peaks from Radon progenies are clearly identified by the classification algorithm (minimum cluster size 20, roundness 0.6 - 1 and circularity 0.6 - 1). Figure 7.9 shows the electron spectrum from the surface measurements which were classified using criteria given in previous section (minimum cluster size 10, maximum roundness 0.6, maximum circularity 0.6, tortuosity 0.01 - 1 and linearity 0.04 - 1). The electron events rate was observed to be 23.11 per hour. The spectrum of small clusters (of sizes up to 10 pixels) is shown in Figure 7.10. The observed rate of such events was 11621.09 per hour. These events are mostly from X-rays and gamma interactions and may also include low energy electrons and alphas. Detailed classification of events with small cluster sizes is a challenge, because the 2D signature is not so prominent. In Figure 7.11 the spectrum of alpha, electron and small cluster events are plotted along with the full spectrum. The full spectrum can be visualized as a combination of other spectra. It can be noticed that the lower energy part ( $< 1000$  keV) of the spectrum corresponds well with small cluster spectrum.

As it was pointed out earlier, the  $0\nu\beta^-\beta^-$  signal in  $^{116}\text{Cd}$  is in the energy region 2.5 - 3 MeV (region of interest). Thus more detailed analysis of background in this region was done. Figure 7.12 shows the spatial distribution of alphas in the region of interest

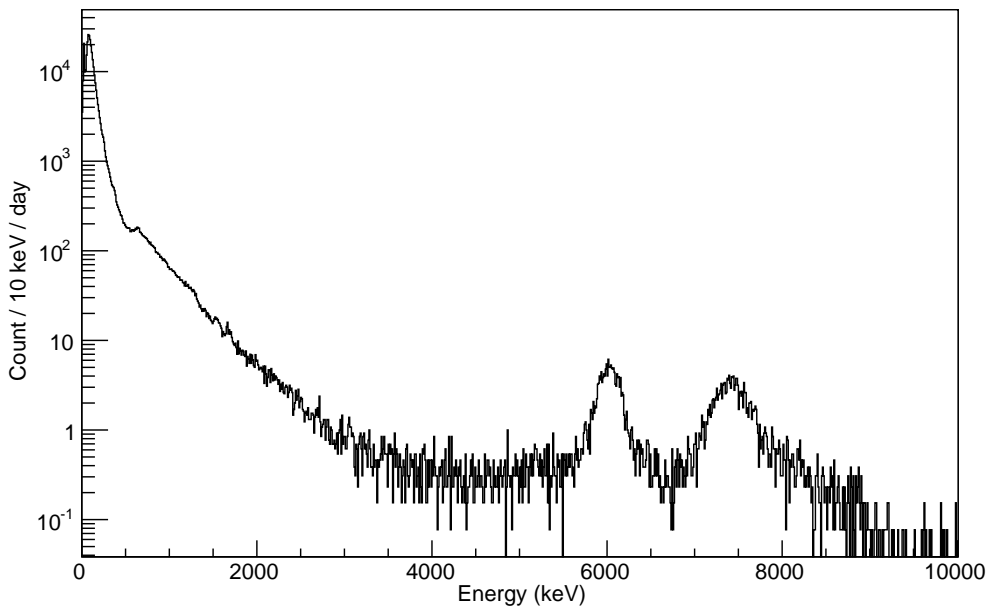


Figure 7.7: Full spectrum of surface measurement using CdTe SPD. Duration of measurement was 13.5 days and observed rate of all background events was 11818.46 per hour.

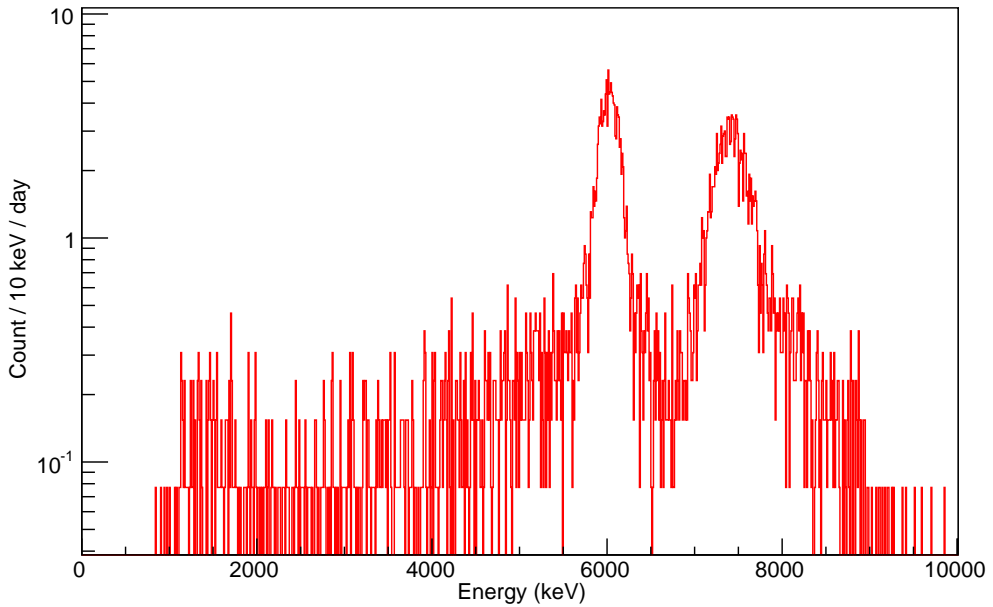


Figure 7.8: Alpha spectrum from surface measurement using CdTe SPD. Duration of measurement was 13.5 days and observed rate of alpha events was 15.85 per hour.

(ROI) on the pixel detector surface. From 5135 events identified as alphas, 46 were in the ROI. Thus, estimated alpha background rate in the ROI was  $0.14 \pm 0.02$  events per

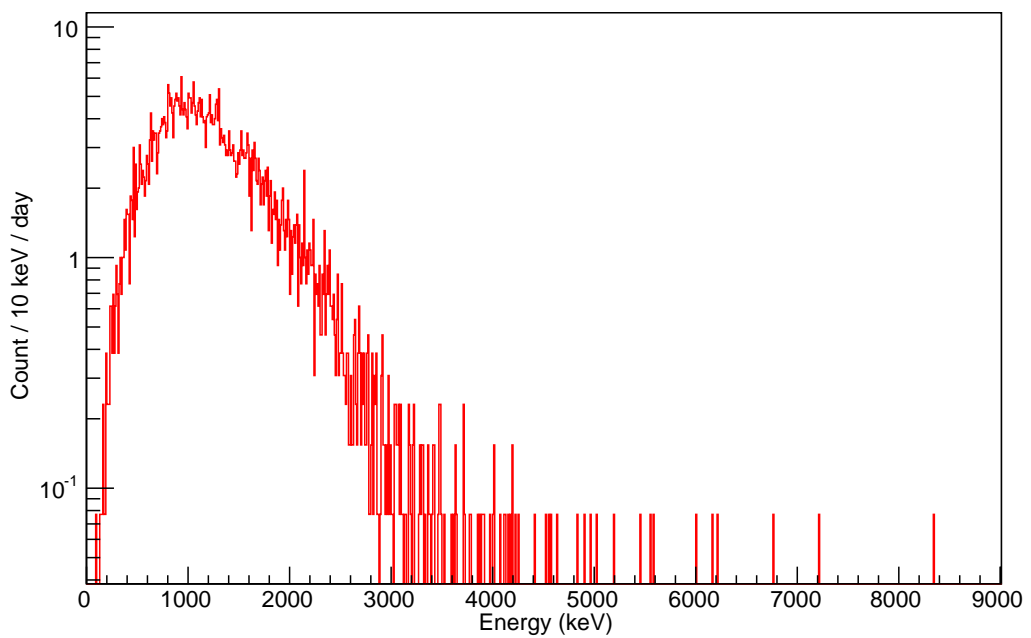


Figure 7.9: Electron spectrum from surface measurement using CdTe SPD. Duration of measurement was 13.5 days and observed rate of electron events was 23.11 per hour.

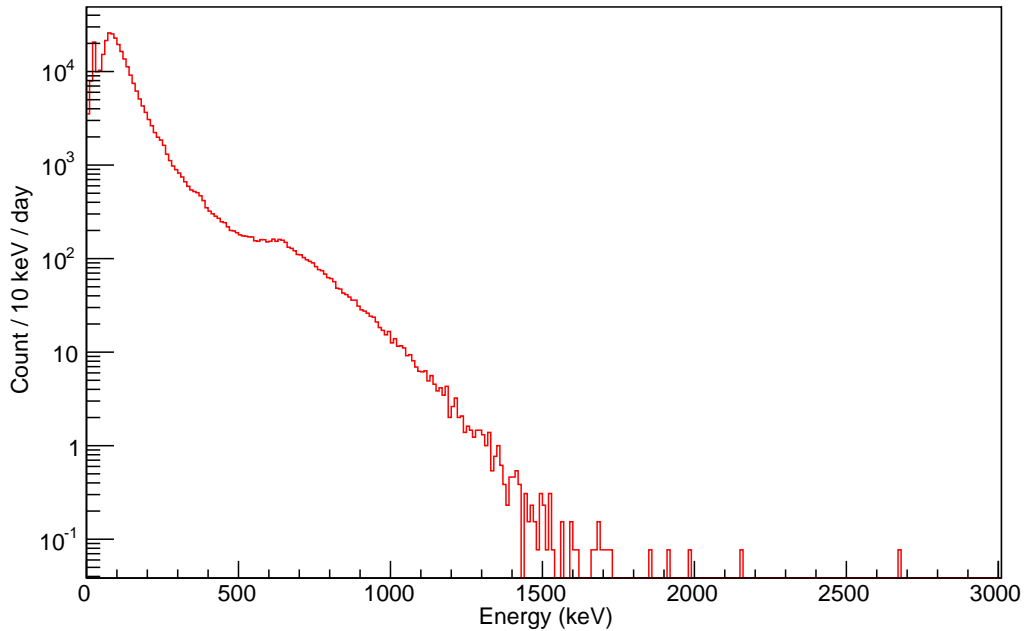


Figure 7.10: Spectrum of small clusters (sizes up to 10 pixels) from surface measurement using CdTe SPD. Duration of measurement was 13.5 days and observed rate of events was 11621.09 per hour.

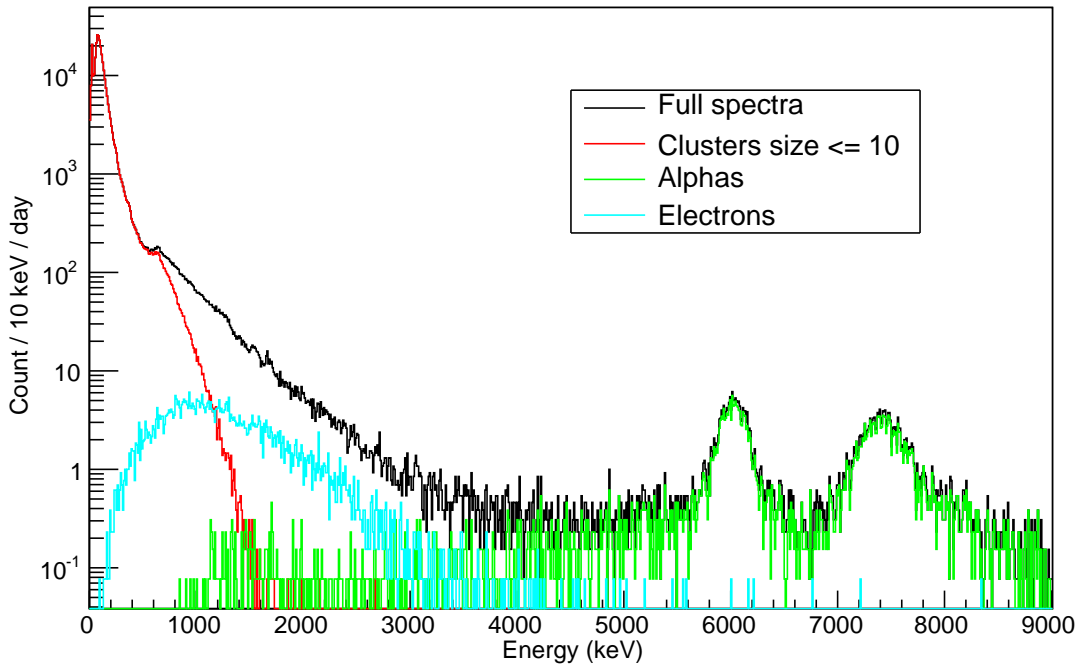
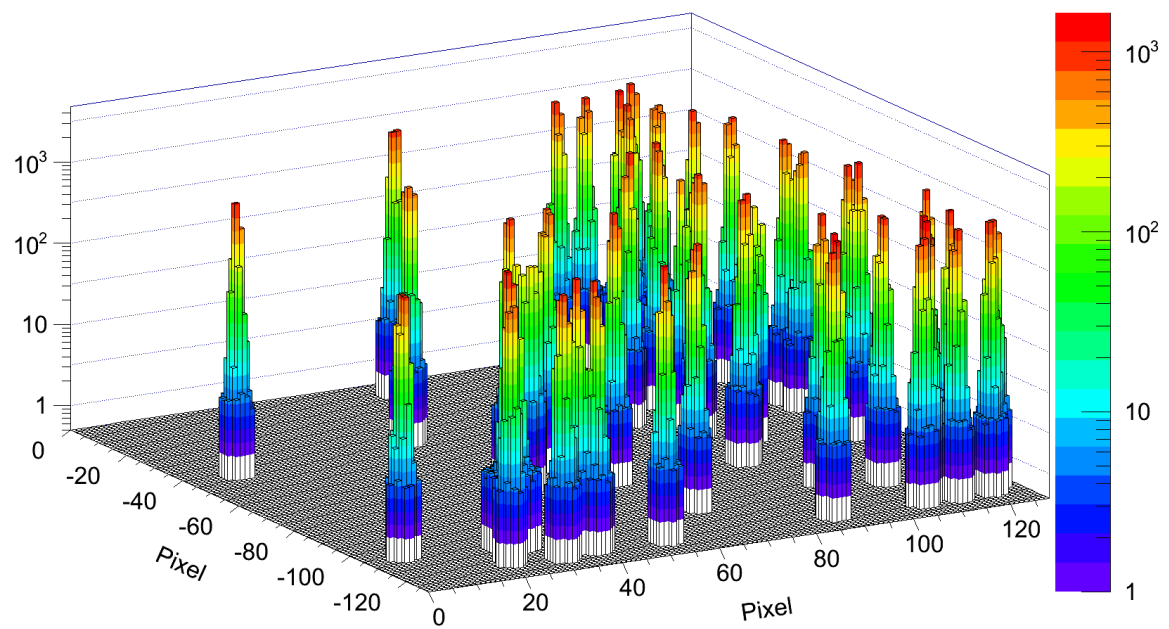


Figure 7.11: Comparison of alpha, electron and small clusters ( $\leq 10$  pixels) spectra with full spectrum, from surface measurement using CdTe SPD.

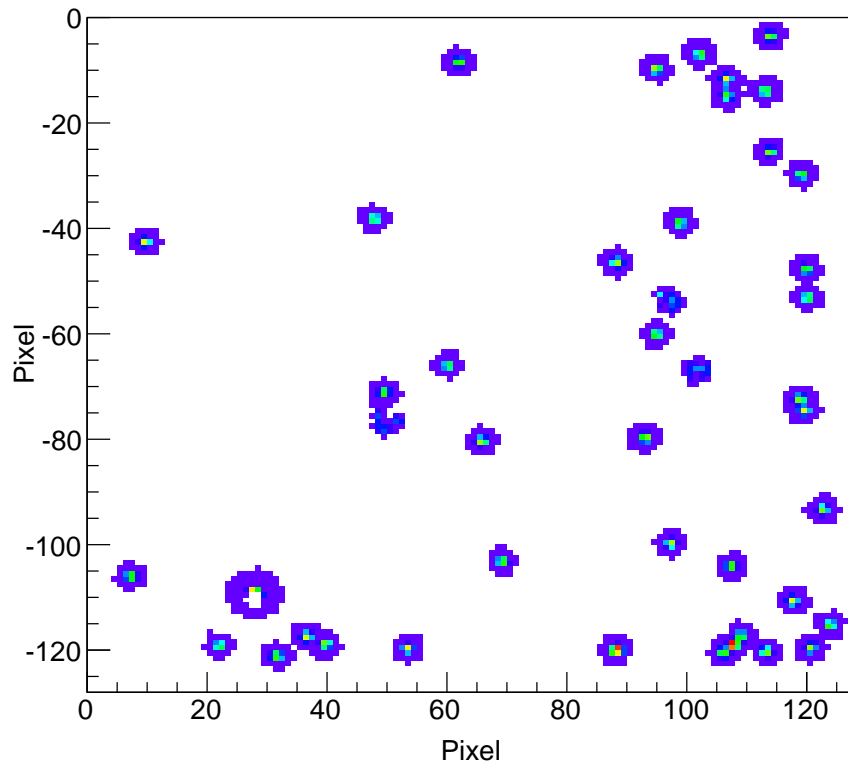
hour. Figure 7.13 shows the spatial distribution of electrons in the ROI on pixel detector surface. In total, 169 electrons were in the ROI and thus the estimated electron rate was  $0.52 \pm 0.04$  events per hour. Table 7.1 summarizes the surface background measurement results discussed above.

	0 - 10 MeV	2.5 - 3 MeV
Alphas/h	$15.85 \pm 0.22$	$0.14 \pm 0.02$
Electrons/h	$23.11 \pm 0.27$	$0.52 \pm 0.04$

Table 7.1: Estimated background rates from CdTe SPD surface measurements for a duration of 13.5 days. The region of interest (ROI) is 2.5 - 3 MeV.

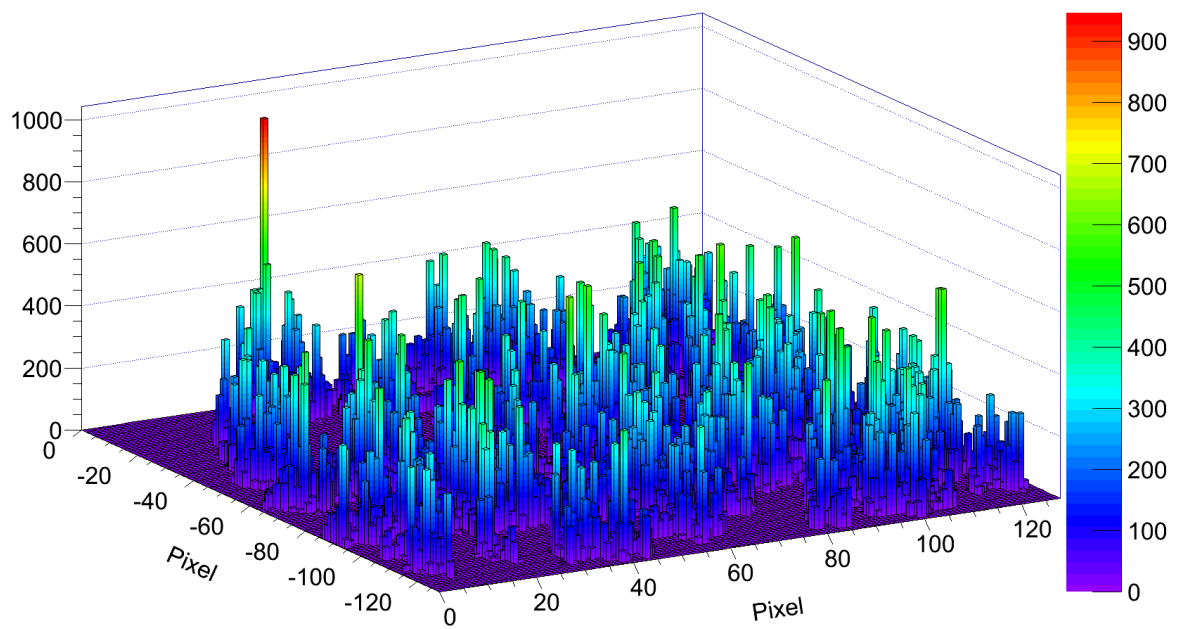


(a) 3D view of the alpha clusters.

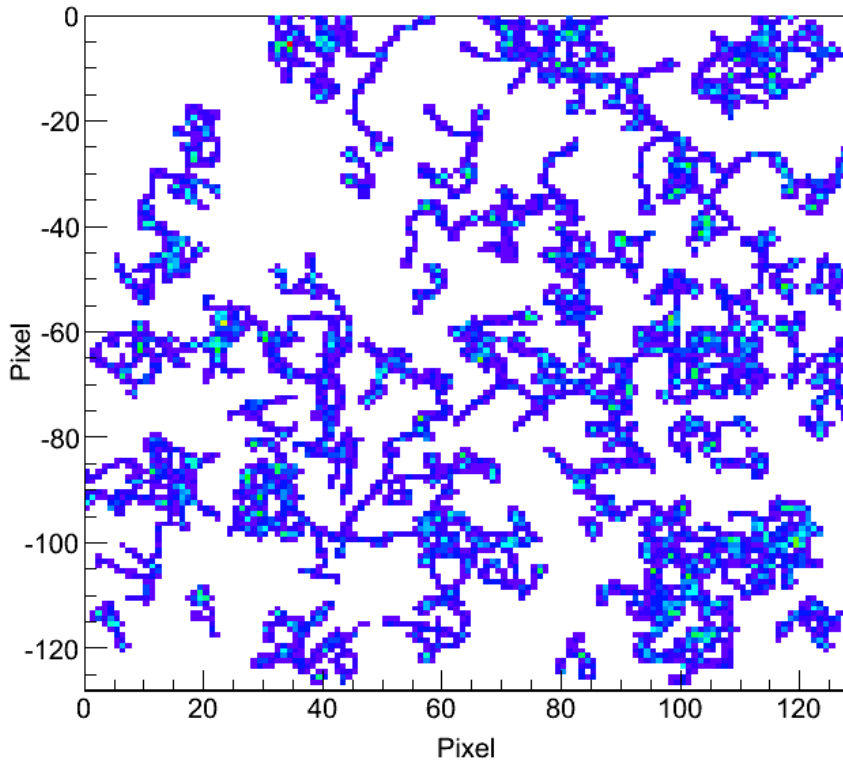


(b) 2D plot of the alpha clusters.

Figure 7.12: Accumulated frame of alpha clusters in the 2.5 - 3 MeV region from the surface measurement with CdTe SPD.



(a) 3D view of the electron tracks.



(b) 2D plot of the electron tracks.

Figure 7.13: Accumulated frame of electron clusters in the 2.5 - 3 MeV region from the surface measurements with CdTe SPD.

## 7.2 Underground measurements

Underground measurements were performed in the LNGS laboratory, Gran Sasso, Italy using the same detector as for surface measurement. Detector was covered with 10 cm of Pb. The detector installation inside the shielding can be seen in the Figure 7.14. Two sets of data were collected from underground laboratory, one with nitrogen ( $N_2$ ) flushing for 45 days and another without  $N_2$  flushing for 11 days.



Figure 7.14: Shielding used in the underground measurements at LNGS. The CdTe SPD was kept inside the Al box and covered by 10 cm of lead.

Data set	0 - 10 MeV (counts/h)	2.5 - 3 MeV (counts/h)
Surface, no $N_2$ flushing	$11818.46 \pm 6.04$	$2.47 \pm 0.09$
Underground, no $N_2$ flushing	$87.46 \pm 0.58$	$0.06^{+0.02}_{-0.01}$
Underground, with $N_2$ flushing	$78.43 \pm 0.27$	$0.02^{+4.45 \times 10^{-3}}_{-3.89 \times 10^{-3}}$

Table 7.2: Estimated background rates (all events) from surface and underground (with and without  $N_2$  flushing) measurements using CdTe SPD. Total time of measurement was 13.5, 11 and 45 days for surface, underground without  $N_2$  flushing and underground with  $N_2$  flushing data, respectively. The region of interest is 2.5 - 3 MeV.

Table 7.2 summarizes the total events rates for those above mentioned underground measurements and the surface measurement. The Figure 7.15 compares the full spectra from underground measurements with and without  $N_2$  flushing. It can be clearly seen that two alpha peaks with energies 6 and 7.69 MeV from  $^{218}\text{Po}$  and  $^{214}\text{Po}$  was highly suppressed when flushed with  $N_2$ . Also, above 3 MeV the background is reduced significantly which indicates good alpha suppression using  $N_2$  flushing. In the low energy region ( $< 2$  MeV) both spectra are identical. The observed rate of all events in the case

of no  $\text{N}_2$  flushing was 87.46 events per hour, whereas in the case of  $\text{N}_2$  flushing it was 78.43. Figure 7.16 compares the underground background spectrum (with  $\text{N}_2$  flushing) with surface spectrum (without  $\text{N}_2$  flushing). As expected, there is significant reduction in the background in the underground measurement compared to surface measurement. Background reduction by a factor of 150 was observed in the underground measurement with  $\text{N}_2$  flushing compared to surface measurement without  $\text{N}_2$  flushing.

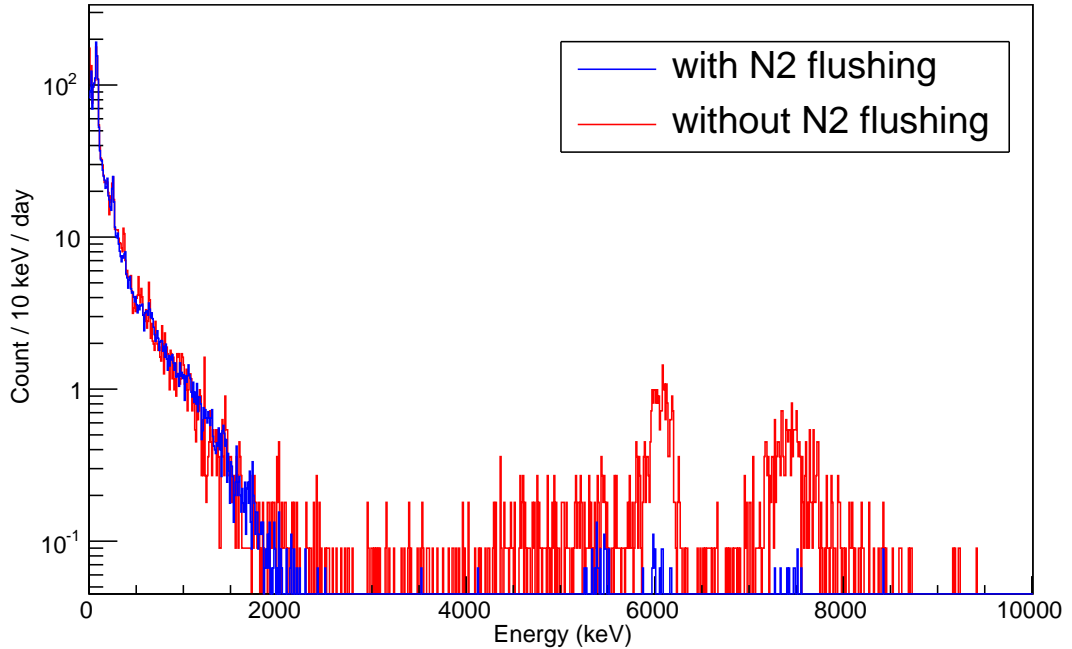


Figure 7.15: Comparison of full spectra from underground measurements with (87.46 events/h) and without  $\text{N}_2$  flushing (78.43 events/h) using CdTe SPD. Total time of measurement was 11 and 45 days for without  $\text{N}_2$  flushing and with  $\text{N}_2$  flushing data, respectively.

From underground data alphas, electrons and small cluster events ( $\leq 10$  pixels) were also identified based on the criteria used for surface data. Table 7.3 summarizes the classification results and compares with surface measurements. Figure 7.17 shows the alpha spectrum from measurements with  $\text{N}_2$  flushing. The rate of alphas (events/h) were 2.70 and 0.29 for measurement without and with  $\text{N}_2$  flushing, respectively. Interestingly, in the underground data there are three visible alpha peaks including 5.3 MeV from  $^{210}\text{Po}$  (indicates the presence of  $^{210}\text{Pb}$ ). It shows large exposition of detector to Rn atmosphere, thus possibility to store detectors in Rn free atmosphere must be considered. Figure 7.18 shows the electron spectrum from underground measurement with  $\text{N}_2$  flushing. Observed electron events per hour was 0.61 in the data without  $\text{N}_2$  flushing, whereas the rate in the data with flushing was 0.44. The Figure 7.19 is spectrum from the small clusters ( $\leq 10$  pixels) from measurements with  $\text{N}_2$  flushing (75.2 events/h). Figure 7.20 plots the above mentioned alpha, electron and small clusters spectra along with the full spectrum in one plot. The full spectrum can be seen as a combination of other spectra.

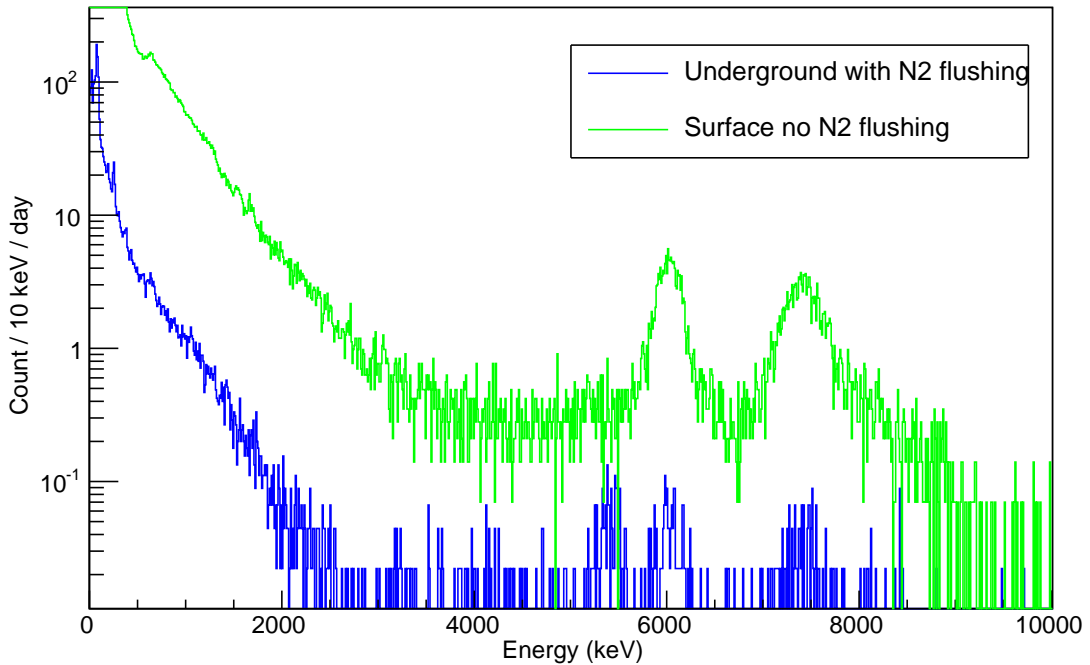


Figure 7.16: Comparison of full spectra from underground measurements with  $\text{N}_2$  flushing (78.43 events/h) and surface measurement without  $\text{N}_2$  (11818.46 events/h) using CdTe SPD. Total time of measurement was 45 and 13.5 days for underground and surface data, respectively.

The energy region 2.5 - 3 MeV (ROI) was further studied for better understanding of background for  $0\nu\beta\beta$  events. Accumulated frame of alphas in ROI from the measurement with  $\text{N}_2$  flushing is shown in the Figures 7.21. Out of 316 alpha events from 45 days of data, 10 were identified in the ROI ( $9.26 \times 10^{-3}$  events/h). In the case of data without  $\text{N}_2$  flushing the rate of alpha events in ROI was 0.03. Figure 7.22 shows the accumulated frames of electrons identified from the data with  $\text{N}_2$  flushing. Only two events were identified as electron in the ROI ( $1.85 \times 10^{-3}$  events/h). By studying the 3D signature of these electrons (see Figure 7.22a) it was assumed (with high probability) that they are from single electrons as only one bragg peak is visible in the track structure. Based on the preliminary analysis there were no background events for two electrons during 45 days of measurement in LNGS.

The results presented here are preliminary and further improvements of the cluster identification is necessary. It should be also mentioned that the measurements were done with a detector which was not tuned for low background experiments (PCB, components and support structures). A new low background coincidence setup (using CuFlon Pixel Telescope design) is being prepared and soon it will be installed in the LSM underground laboratory for further background measurements.

Data set	Alphas/h		Electrons/h	
	0 - 10 MeV	2.5 - 3 MeV	0 - 10 MeV	2.5 - 3 MeV
Surface, no N <sub>2</sub>	15.85 ± 0.22	0.14±0.02	23.11±0.27	0.52 ± 0.04
Underground, no N <sub>2</sub> flushing	2.70 ± 0.10	0.03± 0.01	0.61 ± 0.05	0.01 <sup>+8.73×10<sup>-3</sup><sub>-7.18×10<sup>-3</sup></sub></sup>
Underground, with N <sub>2</sub> flushing	0.29 ± 0.02	$9.26\times10^{-3}$ $^{+3.53\times10^{-3}}$ $_{-2.98\times10^{-3}}$	0.44 ± 0.02	$1.85\times10^{-3}$ $^{+2.09\times10^{-3}}$ $_{-1.17\times10^{-3}}$

Table 7.3: Estimated background rates from underground measurements (with and without N<sub>2</sub> flushing) in comparison to surface measurements (without N<sub>2</sub> flushing). Total time of measurement was 13.5, 11 and 45 days for surface, underground without N<sub>2</sub> flushing and underground with N<sub>2</sub> flushing data, respectively. The region of interest (ROI) is 2.5 - 3 MeV.

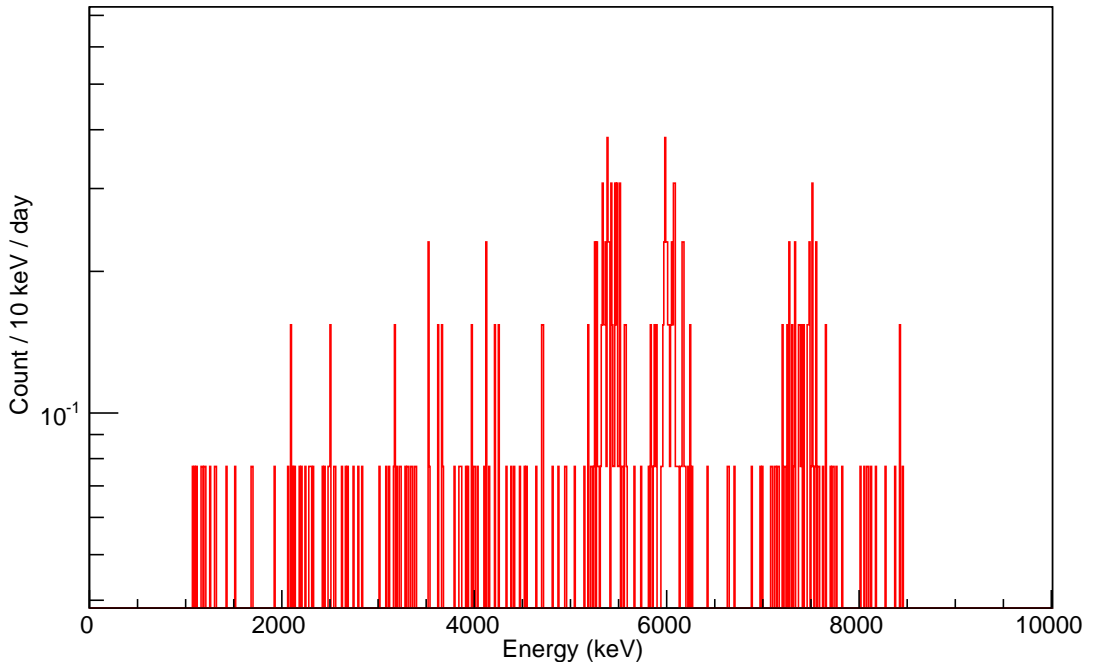


Figure 7.17: Alpha spectrum from underground measurements with N<sub>2</sub> flushing. Total time of measurement was 45 days and observed alphas rate was 0.29 events/h.

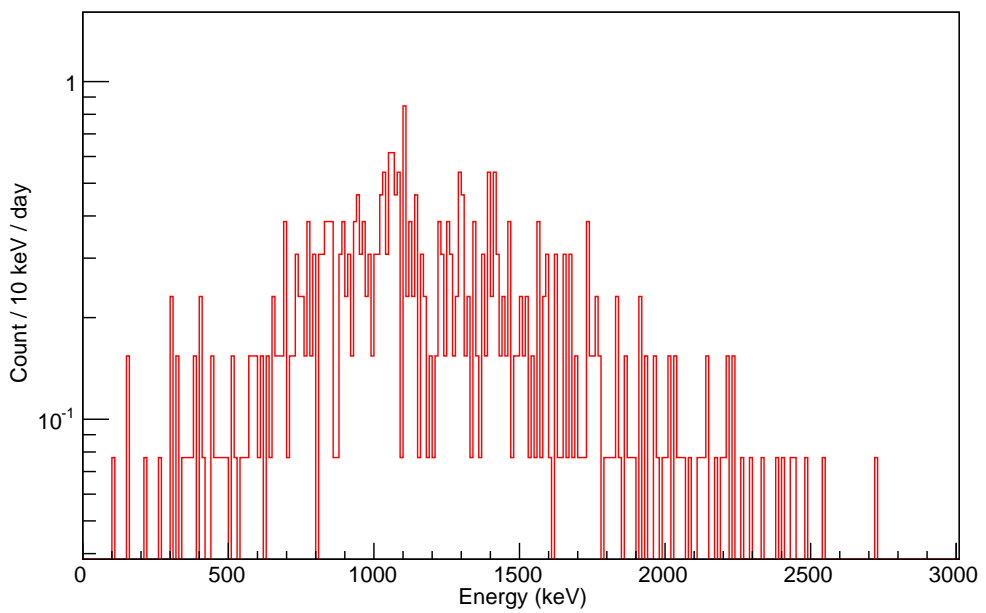


Figure 7.18: Electron spectrum from underground measurements with  $\text{N}_2$  flushing. Total time of measurement was 45 days and observed electrons rate was 0.44 events/h.

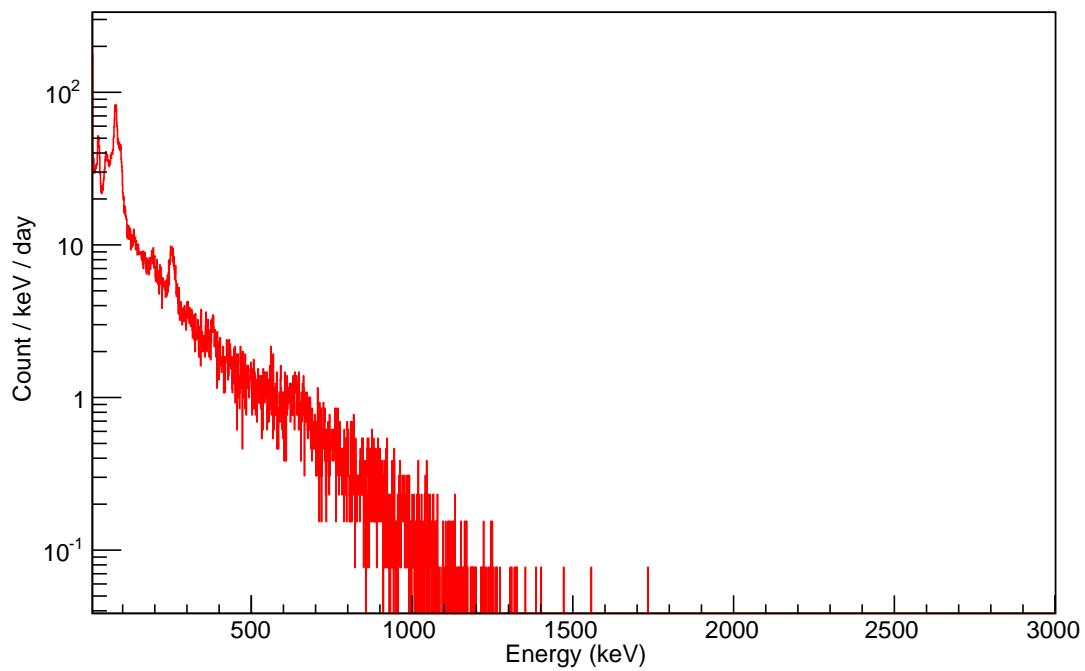


Figure 7.19: Spectrum of events with size  $\leq 10$  pixels from underground measurements with  $\text{N}_2$  flushing. Total time of measurement was 45 days and observed rate was 75.20 events/h.

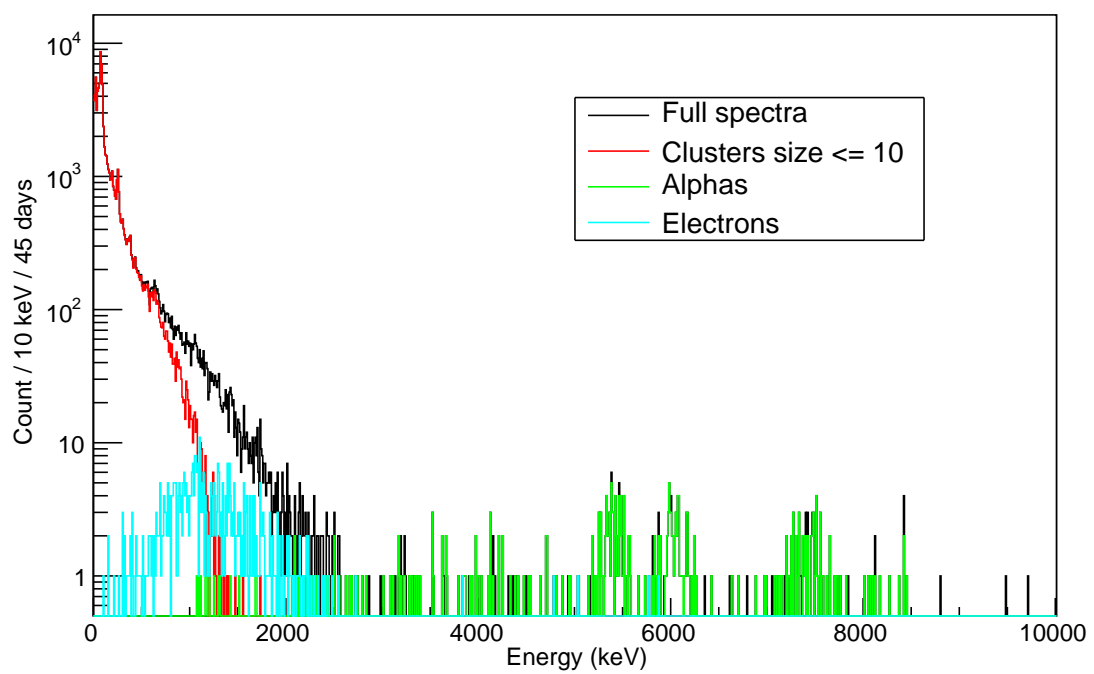
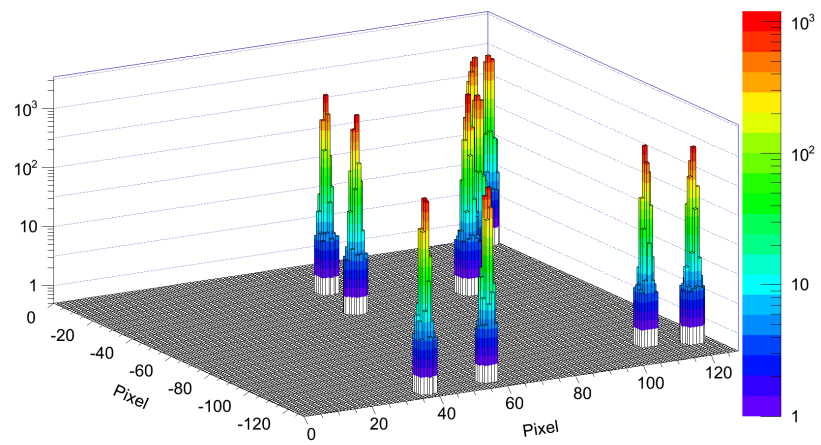
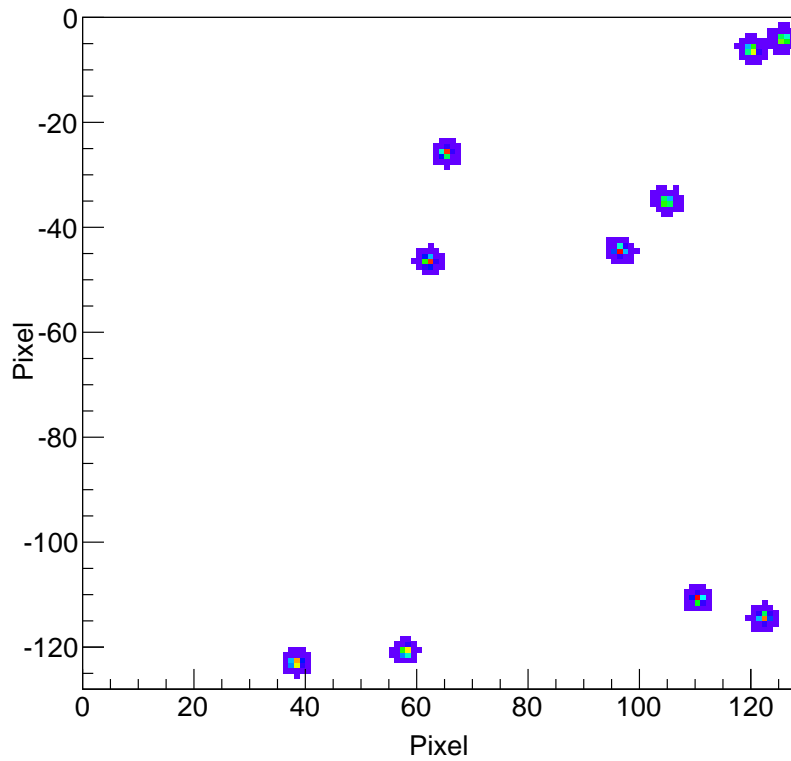


Figure 7.20: Electron alpha and small clusters spectra compared to full spectrum, from underground measurements with N<sub>2</sub> flushing.

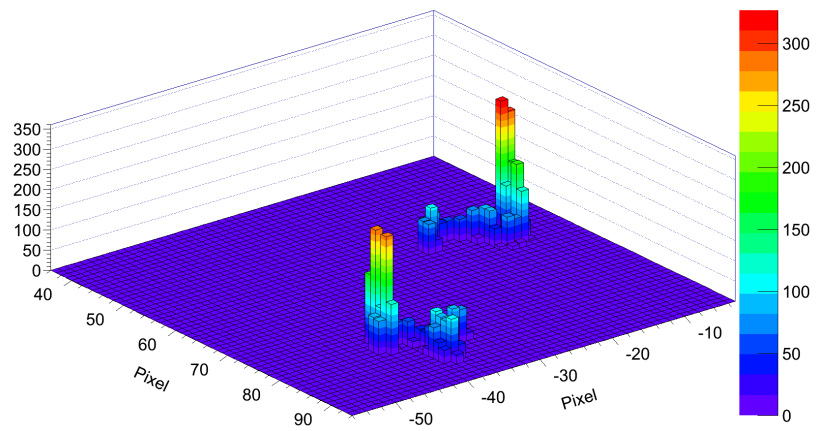


(a) 3D view of the tracks.

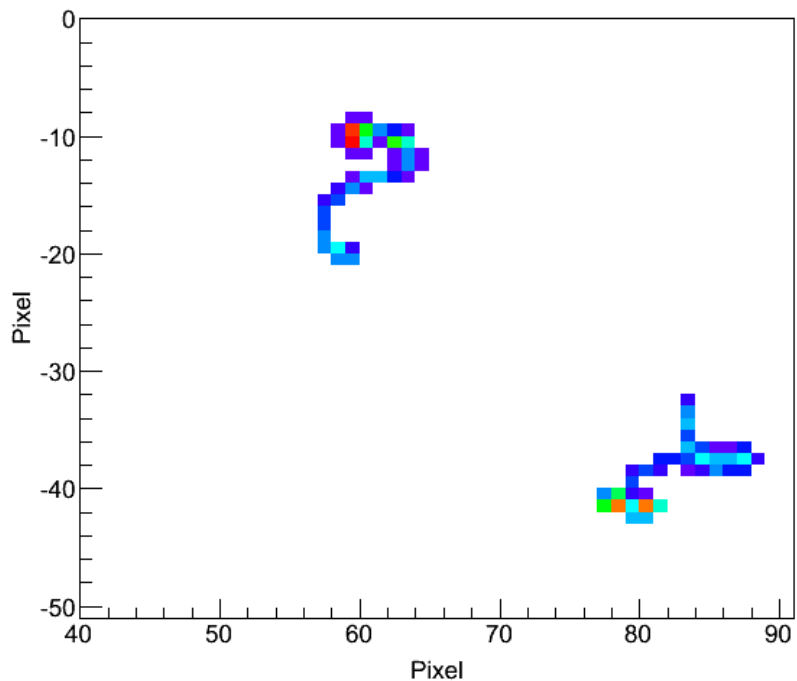


(b) 2D plot of the tracks.

Figure 7.21: Accumulated tracks of alphas in 2.5 - 3 MeV region from the LNGS measurements (with 10 cm Pb shielding and N<sub>2</sub> flushing against Rn) with CdTe SPD.



(a) 3D view of the tracks.



(b) 2D plot of the tracks.

Figure 7.22: Accumulated tracks of electrons in 2.5 - 3 MeV region from the LNGS measurements (with 10 cm Pb shielding and N<sub>2</sub> flushing against Rn) with CdTe SPD.

# Chapter 8

## SPT background measurements

Extensive background measurements were performed to understand the quality of pixel detector technology for  $2\nu EC/EC$  decay of  $^{106}\text{Cd}$ . Three different setups were used in the background measurements. At first a standard Timepix Silicon pixel detector was used in the measurements. Later, other two setups called CuFlon and Flex-Rigid Si Pixel Telescope (SPT) both from cleaner PCB materials were designed and background measurements were performed. Measurements were conducted on the surface at IEAP and in the underground laboratory at LSM, France. Initially, a simple shielding of 5 cm Pb was used in the measurements and later a comprehensive shielding was installed in the underground laboratory for background studies and future measurements. In order to judge the performance of SPT system, the background measurement from TGV II (with natural Cd foils between detectors) was studied and then compared with SPT background results. Results from the background estimation of TGV II system is presented in the next section.

### 8.1 TGV II background

The readout architecture of TGV II setup is shown in Figure 8.1. There are 32 detectors (arranged as 16 pairs) where detector diameter is 60 mm (sensitive diameter 51 mm) and detector thickness is 6 mm. The setup has a total sensitive volume of  $400 \text{ cm}^3$  and a mass of 3 kg. Energy resolution of the detectors ranges from 3 to 4 keV at 1332 keV ( $\gamma$  rays from  $^{60}\text{Co}$ ). Whole setup is covered with three layers of shielding made of 16 cm borated polyethylene, 10 cm Pb and 20 cm Cu (see Figures 8.2 and 8.3). For the background measurement from which the results are presented here, natural Cd was used as source foil in between the detector pairs [2]. The thickness of the Cd foil used was 50  $\mu\text{m}$ .

Each HPGe detector is connected to a spectroscopic amplifier (SA) unit and SA gives three outputs from a single event. Two of the three outputs provide energy information (integrated with different shaping times: 2  $\mu\text{s}$  and 8  $\mu\text{s}$ ) and the third is used for trigger generation. The signals with different shaping times are used in the microphonic noise reduction technique to remove the false signals [86]. In Germanium detectors especially in lower energy region, the mechanical vibrations converts to microphonic noise signals (non radiation noise) of low frequency. In the case of such noisy signal, SA output path

with short shaping time (cut off frequency is higher) filters the signal, but the signals originating from true events give comparable output in both channels. The longer the shaping time the better the signal to noise ratio achieved, thus the  $8 \mu\text{s}$  output channel is preferred for the energy information. There are in total eight Analog to Digital Converters (four each for  $2 \mu\text{s}$  and  $8 \mu\text{s}$  channels) which are multiplexed appropriately to the 32 detectors. The third output from the spectroscopic amplifier unit connects to a Master Trigger unit (MT) and used in generating a fast trigger signal. These fast trigger signals multiplex the fired detectors to ADCs and also handles the coincidence. The coincidence window for the events is in the order of  $\mu\text{s}$ .

Data from a background run of 2965 hours (124 days) was analyzed and results are presented here. In the raw data, there were in total 584597 events ( $6.16 \text{ events/detector/h}$ ) and in the Region of Interest (ROI, 19-23 keV) were 17831 ( $0.19 \text{ events/detector/h}$ ) events. After applying coincidence criterion (maximum two simultaneous hits in all the detectors) the rate was  $1.15 \text{ events/detector/h}$  and in ROI was  $0.08 \text{ events/detector/h}$ . Additionally, microphonic noise suppression can be utilized to further suppress the background events. If the difference in the outputs of  $8 \mu\text{s}$  and  $2 \mu\text{s}$  channels for the same event are more than 1.5 keV, they were considered as noisy events and removed. With the addition of microphonic noise suppression the rate was  $0.57 \text{ events/detector/h}$  and in the ROI was  $0.04 \text{ events/detector/h}$ . With all the noise reduction criteria applied the Double Side Event rate was  $9.57 \times 10^{-2} \text{ events/detector pair/h}$  and in ROI was  $1.48 \times 10^{-4} \text{ events/detector pair/h}$ . The rate of single event on detector pair and satisfying microphonic suppression (can be considered as Single Side Event with the assumption that the two coincident events registered in the same detector and thus deposited in total 42 keV) was  $3.52 \text{ events/detector pair/h}$  and in the 40 - 44 keV region rate was  $0.10 \text{ events/detector pair/h}$ . Table 8.1 summarize the background results discussed above. Figure 8.4 shows the scatter plot of events with different noise reduction criteria and Figure 8.5 compares the spectra with above conditions.

	Total (counts/detector/h)	in 19-23 keV (counts/detector/h)
All events	$6.16 \pm 8.06 \times 10^{-3}$	$0.19 \pm 1.41 \times 10^{-3}$
All events (with coincidence)	$1.15 \pm 3.49 \times 10^{-3}$	$0.08 \pm 9.20 \times 10^{-4}$
All events (with all criteria)	$0.57 \pm 2.45 \times 10^{-3}$	$0.04 \pm 6.75 \times 10^{-4}$
	Total (counts/detector pair/h)	in 19-23 keV (counts/detector pair/h)
DSE event	$0.43 \pm 4.06 \times 10^{-3}$	$3.58 \times 10^{-4} \pm 1.58 \times 10^{-4}$
DSE (with all criteria)	$9.57 \times 10^{-2} \pm 1.42 \times 10^{-3}$	$1.48 \times 10^{-4} {}^{+ 6.97 \times 10^{-5}}_{- 5.79 \times 10^{-5}}$
	Total (counts/detector pair/h)	in 40-44 keV (counts/detector pair/h)
SSE event	$8.37 \pm 0.015$	$0.19 \pm 2.35 \times 10^{-3}$
SSE (microphonic suppression)	$3.52 \pm 8.61 \times 10^{-3}$	$0.10 \pm 1.47 \times 10^{-3}$

Table 8.1: Estimated TGV II background rates from a background run with natural Cd foil between the detector pairs (all criteria  $\Rightarrow$  with coincidence and microphonic suppression). Total duration of measurement was 2965 hours.

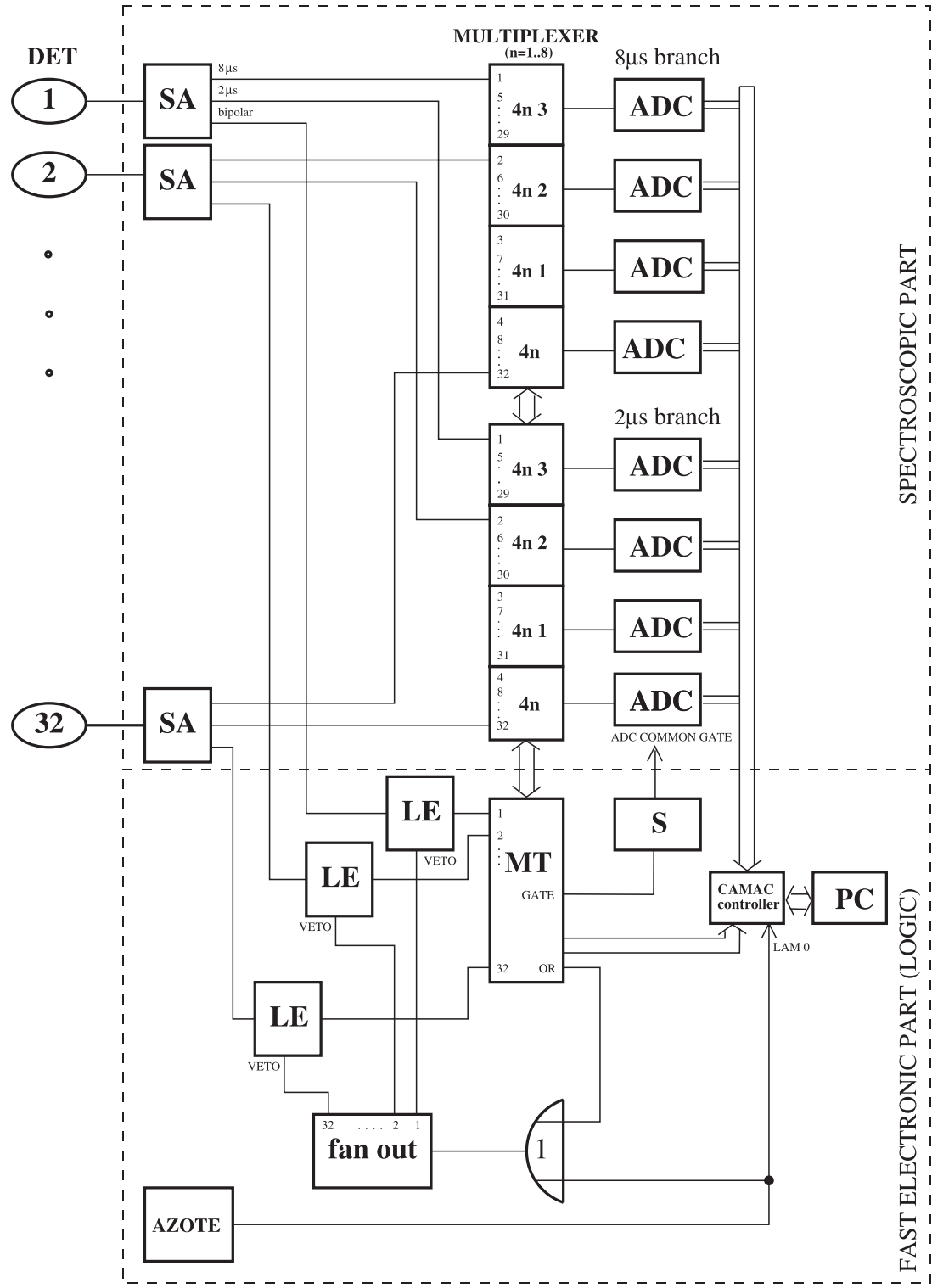


Figure 8.1: The schematic of electronics readout for the TGV II measurement setup (DET - detectors 1 to 32 including preamplifiers, SA - spectroscopic amplifier, ADC - analog to digital converter, LE - leading edge discriminator, S - shaper, MT - master trigger, AZOTE - LN2 filling facility)[49].



Figure 8.2: TGV II shielding outer view.

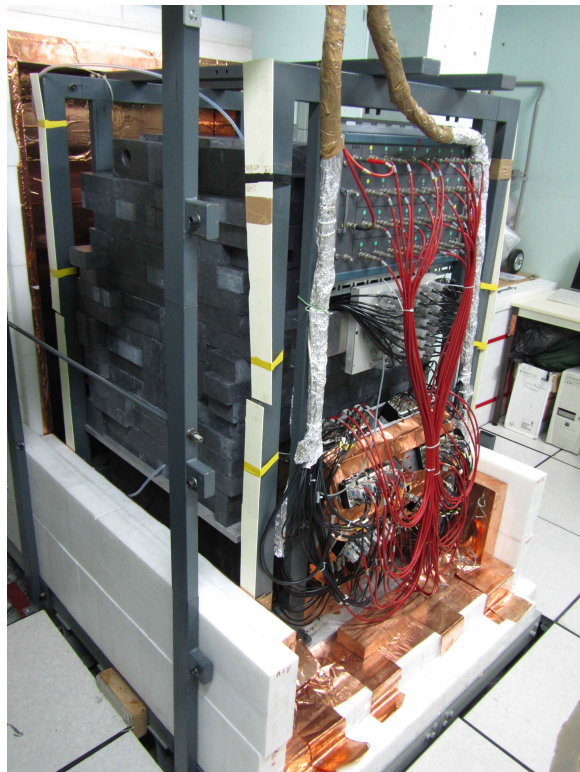


Figure 8.3: TGV II inner Pb shielding and electronics.

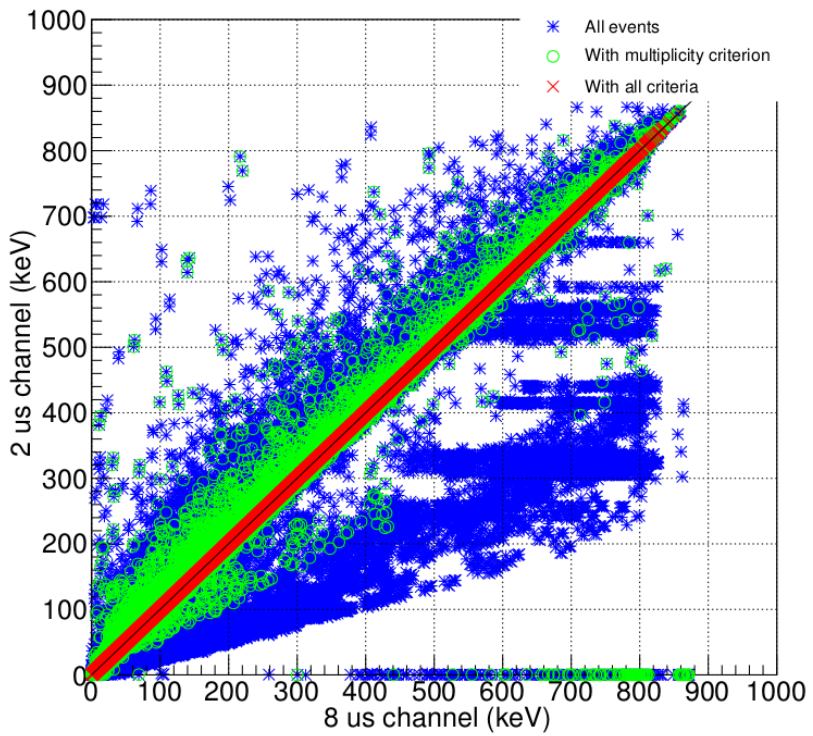


Figure 8.4: Scatter plot ( $2 \mu\text{s}$  vs  $8 \mu\text{s}$  shaping times) of SA output from TGV II detectors for raw data (blue), coincident events (green) and events satisfying coincidence and microphonic noise suppression (red).

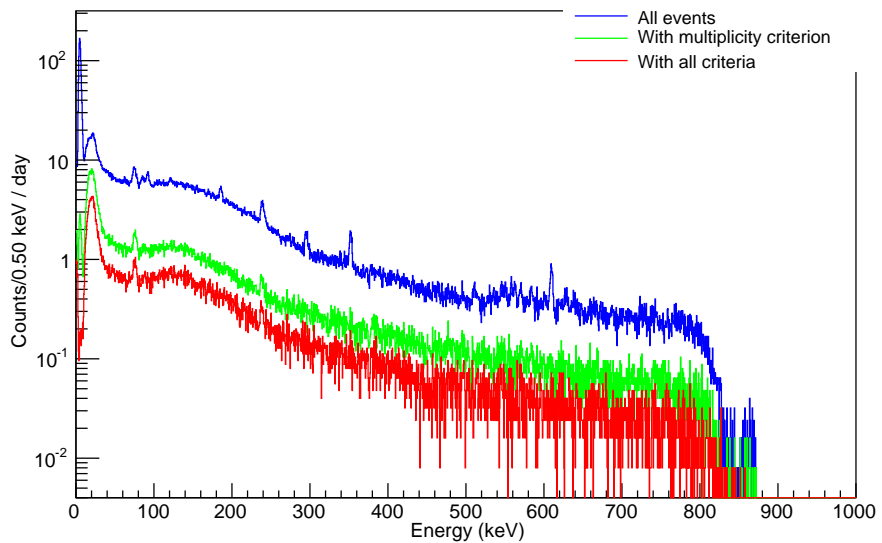


Figure 8.5: Full spectrum comparison between all events, coincident events (satisfying multiplicity criterion) and events satisfying coincidence and microphonic suppression criteria (all criteria) of TGV II background measurement.

## 8.2 Si Pixel Telescope (SPT) background measurements for $2\nu EC/EC$ decay of $^{106}\text{Cd}$

To estimate the feasibility of pixel detector technique in the low background experiments such as double electron capture of  $^{106}\text{Cd}$ , good understanding of background events is important. The background has been studied for three different pixel detector configurations:

- ◊ Standard version of Si pixel detector (CERN version on FR4 board), so called Single Pixel Detector (SPD),
- ◊ Stack of two Si pixel sensors (face-to-face arrangement) using CuFlon boards, so called CuFlon Si Pixel Telescope (SPT),
- ◊ Stack of two Si pixel sensors (face-to-face arrangement) using flex-rigid board, so called Flex-Rigid SPT.

Measurements were performed on the surface at IEAP, CTU in Prague (using simple 5 cm Pb shielding) and in the underground laboratory LSM, France (using a simple as well as the sophisticated shielding). Detailed description of measurement setups and obtained results are presented in the next sections.

### 8.2.1 Si Single Pixel Detector (standard version)

One silicon Single Pixel Detector (SPD) was used as the first step in the background measurements in the LSM underground laboratory. Pixel pitch of the detector was 55  $\mu\text{m}$  and thickness of the Si sensor was 300  $\mu\text{m}$ . The detector was shielded using Pb layer of 5 cm thickness from all sides. The results presented here are from a measurement of approximately 9 days long. Table 8.2 lists the estimated background rates from the data. Figure 8.6 is the full spectrum from the measurements and the observed rate (per hour) of all events was 150.48. The observed Single Side Events (SSE) background rate was 2.46 events/h and the SSE spectrum is shown in Figure 8.7. Figure 8.8 is distribution of distance between interaction points in the SSE events. The SSE distance distribution has a peak near to zero which indicates that majority of background double events occurs in the adjacent pixels or adjacent pixels are activated by hit pixels. After applying distance cut (removing events which are outside 0.7 - 4 mm range) the SSE rates was reduced to 0.19 events/h and in ROI to 0.02 events/h. The SPD background (SSE events) compared to TGV II (DSE events, as SSE background is very high and not used in TGV data analysis) background rate is approximately factor two more ( $9.57 \times 10^{-2}$  events/h for TGV II, 0.19 events/h for SPD). Rates of events in the region of interest (ROI) is much worse, as the SPD rate is a factor 135 more than TGV background rates. It shows that standard pixel detector is not optimized for the low background experiments.

All events/h		SSE/h		SSE with dist./h	
Total	ROI	Total	ROI	Total	ROI
$150.48 \pm 0.83$	$4.60 \pm 0.14$	$2.46 \pm 0.11$	$0.23 \pm 0.03$	$0.19 \pm 0.03$	$0.02 \pm 0.01$

Table 8.2: Results of Si SPD background measurements, from underground data (219 h) with 5 cm lead shielding. The region of interest (ROI) is 19 - 23 keV. All numbers are normalized per hour.

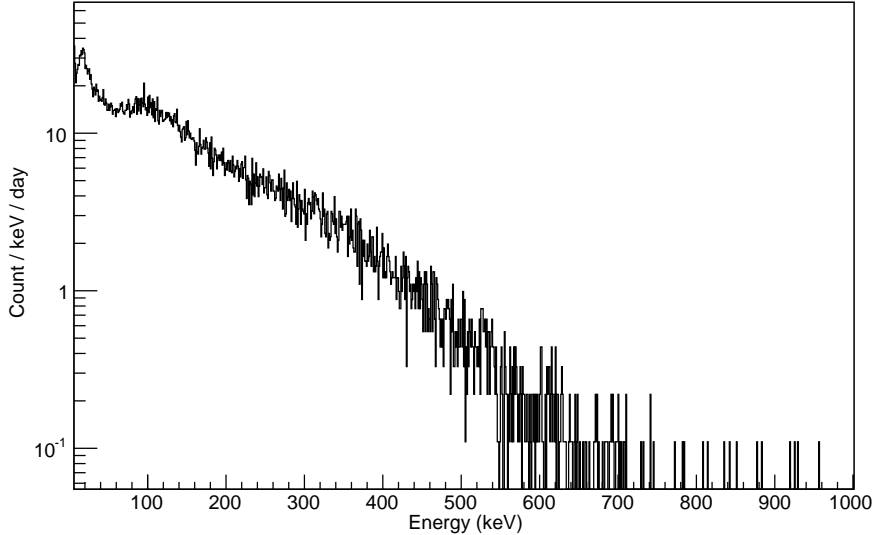


Figure 8.6: Full spectrum of background measured using CERN Si SPD in the underground, shielded with 5 cm Pb (219 h). The background rate was 3612 events/day.

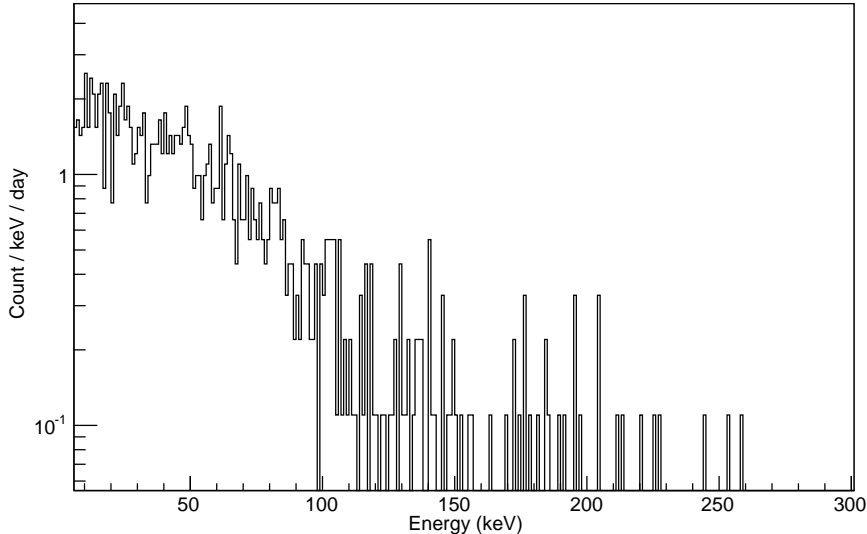


Figure 8.7: SSE spectrum from background measured using CERN Si SPD in the underground, shielded with 5 cm Pb (219 h). The SSE background rate was 59 events/day.

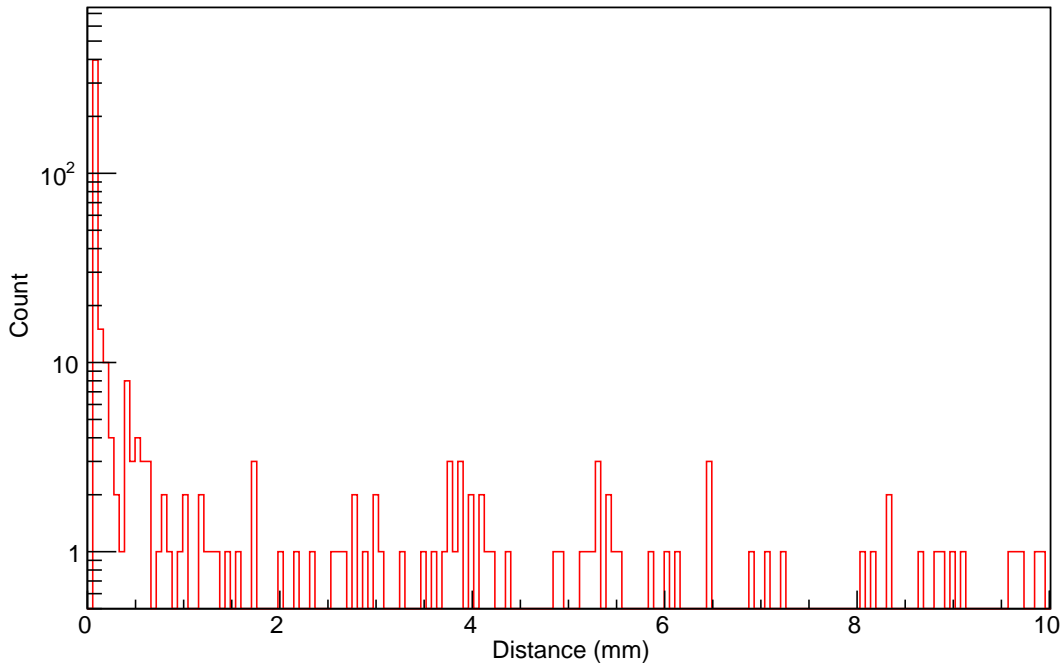


Figure 8.8: SSE distance distribution of CERN Si SPD from underground background measurements shielded with 5 cm Pb (219 h).

### 8.2.2 CuFlon Si Pixel Telescope

Newly designed and produced CuFlon SPT unit consists of a pair of Timepix detectors with pixel pitch 55  $\mu\text{m}$  and 300  $\mu\text{m}$  thick sensors. Background measurements were performed on the surface and in the underground with this setup.

#### Surface measurements

On the surface, measurements were performed with and without shielding. The shielding arrangement was 5 cm of Pb from all sides of the setup. Table 8.3 lists the estimated background rates from these measurements. Figure 8.9 compares the shielded and unshielded measurement spectra from surface measurements. The visible peak in the spectrum with shielding is due to the MIPS/muons passing through the detector vertically, as detector was aligned parallel to earth surface. This fact is more clear in the SSE and DSE spectrum of unshielded measurement shown in Figure 8.10, where DSE spectrum has the peak, and in SSE spectrum it is missing. The Figure 8.11 shows the distance distribution of SSE and DSE events from the measurements without shielding. The SSE distance distribution is comparable to the SPD whereas the DSE events have a peak near to zero from the events which are passing through both detectors, mainly originating from cosmic muons.

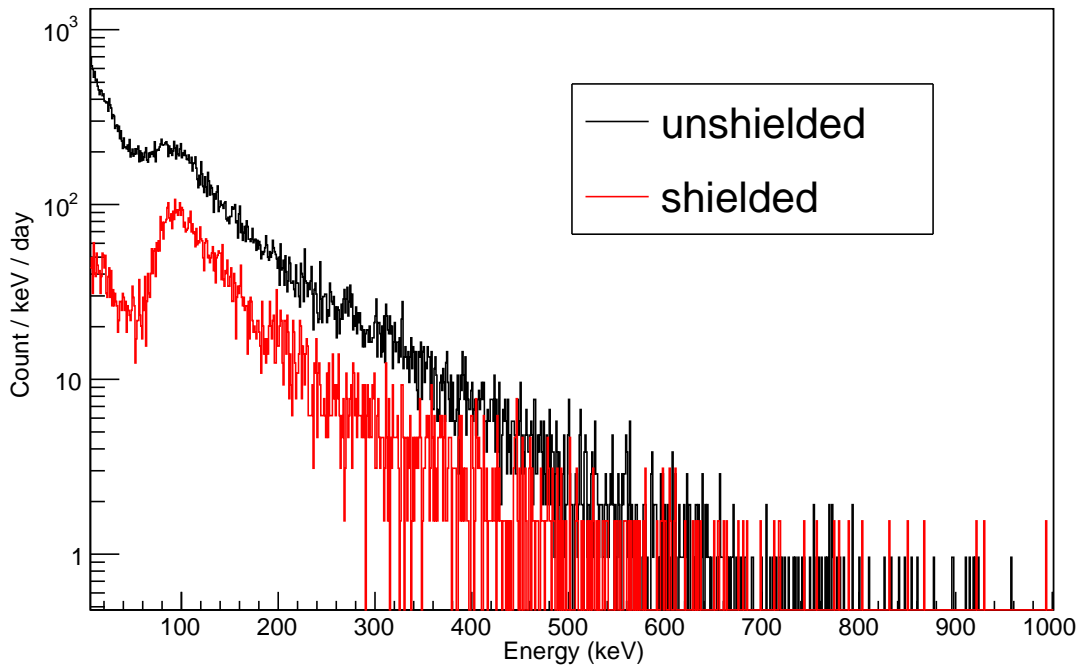


Figure 8.9: Spectra from CuFlon SPT surface measurements, with 5 cm Pb shielding (15.5 h of measurement) and without any shielding (25 h of measurement). The observed background rate was 42599 events/day for unshielded measurement and 6574 events/day for shielded measurements.

Dataset	All events/h		SSE/h		DSE/h	
	Total	in ROI	Total	in ROI	Total	in ROI
No shield	$1703.96 \pm 8.26$	$66.20 \pm 1.63$	$16.24 \pm 0.81$	$0.72 \pm 0.17$	$20.08 \pm 0.90$	$0.12^{+0.09}_{-0.08}$
Shielded	$424.13 \pm 5.23$	$7.35 \pm 0.69$	$1.10^{+0.31}_{-0.27}$	$0.19^{+0.15}_{-0.12}$	$8.77 \pm 0.75$	$0.06^{+0.11}_{-0.04}$

Table 8.3: Estimated background rates from CuFlon SPT surface measurements, with (15.5 h of measurement) and without (25 h of measurement) lead shielding. The region of interest (ROI) is 19 - 23 keV. All numbers are normalized per hour.

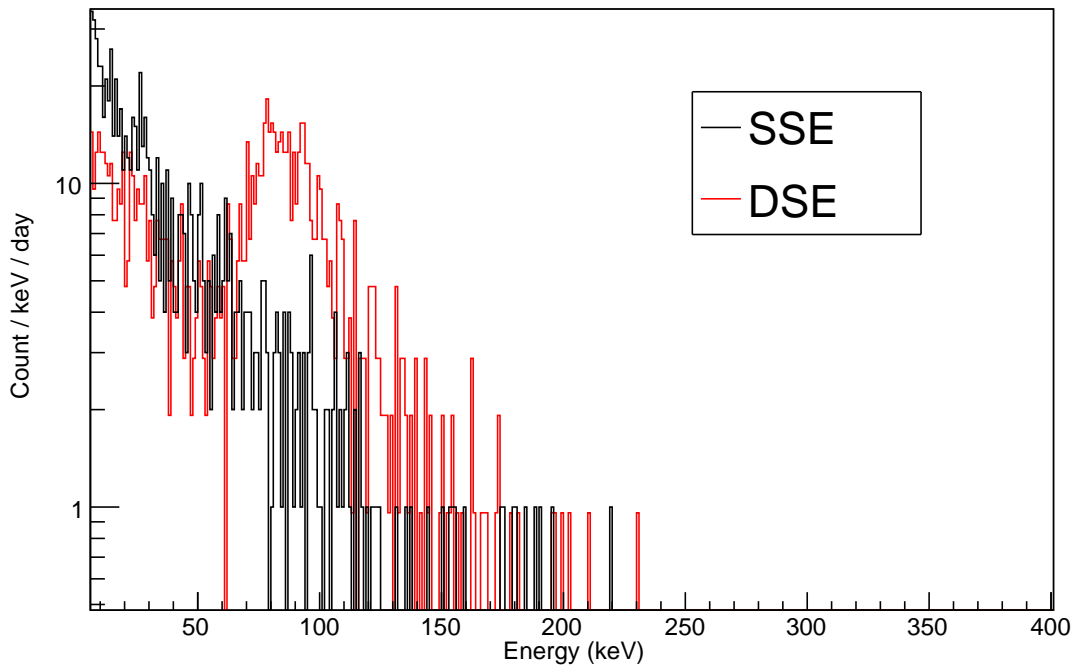


Figure 8.10: Spectra of all DSE and SSE events from CuFlon SPT surface measurements without any shielding. Total time of measurement was 25 h. The observed SSE background rate was 390 events/day and DSE rate was 482 events/day.

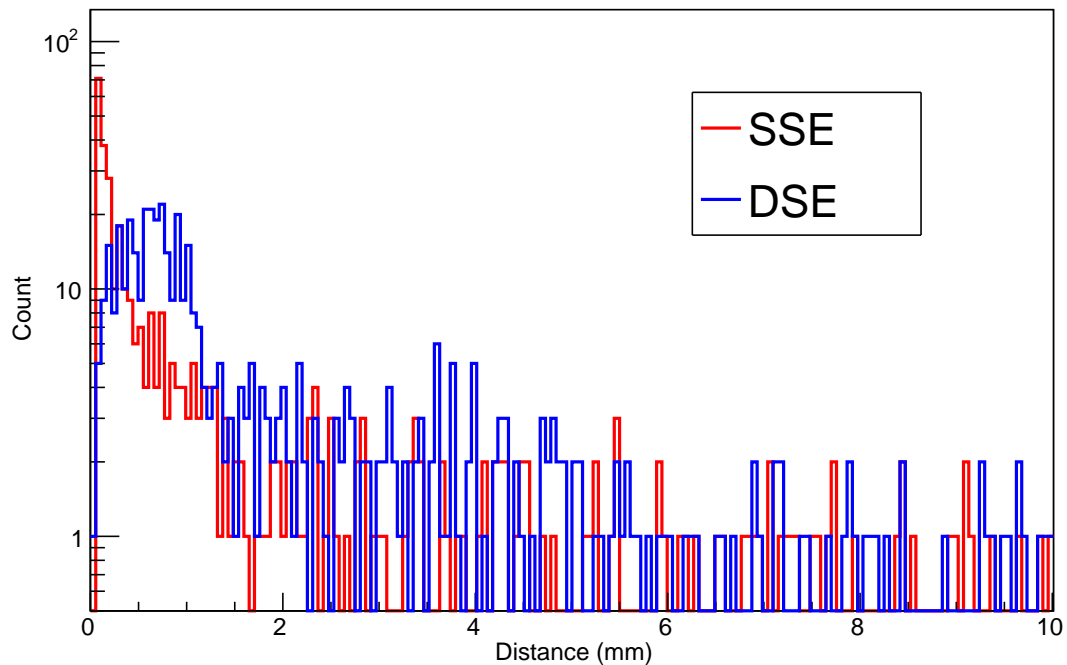


Figure 8.11: Distance distribution of all DSE and SSE events from CuFlon SPT surface measurements without any shielding. Total time of measurement was 25 h.

### Underground measurements with 5 cm Pb shield

Initially, underground measurements (in LSM, France) with CuFlon SPT were performed inside 5 cm Pb shielding. Figure 8.12 shows the simple shielding used in the measurements. In total 4118 hours ( $\sim 172$  days) of data was collected. Results from data analysis are presented in Table 8.4. Figure 8.13 compares the spectrum of SPT measurement with SPD measurements, both with 5 cm Pb shielding from the underground measurements. A factor of eight reduction in the background (all events) was observed in SPT (per detector) compared to SPD. The background rates (per hour) were 0.17 and 0.47, respectively for SSE and DSE events and in the energy region 19 - 23 keV were  $1.94 \times 10^{-3}$  and  $3.64 \times 10^{-3}$ . Figure 8.14 shows the distance distribution of SSE and DSE events from the measurements, which can be used as an additional background suppression criteria. The SSE distribution is almost identical to previous measurements and the DSE distance distribution does not show any peaks, but a gradual decrease from 1.5 mm to 10 mm. This DSE distribution indicates the influence of external particles passing through both detectors or scattering on both detectors. By applying a distance cut (0.7 - 4 mm), the background level was further suppressed. The SSE background rate was reduced to  $2.43 \times 10^{-4}$  events/h, whereas the DSE background rate was reduced to  $1.94 \times 10^{-3}$  events/h in the ROI.



Figure 8.12: CuFlon SPT inside 5 cm Pb shielding in the LSM underground laboratory, without top layer shielding.

	All events/h	in ROI/h
Total Events	$37.08 \pm 0.09$	$0.87 \pm 0.01$
SSE	$0.17 \pm 0.63 \times 10^{-2}$	$1.94 \times 10^{-3} {}^{+8.06 \times 10^{-4}}_{-6.54 \times 10^{-4}}$
DSE	$0.47 \pm 0.01$	$3.64 \times 10^{-3} {}^{+1.05 \times 10^{-3}}_{-8.94 \times 10^{-4}}$
SSE dist	$0.04 \pm 3.16 \times 10^{-3}$	$2.43 \times 10^{-4} {}^{+4.26 \times 10^{-4}}_{-1.53 \times 10^{-4}}$
DSE dist	$0.28 \pm 8.26 \times 10^{-3}$	$1.94 \times 10^{-3} {}^{+8.06 \times 10^{-4}}_{-6.54 \times 10^{-4}}$

Table 8.4: Results of CuFlon SPT underground background measurements, with 5 cm lead shielding. The region of interest (ROI) is 19 - 23 keV. Total time of measurement was 4118 hours.

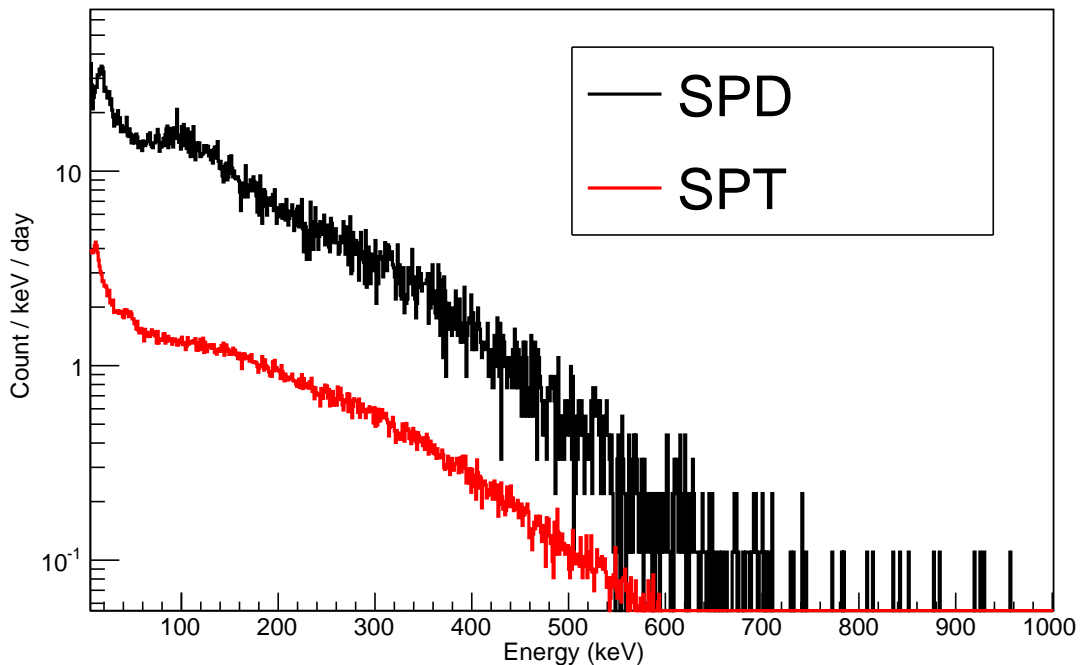


Figure 8.13: Comparison of CuFlon SPT and SPD spectra from underground measurements with 5 cm of Pb shielding. Total time of measurement was 4118 hours and 219 hours for SPT and SPD, respectively. Spectra are normalized per detector per day for both measurements.

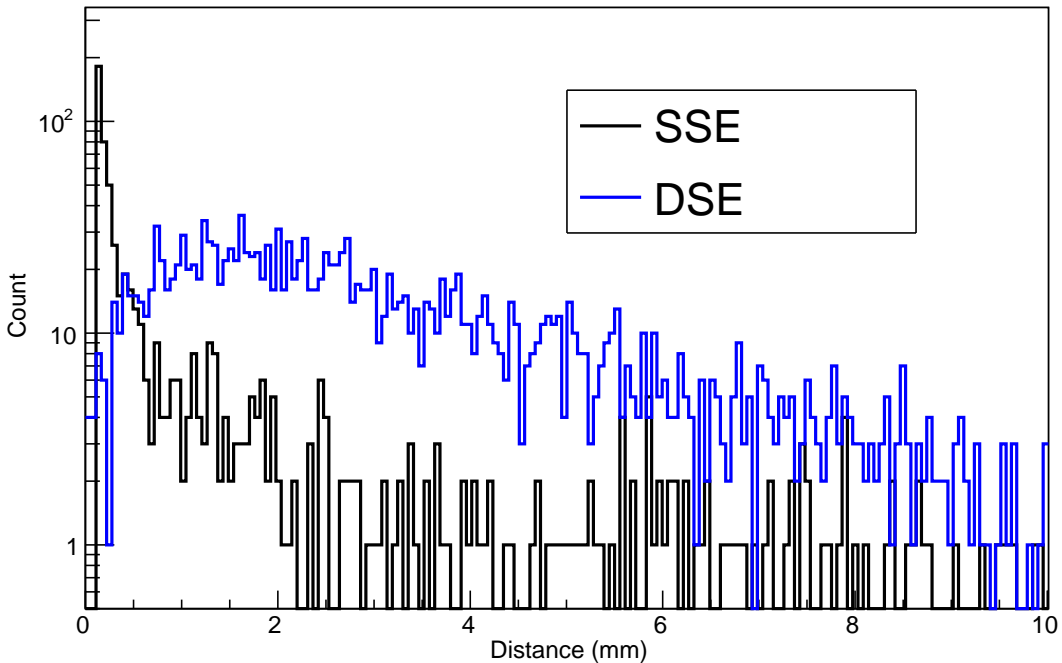


Figure 8.14: Distance distribution of SSE and DSE events from CuFlon SPT underground measurements using 5 cm Pb shielding, from 4118 hours of data.

### Underground measurements with more sophisticated shielding

After finishing the basic measurements with 5 cm of Pb shielding, it was decided to construct a comprehensive shielding and continue the measurements. The new 'full shielding' installed in the LSM underground laboratory has three layers. Figure 8.15 shows the schematic of the shielding. The outermost layer of the shielding is from borated PE which is against fast and thermal neutrons. Inside this layer is 10 cm Pb shielding which suppress effectively external gamma radiation. The lead used was from a stock produced before world war II and the activity was found to be 50 Bq/kg. The innermost layer is made of 2 cm electrolytic copper which is to guard against any gammas and X-rays from Pb shield. Figure 8.16 shows the partially opened shielding. Inner volume of the shielding is 40 cm<sup>3</sup> which is big enough for background measurements as well as real measurements in the coming years. Additionally, Radon-free (< 10 mBq/m<sup>3</sup>) and cooled air will be flushed inside the setup against Rn progenies and to reduce the heating of the setup.

Currently, the CuFlon SPT unit is inside the full shielding and measures the background. From a data set of 46 days of measurements, the estimated background rates are listed in Table 8.5. The Figure 8.17 shows the full spectrum of the events and compares with the measurements using 5 cm Pb shielding. Figure 8.18 shows the DSE and SSE spectra from the measurements. No SSE or DSE events were observed during the 46 days of measurements in the region of interest (19-23 keV). Significant reduction of background

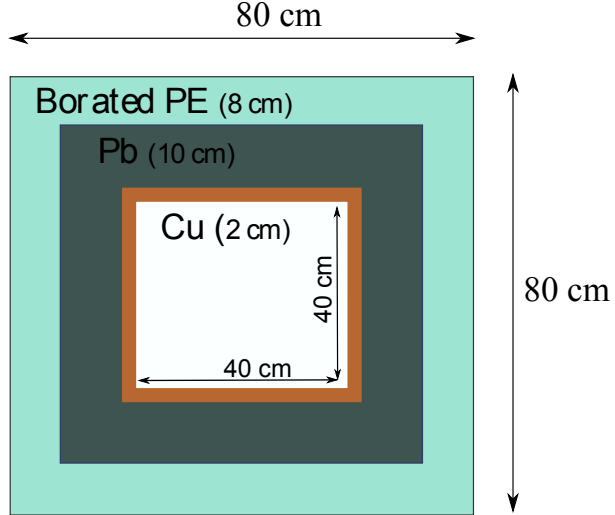


Figure 8.15: Schematic illustration of the full shielding installed in the LSM underground laboratory for double beta experiments (SPT and COBRA) using pixel detectors.



Figure 8.16: View of the full shielding partially open.

is obvious with the sophisticated shielding. In the Table 8.5 the upper limits calculated using Feldman-Cousins approach [87] is given for SSE and DSE rates in ROI. In Figure 8.19 the distance distribution is given which is very similar to usual distribution for such events. Figure 8.20 shows the scatter plot of the DSE and SSE events for the duration of measurement. In a window of 0 - 100 keV, in total sixteen DSE events and seven SSE events were observed during 46 days, but none of them where in the region of interest. Assuming a uniform background rate in this region, the background rates per  $\text{keV}^2$  area are  $1.45 \times 10^{-6}$  and  $6.34 \times 10^{-7}$  events/h for DSE and SSE, respectively. Recalculating the background rate in the ROI region, the obtained background rates are  $2.31 \times 10^{-5}$  events/h and  $1.01 \times 10^{-5}$  events/h for DSE and SSE, respectively.

	All events/h	in ROI/h
Total Events	$7.96 \pm 0.09$	$0.15 \pm 0.01$
SSE	$0.03 \pm 5.43 \times 10^{-3}$	$< 1.17 \times 10^{-3}$
DSE	$0.03 \pm 5.43 \times 10^{-3}$	$< 1.17 \times 10^{-3}$
SSE dist	$0.006^{+2.99 \times 10^{-3}}_{-2.49 \times 10^{-3}}$	$< 1.17 \times 10^{-3}$
DSE dist	$0.02 \pm 4.15 \times 10^{-3}$	$< 1.17 \times 10^{-3}$

Table 8.5: Results of CuFlon SPT underground background measurements, with full shielding. The region of interest (ROI) is 19 - 23 keV. All numbers are normalized per hour.

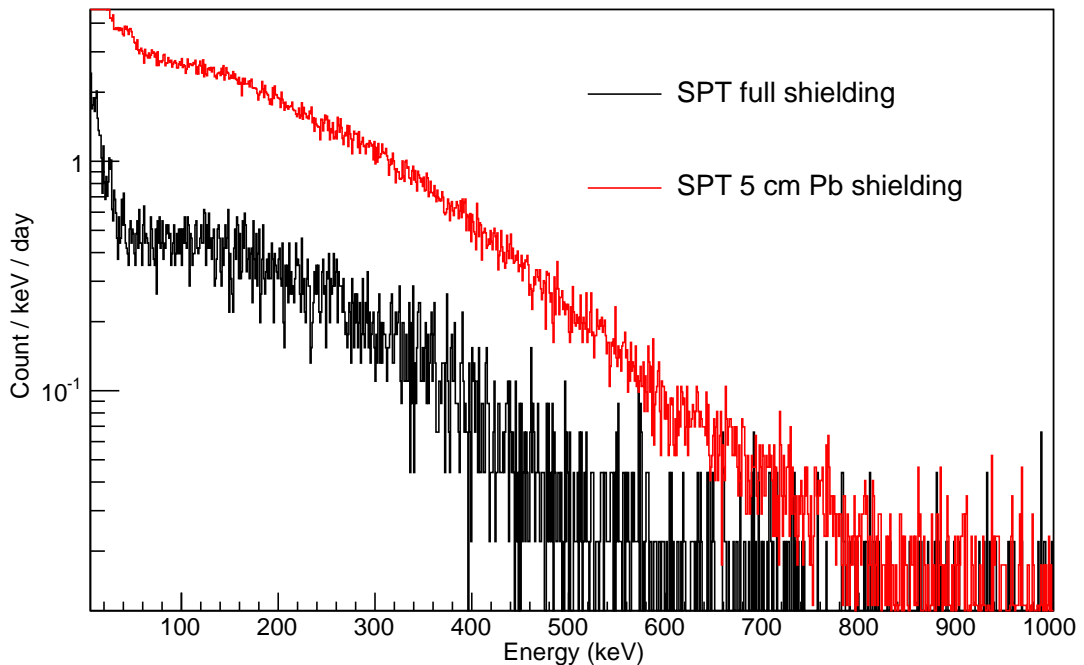


Figure 8.17: Comparison of full spectra from underground measurements with full shielding and 5 cm Pb shielding using CuFlon SPT. Time of measurement was 1104 hours and 4118 hours for full shielding measurement and 5 cm Pb shielding measurement, respectively.

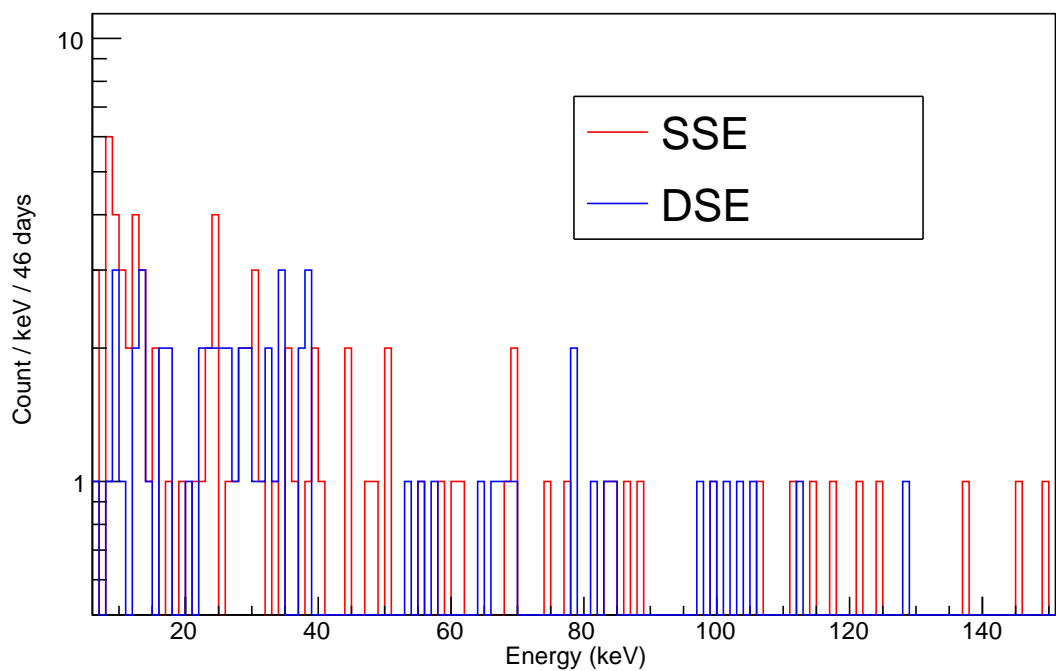


Figure 8.18: DSE and SSE energy spectra from CuFlon SPT underground measurements (46 days) with full shielding.

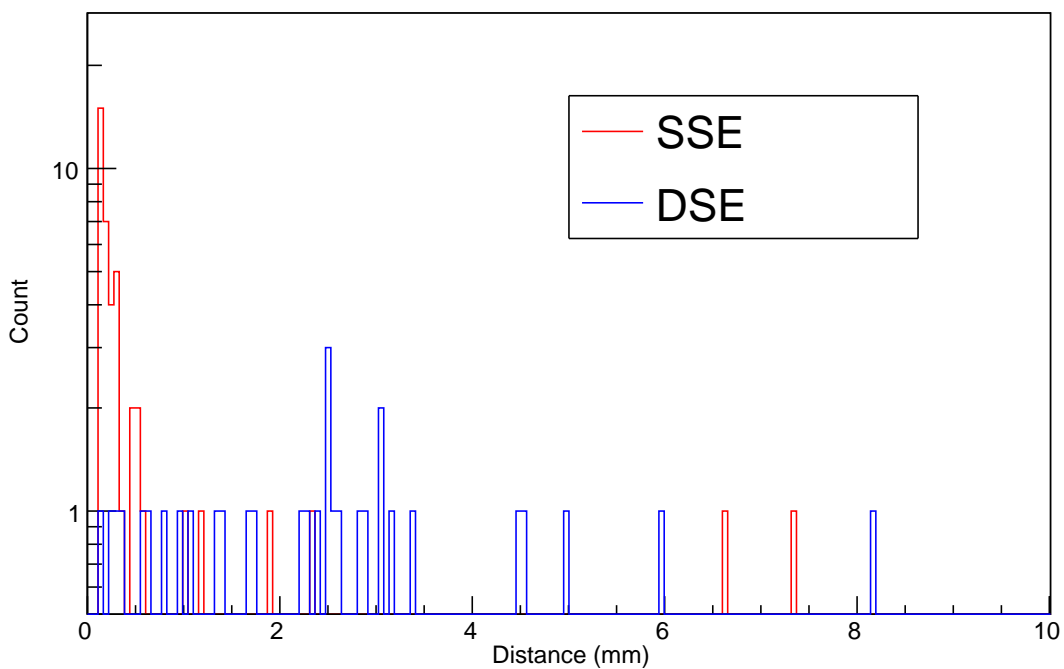


Figure 8.19: DSE and SSE distance distribution from CuFlon SPT underground measurements (46 days) with full shielding.

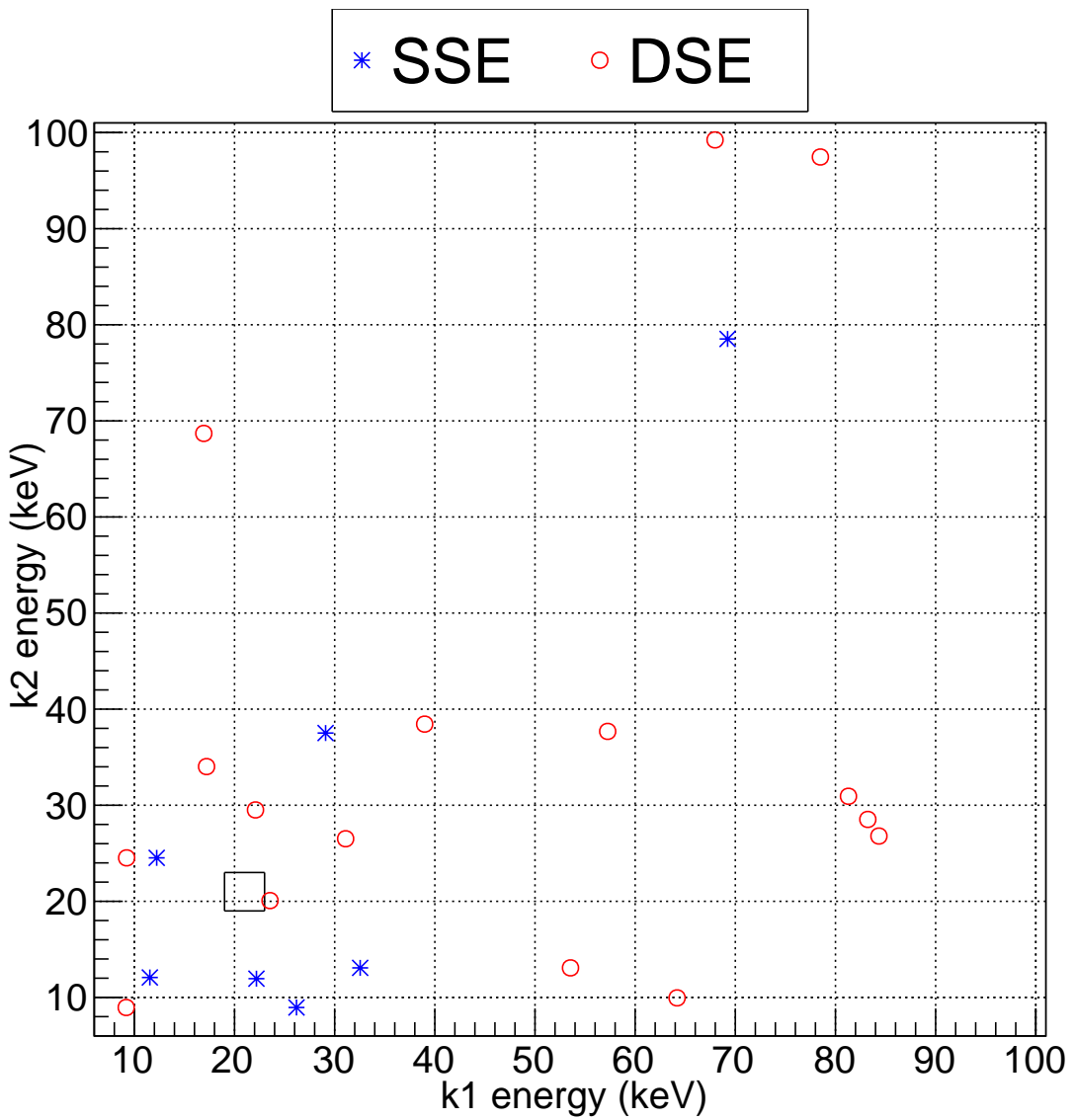


Figure 8.20: Scatter plot of DSE and SSE events from CuFlon SPT underground measurements with full shielding. Each point on the plot represents two coincident events represented by  $k_1$  and  $k_2$  (background events for  $^{106}\text{Cd}$   $2\nu EC/EC$  decay signature). The region of interest (19 - 23 keV) is marked with a rectangle.

### 8.2.3 Flex-Rigid Si Pixel Telescope

One unit of Flex-Rigid SPT (with two Si pixel detectors) was produced and tested for the functionality. Detectors had pixel pitch of  $55\ \mu\text{m}$  and sensors were  $500\ \mu\text{m}$  thick. Natural Cd foil ( $50\ \mu\text{m}$  thickness) was placed between the detectors. Figure 8.21 shows the full spectrum and Figure 8.22 presents the lower energy region from the surface measurements for 125 hours without any shielding. In Figure 8.22 one can see the Cd X-ray peak at 23 keV. Figure 8.23 is distribution of distance for SSE and DSE events from the measurement.

Due to the fact that Si pixel assembly is expensive (several thousand euros per piece), it was decided to use for functionality test assemblies with lower quality (noisy pixels). The first prototype was produced only to demonstrate the functioning of the setup in the Close Geometry as described in the section 3.2. Currently, four pairs of additional Flex-Rigid Si Pixel Telescopes units with good quality Si assemblies ( $500\ \mu\text{m}$  and 1 mm thick sensors) were produced. These units were calibrated and tested, and soon will be installed in our shielding in the LSM underground laboratory for long-term background tests.

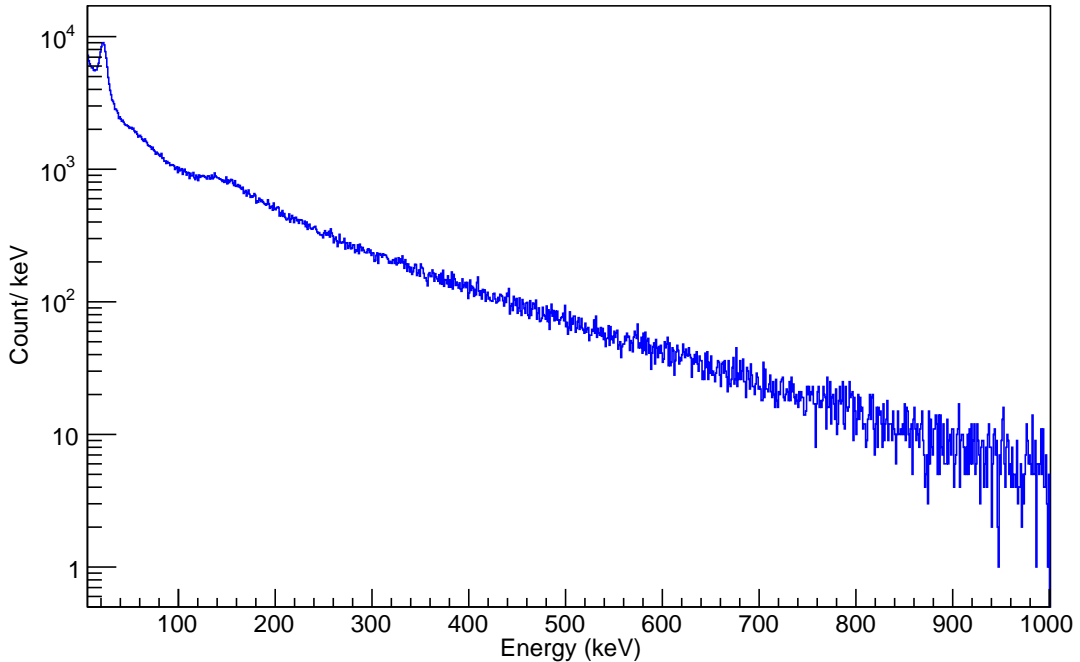


Figure 8.21: Spectrum from surface measurements with natural Cd foil between the pixel detectors in the Flex-Rigid SPT. Measurement was without shielding and duration of measurement was 125 hours.

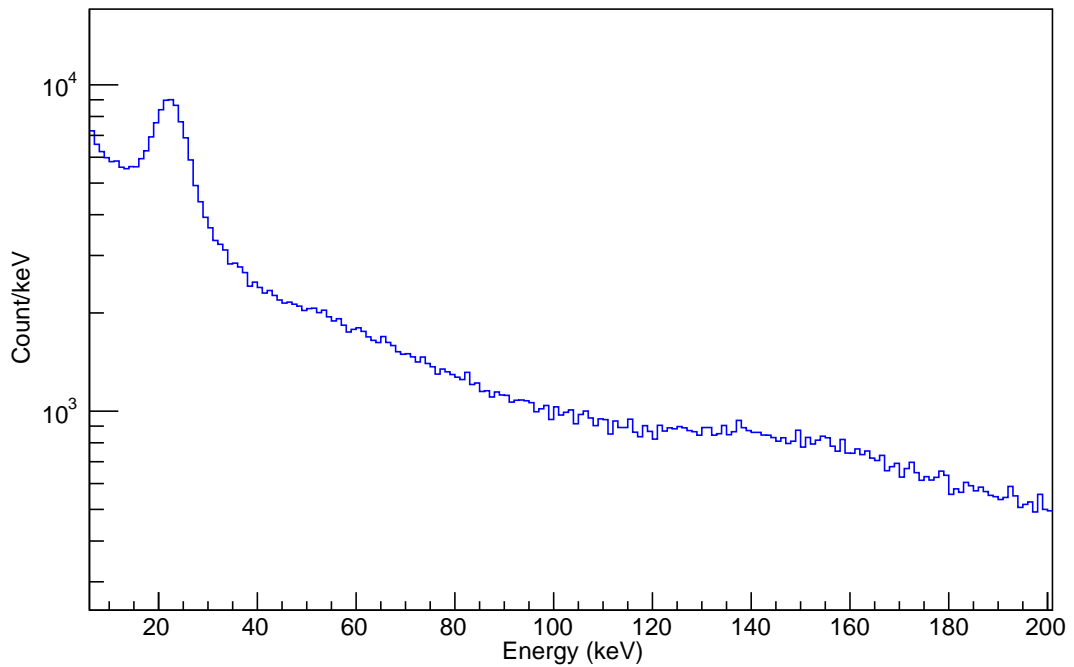


Figure 8.22: Spectrum in the energy window 5-200 keV from surface measurements with natural Cd foil between the pixel detectors in the Flex-Rigid SPT (without shielding). The Cd X-ray peak is visible in the 19-23 keV region.

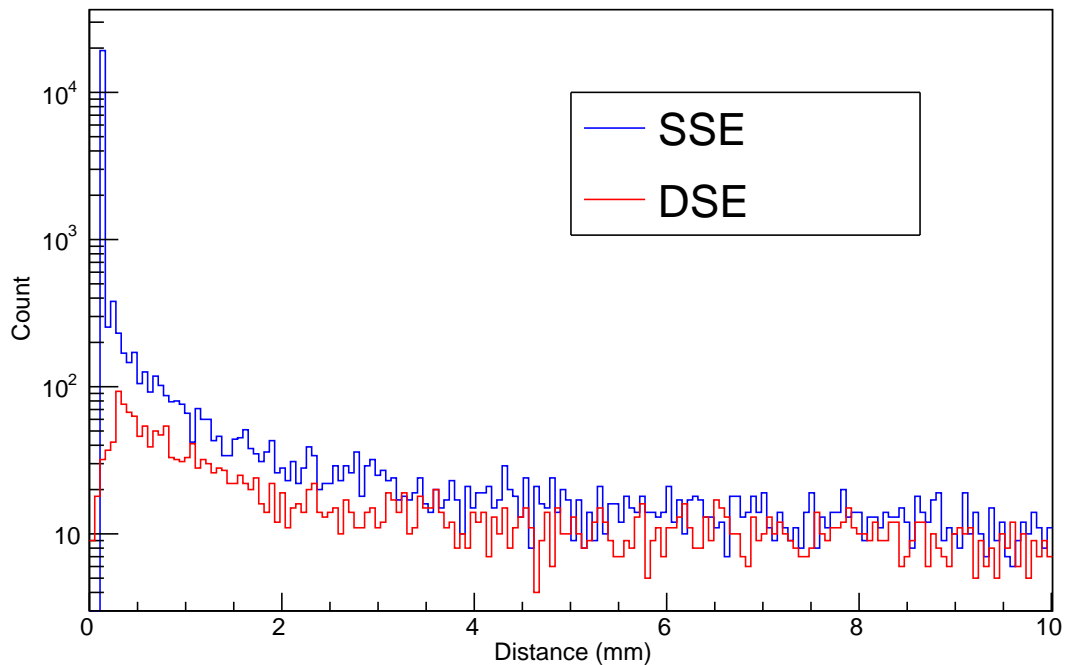


Figure 8.23: DSE and SSE distance distribution from Flex-Rigid SPT (with natural Cd foil between them) surface measurements (125 hours) without shielding.

### 8.3 Background comparison between different setups

In this section results of background rates for three different experimental setups (TGV II detector, standard Si Single Pixel Detector and CuFlon Si Pixel Telescope) are compared. Table 8.6 compares the all events rates between SPD and SPT setups in LSM. SPD background level is significantly higher (150.48 events/h) compared to SPT setup as it is not tuned for low background experiments. Proper selection of materials for construction of setup (CuFlon PCB, position of electronics far from Si assembly etc.) suppressed background by factor eight per detector in SPT setup (SPD is single detector whereas SPT is a detector pair). Also, background reduction capability of full shielding (borated polyethylene, low background lead and electrolytic copper) against simple shielding (5 cm of standard lead) is clearly visible (factor  $\sim 5$  reduction).

Data set	All events/h	in ROI/h
Si SPD 5 cm Pb	$150.48 \pm 0.83$	$4.60 \pm 0.14$
SPT 5 cm Pb	$37.08 \pm 0.09$	$0.87 \pm 0.01$
SPT Full shielding	$7.96 \pm 0.09$	$0.15 \pm 0.01$

Table 8.6: Comparison of background measurements for three different configurations (SPD, SPT with simple shielding and SPT with full shielding) conducted in the LSM underground laboratory. The region of interest (ROI) is 19 - 23 keV. SPD results are per one detector whereas the others are per detector pair.

Table 8.7 compares the SSE (Single Side Events) background rates in those three setups. The SSE rates of SPT with 5 cm Pb shielding was 0.04 events/h and in the ROI it was  $2.43 \times 10^{-4}$ . While after installation of new full shielding the total SSE rates was 0.006 events/h and no events were detected in the ROI (only limit is given) during 46 days. Table 8.8 compares the DSE (Double Side Events) background rates. The DSE rates of SPT with 5 cm Pb shielding was 0.28 events/h and in the ROI it was  $1.94 \times 10^{-3}$ . While after installation of new full shielding the total DSE rates was 0.02 events/h and no events were detected in the ROI (only limit is given) during 46 days.

Table 8.9 presents comparison of background rates between TGV II setup and SPT setup in full shielding. The SSE events in TGV II with all noise suppression conditions was 0.34 and in the ROI was  $9.82 \times 10^{-3}$ . The DSE events in TGV II with all noise suppression conditions was  $9.18 \times 10^{-3}$  and in the ROI was  $1.42 \times 10^{-5}$ . Due to the relative high rates of SSE events, it was not considered for the TGV II data analysis. Whereas, the estimated (value was estimated, not measured. See last paragraph of section 8.2.2) SSE and DSE background rates in the SPT with full shielding were  $1.01 \times 10^{-5}$  events/h and  $2.31 \times 10^{-5}$  events/h, respectively. This rate is very much comparable or better with respect to TGV II background rates, considering that the TGV II shielding is much more superior to SPT shielding. The background rates can be further reduced by thickness of the Pb layer and flushing with Rn-free air in the future. Also, planned Cu shielding between the detectors and readout system could further reduce the background rates.

SSE/h (with distance criteria)		
Data set	Total	ROI
Si SPD 5 cm Pb	$0.19 \pm 0.03$	$0.02 \pm 0.01$
SPT 5 cm Pb	$0.04 \pm 3.16 \times 10^{-3}$	$2.43 \times 10^{-4} {}^{+4.26 \times 10^{-4}}_{-1.53 \times 10^{-4}}$
SPT Full shielding	$0.006 {}^{+2.99 \times 10^{-3}}_{-2.49 \times 10^{-3}}$	$< 1.17 \times 10^{-3}$

Table 8.7: Comparison of estimated SSE background rates for three different configurations (SPD, SPT with simple shielding and SPT with full shielding). The region of interest (ROI) is 19 - 23 keV. SPD results are per one detector whereas the others are per detector pair.

DSE/h (with distance criteria)		
Data set	Total	ROI
SPT 5 cm Pb	$0.28 \pm 8.26 \times 10^{-3}$	$1.94 \times 10^{-3} {}^{+8.06 \times 10^{-4}}_{-6.54 \times 10^{-4}}$
SPT Full shielding	$0.02 \pm 4.15 \times 10^{-3}$	$< 1.17 \times 10^{-3}$

Table 8.8: Comparison of estimated DSE background rates for SPT with simple shielding and full shielding. DSE events cannot be detected by SPD as it is a single detector. The region of interest (ROI) is 19 - 23 keV.

Data set	All event/h		SSE/h (all criteria)		DSE/h (all criteria)	
	Total	ROI	Total	ROI	Total	ROI
SPT Full shielding	6.41	0.15	$6.34 \times 10^{-3}$	$1.01 \times 10^{-5} {}^a$	$1.90 \times 10^{-2}$	$2.31 \times 10^{-5} {}^a$
TGV II in full shielding	1.18	0.036	0.34	$9.82 \times 10^{-3}$	$9.18 \times 10^{-3}$	$1.42 \times 10^{-5}$

Table 8.9: Comparison of TGV II and SPT backgrounds with full shielding. The region of interest (ROI) is 19 - 23 keV for SPT and TGV II DSE whereas the TGV II SSE ROI is 40 - 44 keV. All numbers are normalized per detector-pair per  $1.96 \text{ cm}^2$  (SPT area) per hour.

<sup>a</sup>value was estimated, not measured. See last paragraph of section 8.2.2 for more information.

# Chapter 9

## Conclusions

Double beta decay ( $\beta\beta$ ) experiments are challenging frontiers in modern physics. Reduction of background as well as increasing the efficiency of the setup is the key in any  $\beta\beta$  experiment. Background reduction capabilities of pixel detectors were investigated as part of this PhD thesis. Timepix detectors from Medipix collaboration was used for the studies, due to its success in many fields and availability. The main task was to evaluate the applicability of pixel detectors in the experiment Si Pixel Telescope (SPT) for  $2\nu EC/EC$  of  $^{106}\text{Cd}$  and in the COBRA experiment for  $0\nu\beta\beta$  of  $^{116}\text{Cd}$ . For SPT, Timepix detectors with Si sensors were studied, while for COBRA CdTe sensors were evaluated. A coincidence setup in the form of a Pixel Telescope (pairs of pixel detectors arranged in face-to-face) was proposed for the experiments to increase the detection efficiency and to reduce the background events.

As in all  $\beta\beta$  experiments, the intrinsic contamination (from radioactive isotopes) of the setup, is of greater concern for pixel setup, too. Thus, materials needed for the pixel setup were analyzed for the presence of radioisotopes. The standard chip-carrier PCB material (FR4) was found to contain significant amount of radioisotopes. Therefore, different PCB materials were screened, and the materials with lowest contamination were identified (e.g. CuFlon, flexible PCB materials). Timepix chip-carrier board was redesigned with CuFlon and later improved with a flex-rigid design to achieve the Pixel Telescope geometry.

Two types of Pixel Telescopes were designed as part of this work. The first one was named CuFlon Pixel Telescope where the PCB material is CuFlon. This design gives the lowest radioactive impurities in the setup, but the distance between the detectors is fixed. The second design is based on flexible PCB materials, with rigid part from CuFlon (as a mechanical support for detectors) forming a flex-rigid structure, named Flex-Rigid SPT. This approach enables to adjust the distance between the detectors, thus improving the detection efficiency especially for SPT experiment. Both designs were fabricated, optimized and improved for the low background measurements (special care was taken on the position of the components such as capacitors and connectors). Delrin material was used to make a support structure, as it has very low radioactive impurities.

One Single Pixel Detector (SPD) with CdTe sensor of 1 mm thickness and  $110 \mu\text{m}$  pitch was used in the background measurements for COBRA experiment. Measure-

ments were performed on the surface and in the underground laboratory (LNGS, Gran Sasso, Italy). The data were analyzed and preliminary results were presented. It was demonstrated that the background events could be identified with acceptable accuracy, especially in the region of interest (2.5 - 3 MeV). Additionally, two units of CuFlon Pixel Telescopes using 2 mm thick CdTe sensors were produced and are being prepared for long-term background measurements. Availability of CdTe detectors and detector cooling are concerns for pixel activities for COBRA experiment.

Extensive background measurements were performed for SPT experiment. An improved shielding made of 2 cm of Cu, 10 cm of low radioactive Pb and 8 cm of borated polyethylene was recently installed in the LSM underground laboratory. So far, background measurements of an SPD (Si sensor with 300  $\mu\text{m}$  thickness, 55  $\mu\text{m}$  pitch) and a unit of CuFlon Si Pixel Telescope (CuFlon design, two Si sensors of 300  $\mu\text{m}$  thickness, 55  $\mu\text{m}$  pitch) were carried out on surface and in the underground laboratory (LSM, France). The data were analyzed and results were presented. The CuFlon SPT unit is currently undergoing long-term background measurements in the LSM underground laboratory inside the new sophisticated shielding, and from 46 days of measurements no SSE or DSE events were observed in the region of interest (19 - 23 keV). A unit of Flex-Rigid Si Pixel Telescope with natural Cd foil in between the detectors forming a 'sandwich' (detector touching the Cd foil) was constructed and functionality tests were performed. Additionally, four pairs of flex-Rigid SPTs have been produced (two units each using 0.5 and 1 mm thick Si sensors) for further measurements.

From TGV II phase 2 measurements with a total mass of 13.582 g of Cd enriched up to 75 % and for a duration of 9000 hours, the obtained half-life limit was  $4.1 \times 10^{20}$  years (world's best limit) for  $2\nu\text{EC}/\text{EC}$  decay of  $^{106}\text{Cd}$ . In the case of SPT, with the simulated efficiency of registration of 16.7 %, using Cd source foil of dimension 1.2 cm  $\times$  1.2 cm  $\times$  50  $\mu\text{m}$  enriched with  $^{106}\text{Cd}$  (upto 99 %) and with zero background condition (maximum one background event during whole measurement time) the achievable half-life limit is  $1.7 \times 10^{19}$  years using single unit from one year of measurement. With the 2 g (available for SPT experiments) of enriched Cd and using above mentioned Cd foil dimension  $\sim$ 30 pairs of SPT can be produced. With such 30 units, the achievable half-life limit is  $5.1 \times 10^{20}$  y from one year of measurement, while during four years we could reach the limit  $2.04 \times 10^{21}$  y.

Pixel detectors have potential in double beta decay experiments, but further studies and adaptations are necessary. Four pairs of newly produced Flex-Rigid SPTs have been calibrated and tested for long-term background measurements. They will be soon installed in the LSM underground laboratory for long term background measurements. Also background measurements of above setup with natural Cd foils in between the detectors will be conducted, and continued by  $2\nu\text{EC}/\text{EC}$  decay measurement with 2 g of enriched Cd. Finally the TGV collaboration would like to construct a larger setup comprised of 30 pairs of Si pixel detectors. Si pixel assemblies with thickness of 1 and 2 mm as well as enriched  $^{106}\text{Cd}$  ( $> 99$  % of enrichment) are already available, therefore to reach the limit on the level of  $10^{22}$  is realistic. Experiences gained from SPT will be used to construct a larger CdTe multi-detector prototype for COBRA experiment.



# Bibliography

- [1] J. R. Bond, G. Efstathiou, and J. Silk, “Massive neutrinos and the large-scale structure of the universe”, *Physical Review Letters*, vol. 45, pp. 1980 – 1984, 1980.
- [2] N. I. Rukhadze, C. Briançon, V. B. Brudanin, P. Čermák, V. G. Egorov, A. A. Klimenko, A. Kovalík, Y. A. Shitov, I. Štekl, V. V. Timkin, and T. Vylov, “Search for double beta decay of  $^{106}\text{Cd}$  in TGV-2 experiment”, *Journal of Physics Conference Series*, vol. 203, p. 012072, Jan. 2010.
- [3] K. Zuber, “COBRA-double beta decay searches using CdTe detectors”, *Physics Letters B*, vol. 519, pp. 1–7, Oct. 2001.
- [4] X. Llopert Cudie, C. Frojd, and M. Campbell, *Design and Characterization of 64K Pixels Chips Working in Single Photon Processing Mode*. PhD thesis, Mid Sweden U., Sundsvall, Sundsvall, 2007.
- [5] T. Holy, E. Heijne, J. Jakubek, S. Pospíšil, J. Uher, and Z. Vykydal, “Pattern recognition of tracks induced by individual quanta of ionizing radiation in medipix2 silicon detector”, *Nuclear Instruments and Methods in Physics Research A*, vol. 591, no. 1, pp. 287 – 290, 2008.
- [6] I. Štekl. et al., “Proposal of measurement of double beta decay of  $^{106}\text{Cd}$ ”, *Czechoslovak Journal of Physics*, vol. 48, p. 249, 1998.
- [7] P. Čermák, I. Štekl, Y. A. Shitov, F. Mamedov, E. N. Rukhadze, J. M. Jose, J. Čermák, N. I. Rukhadze, V. B. Brudanin, and P. Loaiza, “Use of silicon pixel detectors in double electron capture experiments”, *Journal of Instrumentation*, vol. 6, p. 1057, Jan. 2011.
- [8] “Neutrino history”, <http://lappweb.in2p3.fr/neutrinos/anhistory.html>, April 2014.
- [9] E. Fermi, “Versuch einer Theorie der  $\beta$ -Strahlen. I”, *Zeitschrift für Physik*, vol. 88, p. 161, 1934.
- [10] C.L. Cowan Jr., F. Reines, F. B. Harrison, H. W. Kruse, and A. D. McGuire, “Detection of the Free Neutrino: A Confirmation”, *Science*, vol. 124, p. 103, 1956.
- [11] The Super-Kamiokande Collaboration, “Evidence for oscillation of atmospheric neutrinos”, *Physical Review Letters*, vol. 81, pp. 1562–1567, 1998.

- [12] Q.R. Ahmad et. al. (SNO Collaboration), “Measurement of day and night neutrino energy spectra at SNO and constraints on neutrino mixing parameters”, *Physical Review Letters*, vol. 89, p. 011302, 2002.
- [13] K. Eguchi et al. (KamLAND Collaboration), “First Results from KamLAND: Evidence for Reactor Antineutrino Disappearance”, *Physical Review Letters*, vol. 90, p. 021802, 2003.
- [14] Ch. Weinheimer, KATRIN Collaboration, “KATRIN, a next generation tritium  $\beta$  decay experiment in search for the absolute neutrino mass scale”, *Progress in Particle and Nuclear Physics*, vol. 48, no. 1, pp. 141–150, 2002.
- [15] W.C. Haxton, G.J Stephenson Jr., “Double beta decay”, *Progress in Particle and Nuclear Physics*, vol. 12, pp. 409–479, 1984.
- [16] F. T. Avignone III, S. R. Elliott, and J. Engel, “Double Beta Decay, Majorana Neutrinos, and Neutrino Mass”, *Reviews of Modern Physics*, vol. 80, pp. 481–516, 2008.
- [17] M. Goeppert-Mayer, “Double beta-disintegration”, *Physical Review*, vol. 48, pp. 512–516, Sep 1935.
- [18] W. H. Furry, “On Transition Probabilities in Double Beta-Disintegration”, *Physical Review*, vol. 56, pp. 1184–1193, Dec. 1939.
- [19] A. S. Barabash, “Experiment double beta decay: Historical review of 75 years of research”, *Physics of Atomic Nuclei*, vol. 74, pp. 603–613, 2011.
- [20] F. T. Avignone III, G. S. King III, and Y. G. Zdesenko, “Next generation double-beta decay experiments: metrics for their evaluation”, *New Journal of Physics*, vol. 7, p. 6, 2005.
- [21] O. Civitarese, I. Štekl, J. Suhonen, ed., *Workshop on Calculation of Double-beta-decay Matrix Elements (MEDEX'13)*, vol. 1572 of *Conference collection*, (Prague), American Institute of Physics, 2013.
- [22] M.G. Inghram and J.H. Reynolds, “Double beta-decay of  $^{130}\text{Te}$ ”, *Physical Review*, vol. 78, pp. 822–823, 1950.
- [23] C. B. Levine, A. Griorso and G. T. Seaborg, *Physical Review*, vol. 77, p. 296, 1950.
- [24] E. der Mateosian and M. Goldhaber, “Limits for Lepton-Conserving and Lepton-Nonconserving Double Beta Decay in  $^{48}\text{Ca}$ ”, *Physical Review*, vol. 146, pp. 810–815, 1966.
- [25] E. Fiorini, A. Pullia, G. Bertolini, F. Cappellani and G. Restelli, “A search for lepton non-conservation in double beta decay with a germanium detector”, *Physics Letters B*, vol. 25, pp. 602–603, 1967.

- [26] M. Günther, J. Hellmig, G. Heusser, M. Hirsch, H. V. Klapdor-Kleingrothaus, B. Maier, H. Päs, F. Petry, Y. Ramachers, H. Strecker, M. Völlinger, A. Balysh, S. T. Belyaev, A. Demehin, A. Gurov, I. Kondratenko, D. Kotel'nikov, V. I. Lebedev, and A. Müller, “Heidelberg-Moscow  $\beta\beta$  experiment with  $^{76}\text{Ge}$ : Full setup with five detectors”, *Physical Review D*, vol. 55, pp. 54–67, 1997.
- [27] H. V. Klapdor-Kleingrothaus and I. V. Krivosheina, “The evidence for the observation of 0nu beta beta decay: The identification of 0nu beta beta events from the full spectra”, *Modern Physics Letters A*, vol. A21, pp. 1547–1566, 2006.
- [28] “Enriched Xenon Observatory”, <http://www-project.slac.stanford.edu/exo/default.htm>, February 2012.
- [29] M. Auger et al., “Search for Neutrinoless Double-Beta Decay in  $^{136}\text{Xe}$  with EXO-200”, *Physical Review Letters*, vol. 109, p. 032505, 2012.
- [30] E. Bellotti and GERDA Collaboration, “GERDA: a germanium detector array to search for neutrinoless double beta decay”, *Journal of Physics Conference Series*, vol. 39, pp. 338–340, 2006.
- [31] M. Agostini et. al. (GERDA Collaboration), “Results on Neutrinoless Double- $\beta$  Decay of  $^{76}\text{Ge}$  from Phase I of the GERDA Experiment”, *Physical Review Letters*, vol. 111, p. 122503, 2013.
- [32] “CUORICINO Cryogenic Underground Observatory for Rare Events”, <http://crio.mib.infn.it/wig/Cuoricinopage/CUORICINO.php>, March 2012.
- [33] E. Andreotti et. al., “ $^{130}\text{Te}$  neutrinoless double-beta decay with CUORICINO”, *Astroparticle Physics*, vol. 34, no. 11, pp. 822 – 831, 2011.
- [34] R. Ardito, “CUORE: A Cryogenic Underground Observatory for Rare Events”, *ArXiv High Energy Physics - Experiment e-prints*, 2005.
- [35] “The SNO+ Detector”, <http://snoplus.phy.queensu.ca/About.html>, March 2012.
- [36] “Neutrino Ettore Majorana Observatory”, [http://en.wikipedia.org/wiki/Neutrino\\_Ettore\\_Majorana\\_Observatory](http://en.wikipedia.org/wiki/Neutrino_Ettore_Majorana_Observatory), March 2012.
- [37] V. I. Tretyak and NEMO-3 Collaboration, “Results of the double beta decay experiment NEMO-3”, *AIP Conference Proceedings*, vol. 1572, no. 1, pp. 110–113, 2013.
- [38] “SuperNEMO”, <http://nemo.in2p3.fr/supernemo/>, March 2012.
- [39] H. Klapdor-Kleingrothaus, A. Dietz, L. Baudis, G. Heusser, I. Krivosheina, B. Majarovits, H. Paes, H. Strecker, V. Alexeev, A. Balysh, A. Bakalyarov, S. Belyaev, V. Lebedev, and S. Zhukov, “Latest results from the HEIDELBERG-MOSCOW double beta decay experiment”, *The European Physical Journal A - Hadrons and Nuclei*, vol. 12, no. 2, pp. 147–154, 2001.

- [40] The GERDA Collaboration et. al., “Measurement of the half-life of the two-neutrino double beta decay of  $^{76}\text{Ge}$  with the GERDA experiment”, *Journal of Physics G: Nuclear and Particle Physics*, vol. 40, no. 3, p. 035110, 2013.
- [41] A. Gando et. al., “Limits on Majoron-emitting double- $\beta$  decays of  $^{136}\text{Xe}$  in the KamLAND-Zen experiment”, vol. 86, p. 021601, 2012.
- [42] J.B. Albert et al., “Improved measurement of the  $2\nu\beta\beta$  half-life of  $^{136}\text{Xe}$  with the EXO-200 detector”, vol. 89, no. 1, p. 015502, 2014.
- [43] C. Arnaboldi, C. Brofferio, C. Bucci, S. Capelli, O. Cremonesi, E. Fiorini, A. Giuliani, A. Nucciotti, M. Pavan, M. Pedretti, G. Pessina, S. Pirro, C. Pobes, E. Previtali, M. Sisti, and M. Vanzini, “A calorimetric search on double beta decay of  $^{130}\text{Te}$ ”, *Physics Letters B*, vol. 557, no. 34, pp. 167 – 175, 2003.
- [44] KamLAND-Zen Collaboration, “Limit on Neutrinoless  $\beta\beta$  Decay of Xe-136 from the First Phase of KamLAND-Zen and Comparison with the Positive Claim in Ge-76”, *ArXiv e-prints*, Nov. 2012.
- [45] G. Hausser, “Low radioactivity background techniques”, *Annual Review of Nuclear and Particle Science*, vol. 45, 1996.
- [46] N. I. Rukhadze, A. M. Bakalyarov, C. Briançon, V. B. Brudanin, P. Čermák, V. G. Egorov, A. A. Klimenko, A. Kovalík, V. I. Lebedev, F. Mamedov, Y. A. Shitov, F. Šimkovic, I. Štekl, V. V. Timkin, and S. V. Zhukov, “New limits on double beta decay of  $^{106}\text{Cd}$ ”, *Nuclear Physics A*, vol. 852, pp. 197–206, Feb. 2011.
- [47] V. B. Brudanin, N. I. Rukhadze, C. Briançon, V. G. Egorov, V. E. Kovalenko, A. Kovalík, A. V. Salamatin, I. Štekl, V. V. Tsoupko-Sitnikov, T. Vylov, and P. Čermák, “Search for double beta decay of  $^{48}\text{Ca}$  in the TGV experiment”, *Physics Letters B*, vol. 495, pp. 63–68, Dec. 2000.
- [48] A. P. Meshik, C. M. Hohenberg, O. V. Pravdivtseva, and Y. S. Kapusta, “Weak decay of  $^{130}\text{Ba}$  and  $^{132}\text{Ba}$ : Geochemical measurements”, *Physical Review C (Nuclear Physics)*, vol. 64, no. 3, p. 035205, 2001.
- [49] P. Beneš, P. Čermák, K. N. Gusev, A. A. Klimenko, V. E. Kovalenko, A. Kovalík, N. I. Rukhadze, A. V. Salamatin, F. Šimkovic, I. Štekl, V. V. Timkin, and T. Vylov, “The low background spectrometer TGV II for double beta decay measurements”, *Nuclear Instruments and Methods in Physics Research A*, vol. 569, pp. 737–742, Dec. 2006.
- [50] P. Čermák, I. Štekl, V. Bocarov, J. M. Jose, J. Jakubek, S. Pospíšil, M. Fiederle, A. Fauler, K. Zuber, P. Loaiza, and Y. Shitov, “Background capabilities of pixel detectors for double beta decay measurements”, *Nuclear Instruments and Methods in Physics Research A*, vol. 633, p. 210, May 2011.
- [51] I. Hrivnacova, D. Adamova, V. Berejnoi, R. Brun, F. Carminati, A. Fasso, E. Futo, A. Gheata, I. Gonzalez Caballero, A. Morsch, and for the ALICE Collaboration, “The Virtual Monte Carlo”, *eprint arXiv:cs/0306005*, May 2003.

- [52] “The Virtual Monte Carlo (VMC)”, <http://root.cern.ch/drupal/content/vmc>, June 2014.
- [53] J. Allison et al., “Geant4 developments and applications”, *IEEE Transactions on Nuclear Science*, vol. 53, p. 270, 2006.
- [54] “Physics Lists for Electromagnetic Interactions”, [https://geant4.web.cern.ch/geant4/collaboration/working\\_groups/electromagnetic/physlist.shtml](https://geant4.web.cern.ch/geant4/collaboration/working_groups/electromagnetic/physlist.shtml), June 2014.
- [55] V. O.A. Ponkratenko and Yu.G. Zdesenko, “Event generator DECAY4 for simulating double-beta processes and decays of radioactive nuclei”, *Physics of Atomic Nuclei*, vol. 63, p. 1282, 2000.
- [56] R. Bailey et al., *Nucl. Instr. and Meth.*, vol. 213, p. 201, 1983.
- [57] G.D. Agnew et al., *Proceedings of the International Conference on High Energy Physics, World Scientific*, 1992.
- [58] K. Abe et al., *Nuclear Instruments and Methods in Physics Research A*, vol. 400, p. 287, 1997.
- [59] E. H. Heijne, “Semiconductor micropattern pixel detectors: a review of the beginnings”, *Nuclear Instruments and Methods in Physics Research A*, vol. 465, no. 1, pp. 1 – 26, 2001.
- [60] S.L. Shapiro et al., *Nuclear Instruments and Methods in Physics Research A*, vol. 275, p. 580, 1989.
- [61] S.L. Shapiro et al., in: T. Dombeck, V. Kelly, G.P. Yost (Eds.), *Proceedings Det. Research and Development for the Superconducting Super Collider, World Scientific, Singapore*, vol. 275, p. 139, 1991.
- [62] Eric A. Vittoz, *Nuclear Instruments and Methods in Physics Research A, Proceedings First Pixel Workshop, Leuven.*, vol. 275, p. 472, 1989.
- [63] Eric A. Vittoz, *IEEE Journal of Solid-State Circuits*, vol. SC-20, p. 657, 1985.
- [64] N. Wermes, “Trends in pixel detectors: tracking and imaging”, *IEEE Transactions on Nuclear Science*, vol. 51, no. 3, pp. 1006–1015, 2004.
- [65] N. Wermes, “Pixel detectors for tracking and their spin-off in imaging applications”, *Nuclear Instruments and Methods in Physics Research A*, vol. 541, pp. 150–165, Apr. 2005.
- [66] G. Claus, C. Colledani, W. Dulinski, D. Husson, R. Turchetta, J.L. Riester, D. Deptuch, G. Orazi, and M. Winter, “Particle tracking using CMOS monolithic active pixel sensor.”, *Nuclear Instruments and Methods in Physics Research A*, vol. 465, p. 120 – 124, 2001.

- [67] J.J. Velthuis et al., “DEPFET, a monolithic active pixel sensor for the ILC.”, *Nuclear Instruments and Methods in Physics Research A*, vol. 579, p. 685 – 689, 2007.
- [68] B. Henrich, “Experience and results from the 6 Megapixel Pilatus System”, in *International Workshop on Vertex Detectors*, 2007.
- [69] “The Medipix Collaboration”, <http://medipix.web.cern.ch/medipix/index.php>, February 2012.
- [70] “EUDET: Detector R&D towards the International Linear Collider”, <http://www.eudet.org/>, February 2012.
- [71] V. Kraus, M. Holik, J. Jakubek, and V. Georgiev, “FITPix data preprocessing pipeline for the Timepix single particle pixel detector”, *Journal of Instrumentation*, vol. 7, no. 04, p. C04011, 2012.
- [72] D. Tureček, T. Holý, J. Jakubek, S. Pospíšil, and Z. Vykydal, “Pixelman: a multi-platform data acquisition and processing software package for Medipix2, Timepix and Medipix3 detectors”, *Journal of Instrumentation*, vol. 6, p. C1046, Jan. 2011.
- [73] J. Jakubek, “Semiconductor Pixel detectors and their applications in life sciences”, *Journal of Instrumentation*, vol. 4, p. 3013, Mar. 2009.
- [74] D. Vavrik, J. Dammer, J. Jakubek, I. Jeon, O. Jirousek, M. Kroupa, and P. Zlamal, “Advanced x-ray radiography and tomography in several engineering applications”, *Nuclear Instruments and Methods in Physics Research A*, vol. 633, Supplement 1, no. 0, pp. S152 – S155, 2011. 11th International Workshop on Radiation Imaging Detectors (IWORID).
- [75] C. Granja and S. Pospíšil, “Quantum dosimetry and online visualization of x-ray and charged particle radiation in commercial aircraft at operational flight altitudes with the pixel detector timepix”, *Advances in Space Research*, vol. 54, p. 241251, 2014.
- [76] D. Turecek, L. Pinsky, J. Jakubek, Z. Vykydal, N. Stoffle, and S. Pospisil, “Small dosimeter based on timepix device for international space station”, *Journal of Instrumentation*, vol. 6, no. 12, p. C12037, 2011.
- [77] Z. Vykydal et. al., “The Medipix2-based network for measurement of spectral characteristics and composition of radiation in ATLAS detector”, *Nuclear Instruments and Methods in Physics Research A*, vol. 607, no. 1, pp. 35 – 37, 2009.
- [78] J. Jakubek, A. Cejnarova, T. Holý, S. Pospíšil, J. Uher, and Z. Vykydal, “Pixel detectors for imaging with heavy charged particles”, *Nuclear Instruments and Methods in Physics Research Section A*, vol. 591, no. 1, pp. 155 – 158, 2008.
- [79] J. Jakubek, “Energy-sensitive X-ray radiography and charge sharing effect in pixelated detector”, *Nuclear Instruments and Methods in Physics Research Section A*, vol. 607, no. 1, pp. 192 – 195, 2009.

- [80] J. Jakubek, “Precise energy calibration of pixel detector working in time-over-threshold mode”, *Nuclear Instruments and Methods in Physics Research A*, vol. 633, Supplement 1, pp. S262–S266, 2011.
- [81] J. Čermák, “Particle track recognition in Timepix pixel detector”, Master’s thesis, Charles University in Prague, 2013.
- [82] “Kapton polyimide film”, [http://www2.dupont.com/Kapton/en\\_US/](http://www2.dupont.com/Kapton/en_US/), June 2014.
- [83] “Microwave substrates”, <http://www.polyflon.com/microw.htm>, February 2012.
- [84] J. Jakubek, C. Granja, O. Jäkel, M. Martisikova and S. Pospíšil, “Detection and Track Visualization of Primary and Secondary Radiation in Hadron Therapy Beams with the Pixel Detector Timepix”, *IEEE NSS/MIC Knoxville Conference Record*, pp. 1967–1970, 2011.
- [85] E. D. Vincent Morard and P. Dokládal, “Efficient geodesic attribute thinnings based on the barycentric diameter”, *Journal of Mathematical Imaging and Vision*, vol. 46, no. 1, pp. 128 – 142, 2013.
- [86] J. Morales, et al., “Filtering microphonics in dark matter germanium experiments”, *Nuclear Instruments and Methods in Physics Research A*, vol. 321, pp. 410–414, 1992.
- [87] G. J. Feldman and R. D. Cousins, “Unified approach to the classical statistical analysis of small signals”, *physical review D*, vol. 57, pp. 3873–3889, Apr. 1998.



## **Appendix A**

### **Statement of author's contributions**

The author was responsible for implementation of pixel telescope. The structure of the pixel telescope was proposed by the author. The author carefully studied the intrinsic background for pixel detector components, selected suitable fabrication materials and validated it using background measurements. Many design improvements and optimization of pixel system for low background coincidence counting setup were performed. Also, extensive background measurements were performed with single pixel detectors and pixel telescopes (for both TGV and COBRA). Data processing and understanding of the background data was also the responsibility of author. Author was also responsible for preparing articles and presenting results at conferences. The newly installed sophisticated shielding was proposed by author based on the background measurements.

Intrinsic background measurements at the LSM, France was performed by staffs at the LSM laboratory. Simulations and efficiency calculations for SPT as well as COBRA were done by TGV collaboration partner Yu. A. Shitov. Data acquisition tool and some of the data processing capabilities of Pixelman software were utilized in the studies. The software tool Pixa by J. Čermák was also used for the data analysis.



# Appendix B

## List of relevant publications

- [1] J.M. Jose, P. Čermák, I. Štekl, J. Čermák, M. Fiederle, A. Fauler, Yu.A. Shitov, E.N. Rukhadze, N.I. Rukhadze, V.B. Brudanin, K. Zuber and P. Loaiza. "Timepix background studies for double beta decay experiments", *Journal of Instrumentation*, vol. 6, p. C11030, 2011 (corresponding author).
- [2] P. Čermák, I. Štekl, V. Bočarov, J.M. Jose, J. Jakubek, S. Pospišil, M. Fiederle, A. Fauler, K. Zuber, P. Loaiza, Yu.A. Shitov, "Background capabilities of pixel detectors for double beta decay measurements", *Nuclear Instruments and Methods in Physics Research Section A*, vol. A633, pp. S210-S211, 2011.
- [3] P. Čermák, I. Štekl, Yu. A. Shitov, F. Mamedov, E. N. Rukhadze, J. M. Jose, J. Čermák, N. I. Rukhadze, V. B. Brudanin and P. Loaiza, "Use of silicon pixel detectors in double electron capture experiments", *Journal of Instrumentation*, vol. 6 p. C01057, 2011.
- [4] V.B. Brudanin, V.G. Egorov, A.A. Klimenko, A. Kovalík, N. I. Rukhadze, V. V. Timkin, P. Čermák, J. Čermák, J. M. Jose, F. Mamedov, E. Rukhadze, I. Štekl, Ch. Briançon, F. Šimkovic, Yu.A. Shitov, A.M. Bakalyarov, V. I. Lebedev, S. V. Zhukov, and T. M. Bolotskaya, "Summary of the TGV experiment and future plans", *AIP Conference Proceedings*, vol. 1417, pp. 110-114, 2011.
- [5] J. M. Jose, P. Čermák, I. Štekl, Yu.A. Shitov, E.N. Rukhadze, N.I. Rukhadze, V.B. Brudanin, M. Fiederle, A. Fauler, P. Loaiza, "Pixel detectors in double beta decay experiments, a new approach for background reduction", *AIP Conference Proceedings*, vol. 1549, pp. 74-77, 2013 (corresponding author).
- [6] J. M. Jose and TGV collaboration, "Progress in the use of pixel detectors in double beta decay experiment TGV", *AIP Conference Proceedings* vol. 1572, pp.77-80, 2013 (corresponding author).



# Appendix C

## Other outputs

### Posters

13<sup>th</sup> International Workshop on Radiation Imaging Detectors (IWORID), " *Timepix background studies for double beta decay experiments*" , ETH Zurich, Switzerland (July 2011).

14<sup>th</sup> International Workshop on Radiation Imaging Detectors (IWORID), " *Silicon Pixel Telescope background measurements for double beta decay of 106 Cd*" , Coimbra, Portugal (July 2012).

Low Radioactivity Techniques 2013 (LRT 2013), " *Pixel detectors in double beta decay experiments, a new approach for background reduction*" LNGS, Italy (April 2013).

### Talks

Matrix Elements for the Double-beta-decay Experiments (MEDEX'13), " *Progress in the use of pixel detectors in double beta decay experiment TGV*" , Prague, (June 2013).



## **Appendix D**

### **Co-author's statements**



### **Co-author's statements**

Co-authors of articles listed in the Appendix B, 'List of relevant publications' declare that Joshy Madathiparambil Jose's role in preparation of experimental setup and measurements of background was very important, and his role in data processing as well as results interpretation was leading. He was also selected by the collaboration to be the corresponding author of articles (B [1], B [5] and B [6]) and present the results in the conferences (listed in Appendix C).

Name	Signature
------	-----------

N.I. Rukhadze



V.B. Brudanin



V.G. Egorov



A.A. Klimenko



A. Kovalík



V. V. Timkin



A.M. Bakalyarov



V. I. Lebedev



S. V. Zhukov



T. M. Bolotskaya



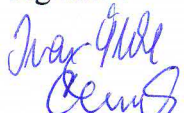
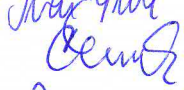
F. Simkovic





### **Co-author's statements**

Co-authors of articles listed in the Appendix B, 'List of relevant publications' declare that Joshy Madathiparambil Jose's role in preparation of experimental setup and measurements of background was very important, and his role in data processing as well as results interpretation was leading. He was also selected by the collaboration to be the corresponding author of articles (B [1], B [5] and B [6]) and present the results in the conferences (listed in Appendix C).

Name	Signature
I. Štekł	
P. Čermák	
J. Jakubek	
S. Pospíšil	
J. Čermák	
E.N. Rukhadze	
V. Bočarov	
F. Mamedov	
Yu.A. Shitov	
P. Loaiza	
K. Zuber	



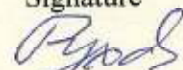
### **Co-author's statements**

Co-authors of articles listed in the Appendix B, 'List of relevant publications' declare that Joshy Madathiparambil Jose's role in preparation of experimental setup and measurements of background was very important, and his role in data processing as well as results interpretation was leading. He was also selected by the collaboration to be the corresponding author of articles (B [1], B [5] and B [6]) and present the results in the conferences (listed in Appendix C).

Name

N.I. Rukhadze

Signature

  
28.07.2014



## Co-author's statements

Co-authors of articles listed in the Appendix B, ‘List of relevant publications’ declare that Joshy Madathiparambil Jose’s role in preparation of experimental setup and measurements of background was very important, and his role in data processing as well as results interpretation was leading. He was also selected by the collaboration to be the corresponding author of articles (B [1], B [5] and B [6]) and present the results in the conferences (listed in Appendix C).

Name \_\_\_\_\_ Signature \_\_\_\_\_

M. Fiederle

A. Fauler

Mr EJU



### **Co-author's statements**

Co-authors of articles listed in the Appendix B, 'List of relevant publications' declare that Joshy Madathiparambil Jose's role in preparation of experimental setup and measurements of background was very important, and his role in data processing as well as results interpretation was leading. He was also selected by the collaboration to be the corresponding author of articles (B [1], B [5] and B [6]) and present the results in the conferences (listed in Appendix C).

Name	Signature
M. Fiederle	
A. Fauler	30.5.19



### **Co-author's statements**

Co-authors of articles listed in the Appendix B, 'List of relevant publications' declare that Joshy Madathiparambil Jose's role in preparation of experimental setup and measurements of background was very important, and his role in data processing as well as results interpretation was leading. He was also selected by the collaboration to be the corresponding author of articles (B [1], B [5] and B [6]) and present the results in the conferences (listed in Appendix C).

Name

J. Čermák

Signature

A handwritten signature in blue ink, appearing to read "J. Čermák".